L. Schmies

Improving the impact tolerance of RTM manufactured CFRP-steel hybrid structures

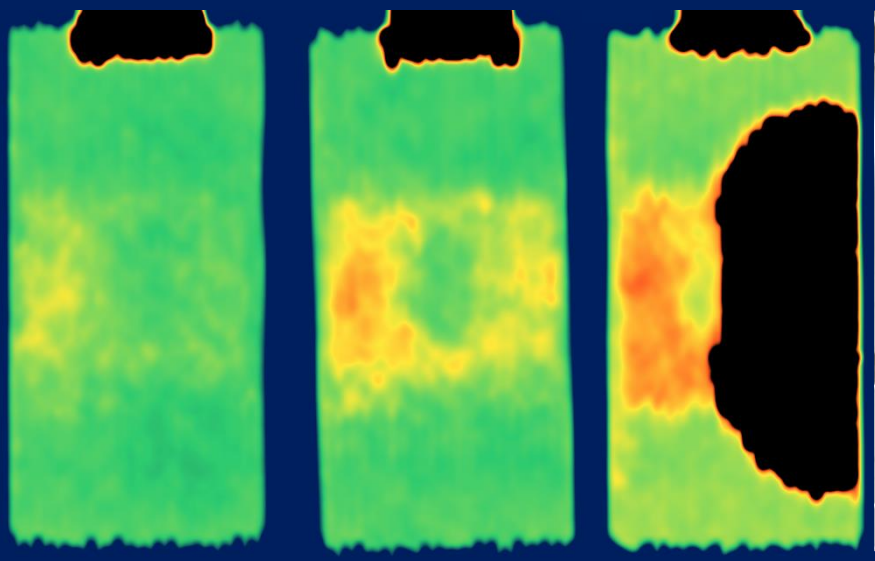

TU Delft

ad ultimum.

TU Delft

Improving the impact tolerance of RTM manufactured steel-CFRP hybrid structures

by

L. Schmies

to obtain the degree Master of Science at Delft University of Technology

Student number	5162831	
Project duration	October 1st, 2020 to August 31st, 2021	
Thesis committee	Prof. C.A. Dransfeld	TU Delft
	Dr. J. Teuwen	TU Delft
	J. Studer	adultimum ag
Version	*public*	

Abstract

Carbon fibre reinforced plastics offer various options to improve structures made from conventional materials such as metal. Carbon fibre reinforced plastics are used increasingly in various sectors such as the aerospace, automotive or sports industry. As carbon fibre reinforced plastics are less damage tolerant as metals due to the brittle epoxy resin matrix, this project dealt with improving the damage tolerance of the CFRP-steel hybrid structures. An extensive literature review highlights the possible toughening mechanisms of epoxy resin matrices by using additives made from polymeric and inorganic materials. Furthermore, the manufacturing process resin transfer moulding, but also potential test setups were researched. Apart from toughening the matrix, the interface between the carbon fibre body and a thin steel sheet attached on top of the specimen was researched as well. For that, different interface materials such as short fibre veils, weaves and polymeric materials were reviewed.

Based on the literature review a hypothesis was defined. Increasing additive concentrations, which were core-shell rubber particles and silica nanoparticles in particular, should yield an increasing impact performance. However, the influence of the manufacturing process and its limitations had to be considered as well. Furthermore, the influence of different interface materials can improve the bond strength of metal-CFRP hybrid structures. All test specimens were produced with resin transfer moulding and most process parameters were kept identical to the current production process in place at *adultimum ag* in Gossau, Switzerland.

The matrix toughening was researched by doing an impact testing series, which was analysed with microscopy, ultrasonic testing and differential scanning calorimetry. A variety of different additive combinations were included in impact specimens. An air pressured impact cannon was used to impact the specimens. For the interface toughening, a mandrel peel test setup was developed to compare the required peel forces for different interface materials.

For the peel test the steel sheet acted as a flexible adherend and was peeled from the rigid CFRP body. The specimens with no interface material included yielded the highest peel forces. Glass weave and two different aramid veils were tested alongside the specimens without any interface material. The glass weave acted as a barrier causing matrix rich regions, whereas the aramid veils caused fibre bridging increasing the peel force. However, the steel sheet caused to pull out carbon fibre bundles from the adjacent biaxial carbon fibre plies for the specimens with no interface material yielding the highest peel forces.

For the matrix toughening, an inversed trend as originally anticipated from the literature review and the defined hypothesis was obtained. With increasing additive content, the toughening performance and therefore impact tolerance decreased, as it was identified with ultrasonic testing. Microscopy, differential scanning electron microscopy and the size of dry spots due to high resin mixture viscosities support the assumption that the filling behaviour worsened with increasing additive content and therefore increased viscosity. A larger number of voids causes more crack nucleation sites weakening the structure.

To further confirm the assumptions made, void content analyses and repeated measurements should be performed.

Contents

List of figures

List of acronyms

4ENF	Four-point end-notched flexure
BVID	Barely visible impact damage
CFRP	Carbon fibre reinforced plastic
CSR	Core-shell rubber particles
DCB	Double cantilever beam
DGEBA	Diglycidyl ether of bisphenol A
DGEBF	Diglycidyl ether of bisphenol F
DoE	Design of Experiments
ELS	End loaded split
ENF	End-notched flexure
NDT	Non-destructive testing
Prepreg	Pre-impregnated fabric
RTM	Resin transfer moulding
SEM	Scanning electron microscopy
SENB	Single edge notched bending
SNP	Silica nanoparticles

List of symbols

θ	Angle of polar coordinates	°
a	Crack length	mm
G_C	Critical energy release rate	J/m^2
ρ	Density	kg/m^3
μ	Dynamic viscosity	$kg\ m^{-1}\ s^{-1}$
G	Energy release rate	J/m^2
K_c	Fracture toughness	$MPa * \sqrt{m}$
ν	Kinematic viscosity	$m^2\ s^{-1}$
L	Length	mm
G_{Ic}	Mode I critical energy release rate	J/m^2
K_{Ic}	Mode I fracture toughness	$MPa * \sqrt{m}$
G_{IIc}	Mode II critical energy release rate	J/m^2
K_{IIc}	Mode II fracture toughness	$MPa * \sqrt{m}$
k	Permeability	m^2
V	Potential of external forces	J
Δp	Pressure difference	N/mm^2
r	Radius of polar coordinates	mm
σ_{yy}	Shear stress in the xy-plane	N/mm^2
σ_{xx}	Stress along the x-axis	N/mm^2
σ_{xy}	Stress along the y-axis	N/mm^2
K_I	Stress-intensity factor	$MPa * \sqrt{m}$
U	Sum of the total strain energy stored in the elastic body	J
γ	Surface energy	J
t	Time	s
Π	Total potential energy per unit thickness	J
VDI	Viscosity density index	–

1 Introduction

This chapter provides an introduction to the thesis and project, which was done in corporation with the company *adultimum ag* located in Gossau, Switzerland. First, the project background is described, which is followed by a chapter highlighting the research questions and methodology used based on the defined objective. Then, a short outline of the thesis is given.

1.1 Project background

Carbon fibre reinforced plastics (CFRP) can show improved performance as structural components in comparison to isotropic materials such as metals. Their high strength and low weight in combination with the tailorability for creating anisotropic structures make CFRPs a viable option for applications in aerospace, automotive and sports.

Epoxies commonly used for CFRPs are rather brittle and therefore impact damage is usually unwanted to prevent microcracks, delamination or entire structural failure [1]. In this scenario, the composite structure is specifically supposed to withstand such impact loads and therefore, a part of the project is to investigate matrix toughening mechanisms for increasing the fracture toughness and how well the modifications coming with them can be incorporated into the automated manufacturing process.

Furthermore, to distribute the impact load into a wider area to avoid concentrated and high stresses, a thin steel plate is placed onto the hitting surface. This happens in-situ during the resin transfer moulding process, where the hollow CFRP structure cures and bonds to the metal plate. Given the different stiffnesses of the individual components, thermally induced stresses, the bond between both materials, but also the impact stress in combination with said stiffness jumps can cause micro cracks and eventually interface failure.

For this, it is investigated how the bond strength can be improved so that the metal-CFRP interface does not fail during the product lifetime. Both, the epoxy toughening, and the potential interface failure led to the following objective:

> “It is the objective to identify possible solutions to improve the overall fracture toughness of CFRP-steel hybrid structures produced with resin transfer moulding by considering the use of additives of thermoplastic, elastomeric, or non-organic material and short fibre reinforcements. The industrial requirements in terms of resin viscosity and filling behaviour are to be kept in mind.”

The only things to be modified are therefore the resin system and materials in the interface between the metal and the CFRP body. All other variables are kept constant.

1.2 Research methodology and questions

This chapter highlights the research methodology and the research questions which were derived from the objective presented before. The main research question was formulated as the following:

> "What is the influence on the impact performance when adding additives and interface materials to CFRP-steel hybrid structures - using the manufacturing process implemented at *adultimum ag* – and how do filling behaviour and injection times affect these results?"

To answer the main research question in a defined approach, sub questions have been identified.

1. Which epoxy toughening additives are available and suitable?
    a. Which toughening mechanisms exist and which ones are preferrable?
    b. Does a combination of additives can have a negative impact and how can this be anticipated or avoided?
    c. What consequences does an increasing viscosity due to increasing additive contents cause?

2. How can a metal-CFRP interface be modified and improved?
    a. Do short fibres improve the interfacial bond and fracture toughness of metal-CFRP interfaces?
    b. What is the influence of continuous fibre materials such as weaves or non-crimp fabrics on the interface bond strength?

By figuring out the answers to the sub questions stated above, the main research question is solvable. Answering these questions provides an understanding on how modifying the resin system or the interface influences the overall performance of the CFRP-steel hybrid structures, but also does it give an insight into the influence of the modified materials on the manufacturing process. Even, if additives or specific interface materials yield a better performance in theory, the part still needs to be manufacturable and that in an economically viable way.

From the literature review it becomes apparent that the influence of additives and their combination on the impact performance of metal-composite hybrids is not researched thoroughly. Especially, when considering steel-CFRP hybrid structures and the influence on and due to the manufacturing process. Limitations are given by the resin system – which is a fast curing system – and by the impactor and its speed. Furthermore, the combination of steel, its surface treatment, the resin system and the manufacturing process is not researched thoroughly, either. Each of the variables has a significant influence on the impact performance, which can be either improved or worsened with different interface materials.

For the matrix toughening part of the project, an impact testing series is designed, where a variation of different additives and concentrations is used to create multiple specimens. All specimens are manufactured

with resin transfer moulding (RTM). Then, using an air-powered ball cannon available at *adultimum ag*, the specimens are impacted, and their damage growth is compared. Combining these results with other information such as injection times or microscopy images, the toughening performance and influence on and due to the manufacturing process can be understood.
For the interface testing, a peel test is developed, which offers a simpler test setup than tests specifically designed for mode-II load cases, but still provides information applicable to said load case. After comparing different peel setups in the literature review, the one providing most applicable results and good reproducibility is chosen. This setup is installed in a universal testing machine available at *adultimum ag*. The main source of information are the peel forces, which can be further supported by microscopy, video footage and surface roughness analyses.

1.3 Thesis outline

First, a literature review is presented, which includes the used manufacturing process RTM, out-of-plane impacts and crack propagation, commonly used toughening possibilities for both the epoxy matrix and interfaces, and lastly non-destructive and peel testing. Then, the research performed at *adultimum ag* in cooperation with TU Delft is further described. For that, the materials and the sample preparation are described. Afterwards, the test methodologies including the developed test setups – in particular, the peel test and the impact test – and the results for both experiments are presented. Both experiments are concluded with a discussion of the results. Finally, a conclusion and recommendations summarise the thesis.

2 Literature Review

This chapter provides a literature review performed for the presented thesis project. After highlighting general aspects about carbon fibre reinforced plastics and the manufacturing process RTM, out-of-plane low velocity impacts including their causing damage to composite materials is explained. Damage causes cracks, which depending on the material and its toughness propagate differently. Therefore, the crack propagation and the fracture toughness including the energy release rate is explained. In a next chapter, commonly used peel tests are presented, highlighting their benefits and drawbacks. Based on the information gathered, the different toughening mechanisms by incorporating polymeric particles of elastomeric and thermoplastic basis, but also non-organic particles such as silica nanoparticles are presented. Furthermore, the toughness improvement by including interlaminar layers is presented.

2.1 Carbon fibre reinforced plastics

Carbon fibre reinforced plastics are composite materials made of carbon fibres embedded in a polymeric matrix, which is often a thermosetting epoxy resin or is made from thermoplastic materials. A composite material combines multiple materials to achieve better properties than the individual components have alone. The carbon fibre reinforcement comes in different types depending on the manufacturing process and the desired properties.

2.2 Resin transfer moulding

Manufacturing composite materials can be done with a large variety of different processes. There exist processes with already impregnated fibres (prepregs) and with dry fibres. Depending on the part and surface quality variations in the process occur. One liquid moulding process is called resin transfer moulding (RTM), where liquid resin is injected into a closed mould containing dry fibres. Resin transfer moulding is a widely used process in composite manufacturing. By creating a dry-fibre preform, it is injected with a low viscosity liquid thermosetting resin, which is an epoxy resin often [2, pp. 303-330].
The injection takes place in a closed mould consisting of two mould halves. By applying heat and pressure during and after the injection, the infusion and curing time can be designed to an optimum [3, pp. 201-225]. The part quality is comparable to autoclave processed parts with low void contents and high fibre volume fractions [2, pp. 303-330]. A schematic of the process is shown in Figure 2.1.

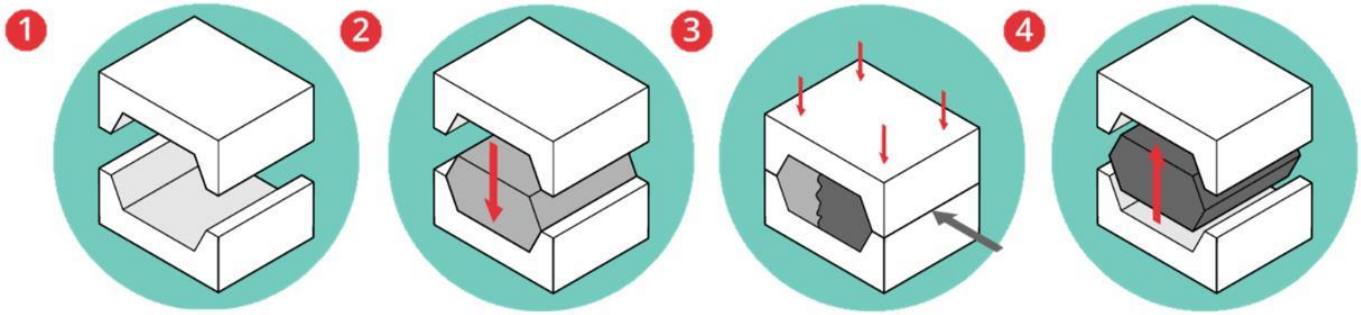

Figure 2.1: RTM process (modified): (1) Use of two mould halves, (2) Dry-fibre preform positioning and mould closing, (3) Infusion process with external locking force, (4) Demoulding of cured part [4]

The process yields good surface finish qualities on both sides and offers a good tolerance control. However, the initial non-recurring costs – especially due to the required precise tolerances of the mould – are relatively high in comparison to other processes such as vacuum infusion. Therefore, the process is rather suited for larger production volumes and smaller geometries [2, pp. 303-330].

It is also possible to manufacture hollow structures. To avoid the hollow area to be filled with resin and to maintain the shape of the part, different methods are available. There exist ceramic mandrels, wax cores, metal cores and bladder-like polymers filled with different media [5, pp. 338-387]. Resin transfer moulding also allows for incorporating features such as sandwich core sections, inserts or other types of reinforcement making it an integral composite part [2, pp. 303-330]. Advantages over classic autoclave processing with pre-impregnated fibres (prepregs) are no shelf-life, integral part manufacturing, lower material costs and reduced manual labour. Furthermore, lower pressures during processing as in comparison to autoclave processing allows for simpler and therefore reduced tooling costs [3, pp. 201-225].

To create the preform, layers of dry fibres are pre-shaped and preassembled in the required orientation and stacking sequence. This can either be done by hand or in an automated way by using robots or gantry systems. Fibres come in unidirectional tapes, woven fabrics, non-crimped fabrics, knitted fabrics and chopped fibre mats [2, pp. 303-330]. Tackifiers to keep the preform in shape are used, which are also called binders. Commonly used are low melting point thermoplastic or elastomeric materials, but also low resin content prepregs are available [2, pp. 303-330]. Alternatively, the individual plies can be stitched together to keep the preform in its shape [3, pp. 201-225].

The used epoxy resin for the project is defined by the company and is a fast curing system with a latency to cure at room temperature, which offers sufficient handling time before curing at elevated temperatures.

With respect to that another relevant aspect is the viscosity of the resin system. By adding additives to the resin, the viscosity usually increases due to the longer chains of thermoplastic and elastomeric materials. The overall viscosity needs to be kept under a certain threshold, so that the infusion time is kept to a minimum. Otherwise – due to the fast curing resin system – the curing might start before the preform has been fully impregnated and therefore causing dry spots and improper load transfers.

Furthermore, the glass transition temperature is a relevant factor for the curing and post curing cycle. For hollow structures, it is crucial that the glass transition temperature of the resin system is not lower than the

processing temperature for the core removal, as this would influence the part's geometry and performance while removing the core.

Another aspect relevant for resin transfer moulding is the thermal expansion of the different materials in the process. That value is depending on the temperature and describes a relative elongation or shrinkage. This is relevant for two aspects. On the one hand, carbon fibre reinforced epoxies have a thermal expansion close to zero [6], whereas other components of the curing part such as steels or core materials usually expand with increasing temperatures [7, p. 10]. On the other hand, the mould material – which is usually an aluminium alloy – has a different coefficient of thermal expansion as well, which needs to be kept in mind when it comes to part tolerances and demoulding processes. As the cure happens at elevated temperatures, the mould is expanded and therefore larger in size. This can be either beneficial or detrimental when it comes to demoulding, as the change in temperature and size can cause the mould to shrink onto the part making the demoulding more difficult.

2.3 Out-of plane low velocity impacts and their damage

Even though the composite materials show high specific strengths and stiffnesses, superior corrosion resistance, tailorability, and improved fatigue properties, they also have drawbacks in comparison to conventional materials such as metals [8–11]. The response to localized impact loading is limited in such a way that plastic deformation is marginal according to Cantwell and Morton [9]. The absorbed energy causes fracture and therefore stiffness and strength reductions [9].

Figure 2.2 shows typical damage types for composite laminates when impacted by low velocity projectiles. Common fracture modes are delamination, fibre-matrix debonding, fibre pull-out, fibre fracture and matrix cracking [9, 10]. On the impact side the laminate experiences compression due to the bending of the laminate, which therefore causes tension on the opposite side. On the tension dominated side both the matrix and fibres can fail. Close to the impact location through-thickness shear can cause the matrix to crack, which initiates delamination [12].

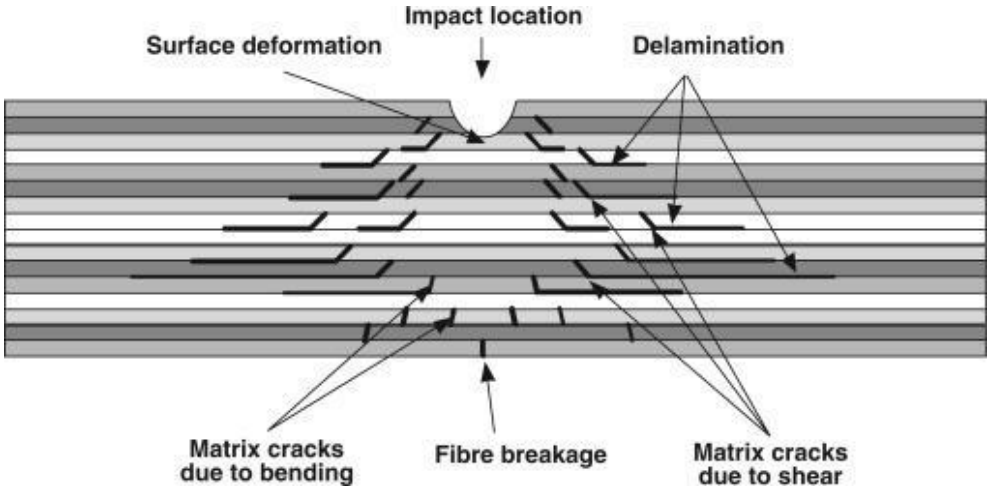

Figure 2.2: Schematic of typical low velocity impact damage in a composite laminate [12]

This delamination initiation is a mode I load case, whereas the delamination growth is mode II (see Figure 2.2) [13, pp. 17-20]. The different fracture modes are shown schematically in Figure 2.4. The delamination increases in size with increasing ply number away from the impact location, though it can differ depending on the ply orientation of the adjacent plies. Further influences on the damage mechanisms and locations are based on both the ply and laminate thickness. For example, a laminate with thin plies has lower interlaminar stresses, but decreases fibre volume fraction due to a larger number of resin rich regions. This causes delamination to occur more likely [13, pp. 147-148]. Even though delamination makes up a large amount of damage in a composite structure, it is rarely the cause for final failure, but rather fibre failure or matrix splitting or cracking. [12]

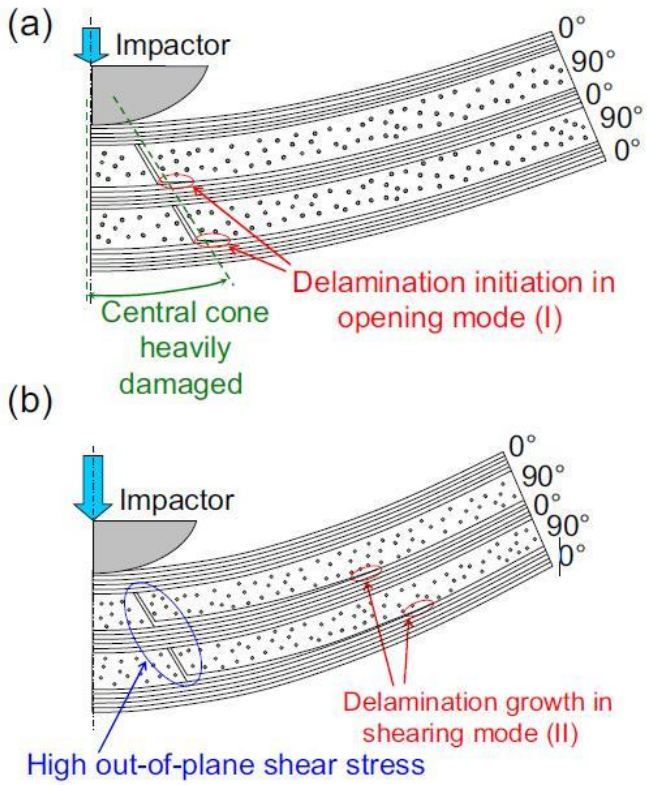

Figure 2.3: Typical scenario of delamination growth during impact loading, (a) Initiation, (b) Propagation [13]

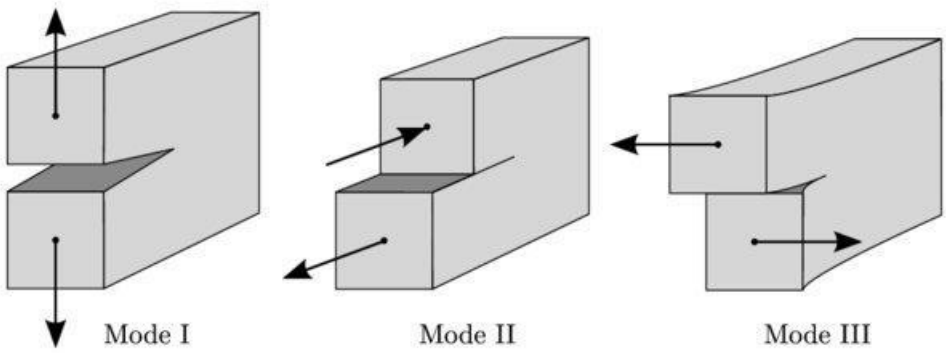

Figure 2.4: Fracture modes I (normal fracture), II (in-plane shear), and III (out-of-plane shear) [14]

As there is no general method to estimate the fracture mode and the size of the impact damage according to Abrate [11], impact test fixtures should resemble the loading condition the composite structure experiences in its operational environment [9].

According to Ullah et al [10] low velocity impacts cause delamination because of an insufficient interlaminar shear strength or because of a limited fracture toughness of the resin between the plies. The occurring shear stresses causing delamination can either be due to global deflections, due to the local contact force or due to a combination of both [11]. Furthermore, Abrate [11] highlighted that interply delamination happen at the interface between plies with different orientations, which is supported by Cantwell and Morton [9], who identified the greatest damage being at interfaces with ply orientation changes of 90 degrees. The delaminated area increases linearly with the kinetic energy of the object impacting the structure, but only after a minimum value has been reached [11]. Also, the overall stacking sequence and the geometry of the structure is relevant for the impact resistance [9].

The impact damage and the resulting delamination cause the in-plane compressive strength and stiffness to decrease significantly, which can be up to 50 % of the original strength and stiffness according to Cantwell and Morton [9, 11]. A good approximation to determine the impact resistance of the composite exposed to out-of-plane impact loads is based on the mode II interlaminar fracture toughness, but a mixed mode I/II assumption is more precise [10].

2.4 Crack propagation and the fracture toughness of composite materials

By inducing a sufficiently high load into a structure due to impacts for example, failure can occur. This failure of a solid structure is caused by crack initiation and subsequent crack propagation. Two ways to estimate the crack propagation are based on local and global approaches. The local approach considers the crack tip stress field, whereas the global approach considers the overall energy balance [15].

For the local approach, both the displacement and the stresses at the crack tip are identified, which are used for the parameters for the near crack tip stress and displacement fields. Crack tips usually cause peak stresses, which is comparable to a singularity making classical failure criteria inapplicable. However, when accepting the singularity at the crack tip, but not using the stress directly at the crack tip, the stresses near the crack tip can be calculated, nevertheless. Usually, the singular stress field at the crack tip can be considered as a good approximation of the finite stress field, if the difference is marginal for a small region around the crack tip. Independent of the geometry of the cracked solid and independent of the applied loads, the following equations are applicable for the stress field near the tip of crack in linearly elastic solids (see equations 2.1 – 2.3) [15].

$$\sigma_{xx} = \frac{K_I}{\sqrt{2\pi r}} * \cos\left(\frac{1}{2}\theta\right) * \left(1 - \sin\left(\frac{1}{2}\theta\right)\sin\left(\frac{3}{2}\theta\right)\right) \tag{2.1}$$

$$\sigma_{yy} = \frac{K_I}{\sqrt{2\pi r}} * \cos\left(\frac{1}{2}\theta\right) * \left(1 + \sin\left(\frac{1}{2}\theta\right)\sin\left(\frac{3}{2}\theta\right)\right) \tag{2.2}$$

$$\sigma_{xy} = \frac{K_I}{\sqrt{2\pi r}} * \sin\left(\frac{1}{2}\theta\right) * \cos\left(\frac{1}{2}\theta\right) * \cos\left(\frac{3}{2}\theta\right) \tag{2.3}$$

r and θ are the polar coordinates with the centre in the crack tip. Therefore, the stresses decrease with increasing distance from the crack tip. The factor K_I is the so-called stress-intensity factor and depends on the crack geometry and the applied load. A failure criterion based on the stress intensity factor has been proposed by Irwin [16]. There is a critical stress intensity factor, which – when reached – causes crack propagation to start. This critical value of the stress intensity is denoted as K_{Ic} (see equation 2.4) [15].

$$K_C = K_{Ic} \tag{2.4}$$

K_{Ic} is also known as the fracture toughness. This value is a material constant and the higher it is, the more energy is required for a crack to propagate. Its unit is $MPa * \sqrt{m}$ and is not directly linked to stresses and strains, but rather a proportionality factor in the stress field. With the experimentally derived fracture toughness and the calculated stress intensity factor based on the given load and geometry, the maximum allowable load can be calculated to avoid crack propagation.

For the global approach the overall energy balance during crack propagation is considered. It is assumed that during crack propagation energy gets released, which is assumed to be absorbed into the surface energy of the newly formed crack surface according to Griffith [17]. So, with crack extension a decrease in potential energy will occur [18, p. 9]. The following equation was proposed by Griffith for the global energy balance criterion (see equation 2.5) [15].

$$-d\Pi = 2\mathrm{da}\gamma \quad \text{or} \quad -\frac{\mathrm{d}\Pi}{\mathrm{da}} = 2\gamma \tag{2.5}$$

Π denotes the total potential energy per unit thickness of the system, which is a function of the crack length. With increasing crack length, the total potential energy decreases, as it gets transformed into surface energy, which is denoted as γ. The overall surface energy of the newly formed crack surfaces is defined as $2\mathrm{da}\gamma$.The total potential energy per unit thickness Π is the sum of the total strain energy stored in the elastic body U and of the potential of external forces V (see equations 2.6) [15, pp. 77-78].

$$\Pi = U + V \tag{2.6}$$

For the decrease in potential energy per unit crack length a factor called energy release rate and usually denoted by G was proposed by Irwin according to Sun and Jin [15, pp. 3-5]. The definition is shown in equation 2.7.

$$G = -\frac{d\Pi}{da} \tag{2.7}$$

The energy release rate can also be considered as a failure criterion when using the energy balance approach (see equation 2.7).

$$G = G_c = 2\gamma \tag{2.7}$$

The approach considers both the total energy of the cracked body and the surface energy of the new surface caused by the crack propagation. The energy release rate – similar to the fracture toughness – is a material constant and its unit is commonly given in *J/m²* or *kJ/m²* [15, p. 4]. It can be determined by measuring the critical stress to make a plate fracture with a known crack length or by measuring the crack length at which under a given a stress the plate fails [18, pp. 11-12].

Depending on the material's brittleness, the energy release rate might be larger than 2γ, which is due to plasticity at the crack tip resulting in an increased crack growth resistance. Once large plastic deformations occur, both the local and global approach with the fracture toughness and energy release rate are no longer applicable. However, for small degrees of plastic deformation modified approaches exist. Irwin proposed an effective stress intensity factor, which takes the plastic zone around the crack tip into account by adding half the plastic zone's size to the crack length [15, p. 7]. In addition to that, other failure criteria such as the crack opening displacement, which was introduced by Wells and others according to Sun and Jin [15, pp. 6-7], exist.

Both, for the fracture toughness and for the energy release rate one has to differentiate between the different modes. Both material parameters are different for mode I, mode II and mode III. For mode I load cases, the crack growth is predictable due to the fact that once it propagates, its direction remains unchanged. However, for mixed mode conditions this statement no longer holds true, making the crack growth prediction and calculation more difficult [15, p. 105].

2.5 Toughness improvement

To improve the toughness of a composite structure, various approaches are available today. This chapter focuses on the matrix modification with the use of polymeric and non-organic materials such as silica nanoparticles. Depending on the material used different toughening mechanisms occur, but also the weight fractions and combinations of different materials can cause both desirable and unwanted effects. Furthermore, interlaminar layers included into the layup can make the interface – which is usually resin dominated – a composite material making the interlaminar layers more fracture resistant. This chapter highlights short aramid fibre interface toughening, which due to its ductility provide excellent toughening behaviour.

2.5.1 Matrix modification

Given their brittle behaviour, the epoxies can be combined with additives before curing to toughen the matrix and to therefore increase the impact resistance and damage tolerance [1]. Furthermore, as a fast curing resin is used, the reaction is strongly exothermic, which can be kept in a controllable region with the aid of additives [19, 20]. To increase the impact resistance and to reduce internal heat build-up during curing, plasticizers such as elastomers, thermoplastics or core-shell-rubber-particles (CSR) can be incorporated into the matrix [21].

Damage in composite structures initiates in the matrix often. Loads not in fibre direction, but in any other direction can cause the matrix to be the dominating component, which is especially true for loads perpendicular to the fibres. Matrix dominated loading directions can cause the matrix to crack due to their brittle nature if thermosets and especially epoxy resins are used. With increasing load or additional load cycles the crack propagates, eventually resulting in delamination of adjacent plies. This hinders the load transfer and therefore weakens the structure. Loads causing delamination can happen both in field but also during manufacturing. Other causes can be insufficient or incorrect curing and foreign particles in the structure.

Improving the fracture toughness of the matrix can be achieved by using thermoplastic materials, which usually have a high toughness, but thermoplastics require high processing temperatures and have higher viscosities than thermosetting plastics.

As the processing conditions for thermoplastics are not suited for liquid moulding processes, increasing the toughness of brittle epoxy resins is inevitable for composite structures prone to impact [22]. Many methods are available, which include chemically modifying the backbone of the thermoset or decreasing the crosslink density to make the molecular chain more flexible. However, according to Kargarzadeh et al the most promising resin modification is including a secondary phase such as rubber additives [23]. Different additive types cause different toughening mechanisms with differing performances, where the performance increase depends upon the ability to dissipate work by said mechanisms. However, also the degree of cure and therefore a variation in crosslink density has an influence on the resin properties [22].

For bulk resins the additivations can cause an increase in toughness by a factor of 10 to 30 times, whereas in composite systems the increase is usually less than that [22].

According to Garg et al the main tougheners are either elastomeric or non-organic [22]. Each shows different toughening mechanisms, but in general rubbery additives yield a higher toughness than inorganic toughened resins. However, the better toughness performance comes with decreases in modulus, tensile strength and glass transition temperature, which can be improved by inorganic particles instead [22]. Furthermore, inorganic particles reduce the exothermic peak during curing. Combining both inorganic and rubber particles, the fracture toughness of the resin can be improved while maintaining or improving the other resin properties.

An overview of different toughening mechanisms is shown in Figure 2.5. The different mechanisms are explained in the following chapters, which focus on the rubber, inorganic and thermoplastic toughening mechanisms. Usually, multiple mechanisms can appear in toughened polymers, which contribute to the overall toughness increase.

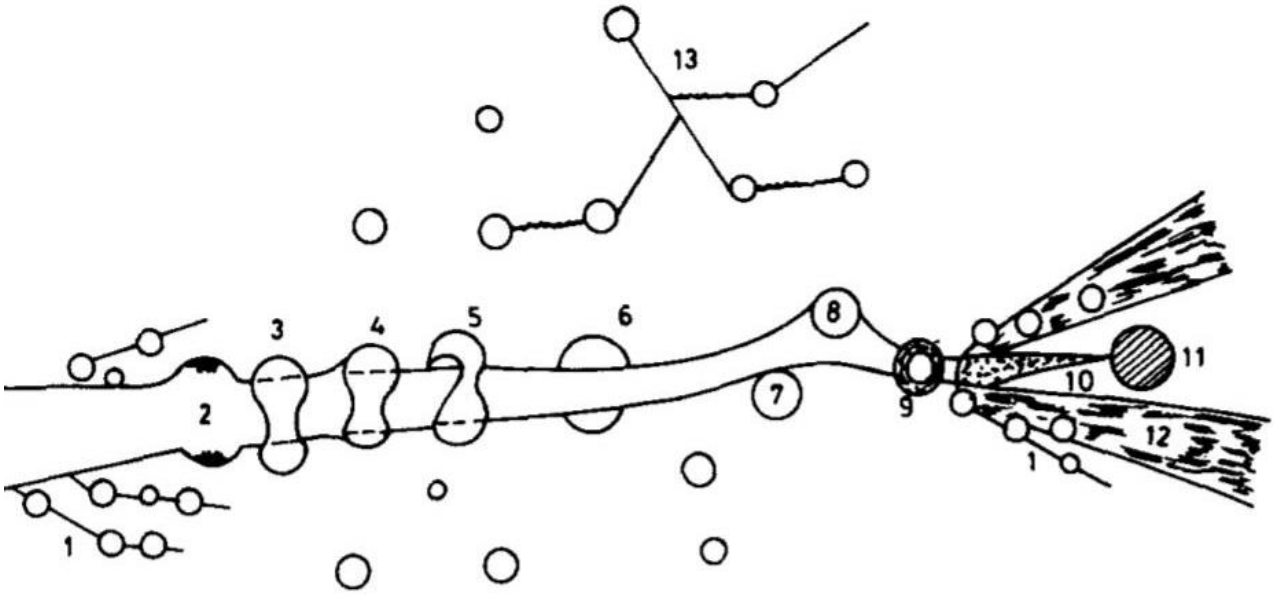

Figure 2.5: Crack toughening mechanisms in rubber-filled modified polymers: (1) shear band formation near rubber particles; (2) fracture of rubber particles after cavitation; (3) stretching, (4) debonding and (5) tearing of rubber particles; (6) trans particle fracture; (7) debonding of hard particles; (8) crack deflection by hard particles; (9) voided/cavitated rubber particles; (10) crazing; (11) plastic zone at craze tip; (12) diffuse shear yielding; (13) shear band/craze interaction [22]

For particle filled epoxies possible toughening mechanisms include an increased fracture surface area due to the irregular path of the crack, plastic deformation of the matrix around the particles and particle deformation. The crack deflection causing an irregular path accounts for a relatively small increase in toughness. Plastic deformation of the matrix around the particles always exists, as particles act as stress concentrators.

For all toughening materials, factors such as size, type of particle, volume fraction, geometric arrangements and bonding play a role in the performance of the toughener. This is especially relevant for reactive liquid rubbers, as the particle forming happens during the curing process. Depending on the cure time and volume fractions particle sizes differ, where slow cure, and high volume fractions yield larger particles and fast curing systems, and lower volume fractions cause the particles to stay small.

2.5.1.1 Rubber toughening mechanisms

Toughening epoxy resins can be achieved by incorporating elastomeric materials into the matrix. This can either be done with reactive liquid rubbers, which form rubbery phases during curing, or by adding so-called core-shell-rubber particles. Those particles have a rubbery core and an outer shell being either of more brittle thermosetting plastics or ceramics. The core is often based on polybutadiene and the shell is usually designed in such a way that strong interfaces to the matrix are achieved.

The main toughening mechanism when incorporating rubber particles into the thermosetting matrix is rubber cavitation and then shear yielding according to Kargarzadeh et al [23].
By exerting a stress onto the structure, the particles experience a triaxial stress state. Due to that, the hydrostatic tension in the particle can cause the particle to cavitate causing the stress state to become more uniaxial than originally triaxial. After this happened, the stress state of the particles promotes the growth of shear bands, which is a ductile behaviour and therefore toughening the matrix. Those shear bands are located in a deformation zone around the particles, which is due to stress concentrations in the matrix. The stress concentrations are caused by an interaction between the rubber particles and the crack tip. The higher the number of rubber particles in the matrix, the higher is the increase in toughness. As more particles cause more deformation zones to occur, the overall resin system becomes more ductile because of the cavitated rubber particles followed by shear band yielding.
Furthermore, rubber particles can cause cracks to deflect from their path reducing the crack tip opening, but also by splitting the crack into two separate ones. This increases the surface area, which requires more energy resulting in a slowed crack propagation. It is also known as micro-bifurcation. Larger particles cause crack deflection more likely than smaller particles.
Further toughening mechanisms when using rubber particles in epoxy matrices are crack-bridging and crack-pinning mechanisms. A schematic is shown in Figure 2.6.

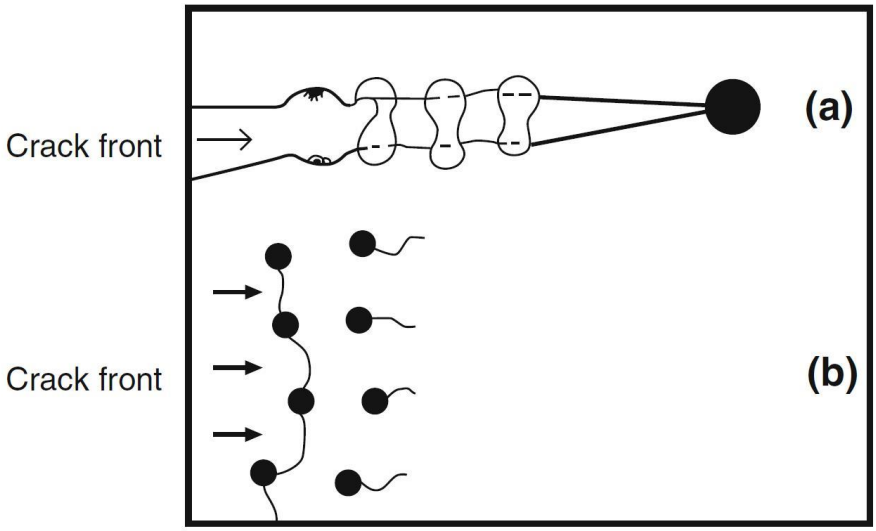

Figure 2.6: (a) Crack-bridging mechanism and (b) crack-pinning mechanism [23]

Cracks tend to propagate through the more brittle epoxy matrix rather than through the rubber particles. By propagating around the particles, the rubber particles stretch in between the two crack planes. With an increasing crack opening the particles strain-harden and eventually fail. However, this bridging of particles and the strain hardening increase the energy necessary for crack propagation and therefore making the system tougher. This toughening mechanism is called crack-bridging.
A more unlikely toughening mechanism to happen when incorporating rubber particles into the thermosetting resin is crack-pinning. The crack propagating through the material gets hindered doing so by the rubber

particles causing the cracks to pin by the particles. The crack front then bows between the particles, which increases the needed energy for the crack to propagate due to an increased surface. After the crack front bowed behind the particles, eventually they unify again. This causes so-called tails behind the particles, as the bowed cracks have offsets in height and therefore cause jumps between the different bowed cracks.
Another toughening mechanism is caused by deformation mechanisms such as crazing, shear yielding and an interaction of crazes with shear bands. The rubber particles act as nucleation sites for both crazes and shear bands. However, they can cause propagation obstruction of crazes resulting in controlled sizes of those. Therefore, rubber particles yield smaller crazes and therefore a reduction in the intrinsic flaw size, which results in an increase in fracture toughness. The toughening effect is depending on the crosslink density, as short chain lengths cause the space for crazing to happen to decrease as well. [22, 24]
Other mechanisms include volume dilatation of rubber particles and the surrounding matrix, but also shear yielding of the epoxy system. Dilatation is further enhanced during curing, where both shrinkage and thermal stresses are induced causing cavitations and the consequent growth of voids. Voids increase stress concentrations and promote the formation of plastic zones, which results in an increased shear band formation. In addition to that, shear bands occur due to strain inconsistencies near the crack tip, which is further enhanced by the addition of rubber additives. Those shear bands can also stop at another particle, which keeps the yielding localised. The shear bands cause crack tips to blunt, which then reduces stress concentrations and delays crack propagation.
According to Garg et al the approach of toughening epoxy resin systems with elastomeric additivations was initially mentioned by McGarry et al, who showed that liquid rubbers added to epoxide formulations can yield significant improvements. The use of reactive liquid rubbers is depending on two factors. Firstly, the rubber needs to be compatible with the resin system, so that it can dissolve and become well dispersed in the matrix. Secondly, they need to be chemically compatible ensuring a reaction between the rubber and the epoxide group.
There also exist so-called core shell rubber particles, which consist of a rubbery core and a shell made out of other polymeric material, which is compatible with the epoxy resin the particles are dispersed into. Throughout available literature, the increase in fracture toughness by adding core-shell-rubber particles has a wide range. Awang Ngah and Taylor [25] researched the toughening performance of core-shell rubber toughened glass fibre composites. They used an anhydride-cured epoxy system. The quasi-isotropic glass fibre reinforced composite was manufactured with resin infusion. The core-shell rubber particles used had a polybutadiene and a siloxane core. The particle diameters ranged from 85-115 and 250-350 for the polybutadiene and siloxane core, respectively. Several specimens with different weight fractions of core-shell rubber particles were manufactured. The concentrations used were 2, 5, 10 and 15 wt%. To measure the fracture energy, a double cantilever beam test for a mode I load case was carried out. Both particle types showed a linear increase for the increasing weight fraction of core-shell rubber particles, where the 15 wt% concentration showed approximately a tripling of the initial fracture energy. Figure 2.7 shows the results of the double cantilever beam test. It also highlights silica nanoparticles, but these results can be neglected for this chapter.

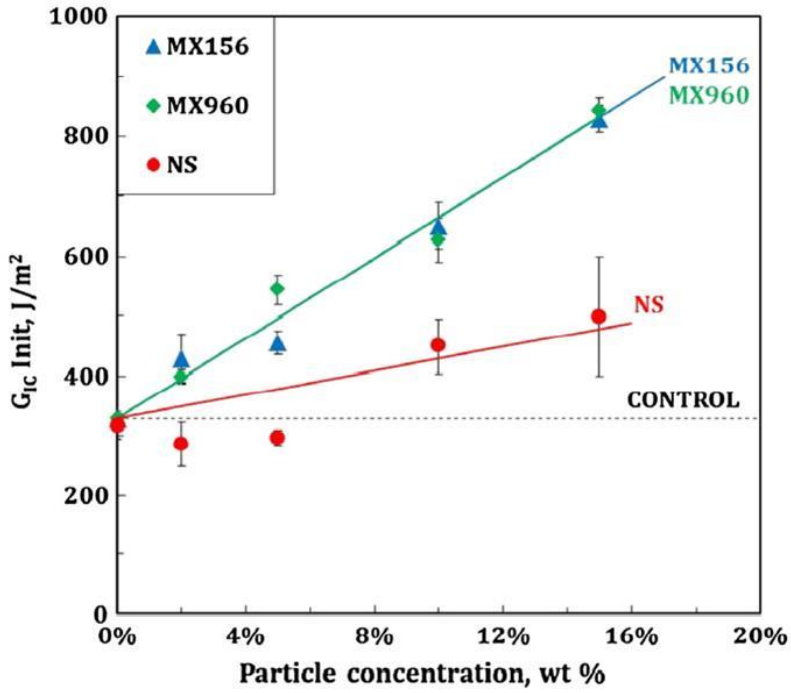

Figure 2.7: Fracture energy vs. particle concentration - MX156: polybutadiene core - MX960: siloxane core - NS: silica nanoparticles [25]

The toughening mechanisms were analysed with electron micrographs. Irrespective of the CSR content, voided particles followed by plastic deformation of the matrix due to void growth were apparent. The diameter of the voided particles increased by almost a factor of two, namely from 58 nm to 110 nm. The 58 nm for the CSR-particles were measured with atomic force microscopy and highlight that the actual diameter is significantly less than the nominal diameter of 100 nm quoted by the manufacturer. However, this larger increase in diameter highlights that the void growth and plastic deformation allows to assume a strong toughening effect due to these mechanisms.

Quan and Ivankovic analysed the toughening effect of two different core shell rubber particles differing in diameter and core material. The two particle types used had a nominal diameter of 300 nm and 50 nm with an acrylic rubber and a butadiene-acrylic copolymer core, respectively. Single-edge notch three-point bending tests were carried out on bulk DGEBA epoxy resin without any fibre reinforcements. Volume fractions ranging from 0 % up to 38 % were tested for the larger particle, whereas the smaller particles were tested in combination with the larger particles with a volume fraction of 22 % and 16 % for the larger and smaller particles, respectively. With increasing fractions of particles dispersed into the resin, the glass transition temperature increased from 122.5 °C to 128.6 °C for the 38 vol% large particle filled resin, whereas the combination of large and small particles yielded an even higher glass transition temperature of 131.2 °C. This is contradictory to other findings, where the glass transition temperature either remained unchanged or decreased [26, 27]. Quan and Ivankovic mention the interface of the matrix and the CSR particles to be the cause for the increased glass transition temperature. The particles hinder chain mobility and therefore impose more restriction for the polymer chains, which is especially the case for the smaller particles with a larger overall surface area.

The fracture energy increases continuously for the larger particles up until 30 vol% of CSR-particles dispersed into the matrix and declines after. The mode I fracture toughness increased from 1.2 $MPam^{1/2}$ to 2.64 $MPam^{1/2}$, which equals an increase by a factor of 2.2. The fracture toughness decreased by 6 % for the 38 vol% large particle filled matrix and by 27.2 % for the mixed-particle matrix. Quan and Ivankovic assume that the decline is due to an amount exceeding the optimal rubber content or due to a higher cross-link density of the matrix.

The initiation toughening mechanism was identified as particle debonding, which was followed by plastic void growth of the matrix. Transmission electron micrographs of a loaded crack tip of the matrix with 38 vol% of the larger CSR-particles is shown in Figure 2.8. It shows the cavitations due to the particle debonding, which is followed by the plastic void growth and deformation of the matrix. Furthermore, shear band yielding was identified as an additional toughening mechanism.

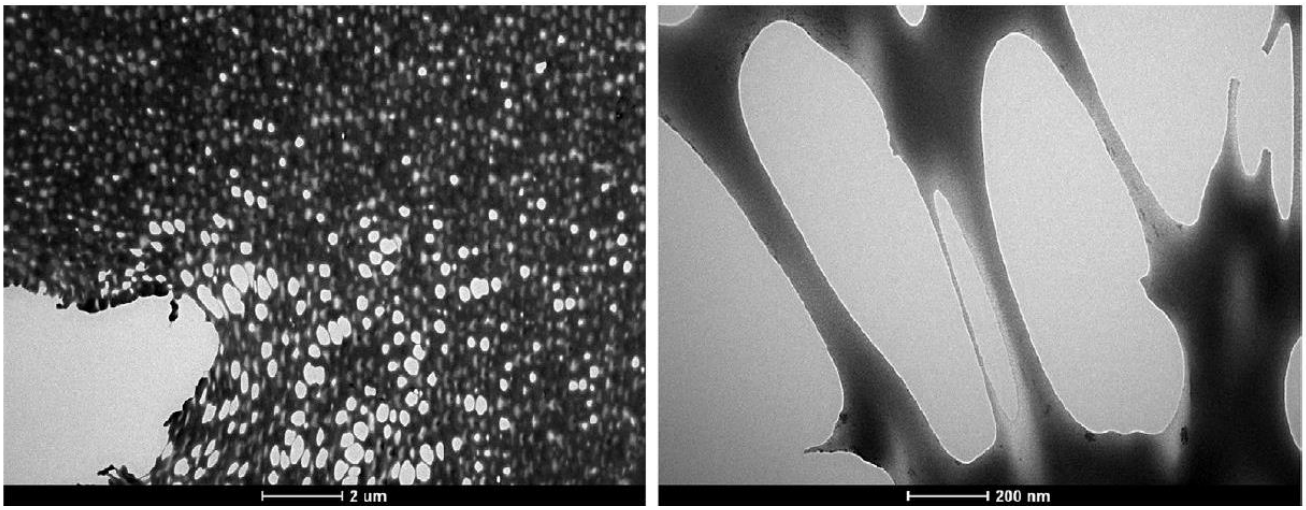

Figure 2.8: TEM images of a loaded crack tip with 38 vol% of 300 nm CSR-particles [28]

Keller et al [19] analysed core-shell rubber nanoparticle reinforcements in fast-curing epoxy resin composites and their influence on the fracture toughness. They used two different particle diameters being 100 nm and 300 nm. The smaller particles had a polybutadiene core, whereas the larger particle had a siloxane core. Both particle types had a poly(methyl methacrylate) shell. For the smaller particle weight fractions of 4.5, 10, 15 and 20 wt% and for the larger particle weight fractions of 4.5, 9, 15 and 20 wt% were used. The fibres used were non-crimped triaxial carbon fibre preform fabrics. To evaluate the fracture properties, single edge notched bending tests were performed. Similar to Awang Ngah and Taylor [25], Keller et al [19] measured the diameters of the CSR-particles using atomic force micrographs. The smaller particles had a diameter of 48 nm instead of 100 nm and the larger particles had a diameter of 110 nm instead of the quoted 300 nm by the manufacturer. This is due to the shell having similar properties to the epoxy resin and therefore are not distinguishable from the matrix making the particles appear smaller. This also causes the actual weight fraction of the rubber core to be less, as the core is included in the initial weight fraction. Figure 2.9 shows the results of the performed tests. The fracture energy increases linearly with increasing CSR-particle content up until 9.1 wt% for the smaller particles and up until 11.5 wt% for the larger particles, which has been 10 wt%

and 15 wt% before curing, respectively. With increasing weight fractions the increase in fracture energy is no longer linear but starts to flatten. The highest fracture energy was achieved with the larger CSR-particles with a weight fraction of 14.5 wt% (initially 20 wt%) yielding an increase by a factor of 14.5 of the original non-modified epoxy resin.

The fracture surface of the CSR-particle modified epoxy resin is rougher in comparison to the non-modified epoxy resin, whose brittleness caused an expected smooth fracture surface. Contrary to Quan and Ivankovic [28], where the particles debonded, Keller et al [19] identified particle cavitation. The bonds between the shell and the resin and between the shell and the core remained intact. The particle cavitation was followed by plastic void growth of the matrix. The particles increased in size by 140 % - 220 % for the larger particles and by 150 % for the smaller particles.

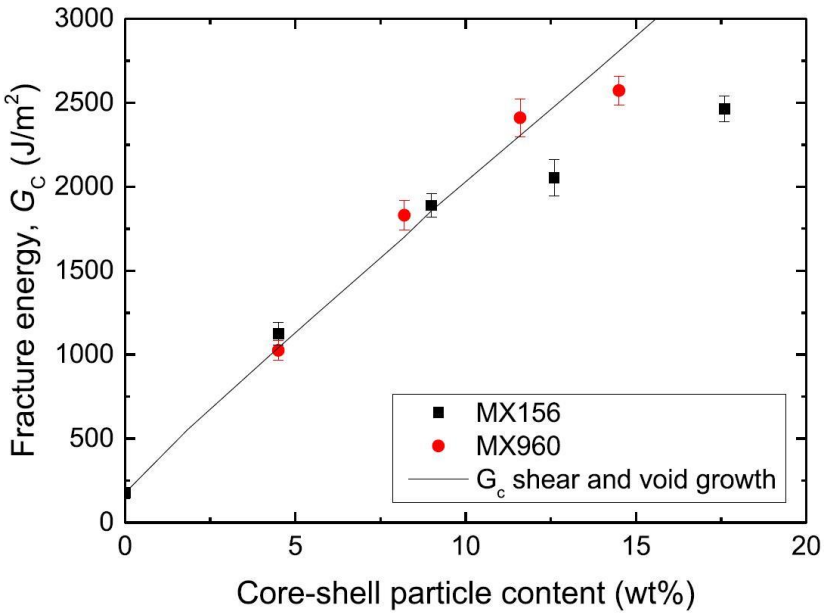

Figure 2.9: Fracture energy vs. CSR-particle content [19]

2.5.1.2 Non-organic particle toughening mechanisms

Previously mentioned toughening mechanisms such as crack pinning or crack deflection are not present in silica nanoparticle toughened systems. Given the particle size in the double-digit to low three-digit nanometre range, the particles are too small in comparison to the crack tip which is usually a few micrometres large according to Johnsen et al [27]. Furthermore, no crack bridging occurs due to the rigidity of the particles and therefore cannot connect the two crack planes, as it is the case for rubbery particles.

The main toughening mechanism has been identified as plastic void growth, where silica nanoparticles debond prior to the plastic void growth [27, 29]. During debonding of the particles less energy is consumed than during plastic void growth, but it is essential so that the latter can occur [27]. This has also been identified by Goyat et al [30] who analysed titanium dioxide nanoparticle modified epoxy systems. The main toughening mechanisms were identified as particle pull out followed by plastic void growth. The particle debonding

created a hemi-spherical hole in which the debonded particle remained. The following plastic void growth has been identified as the main toughening mechanism as well. However, unlike Johnsen et al [27] Goyat et al [30] mentioned crack deflection as contributor to the overall toughening. They differed between crack deflection type I and type II, where type II occurs when the crack propagates around loosely bonded particles. Non-organic particles such as silica nanoparticles increase the toughness, the strength and modulus, but also the thermal conductivity and glass transition temperature. Particles can make the product more cost-efficient, reduce the degree of shrinkage, the exothermic peak during curing and the coefficient of thermal expansion [22].

Bray et al [31] toughened epoxy polymers with silica nanoparticles and analysed the effect of volume fraction and particle size on the toughening performance. The matrix was based on a bisphenol A resin cured with a piperidine hardener. The silica nanoparticles used had average diameters of 23 nm, 74 nm, and 170 nm. The fracture toughness of the bulk resin specimens was measured with a single-edge notch bend test. For all particle diameters volume fractions ranging from 5 to 30 vol% in 5 vol% steps were tested. Also, an unmodified bulk resin system and 2.5 vol% specimens for all particle diameters were tested. The test results are shown in Figure 2.10. It can be seen that irrespective of the particle diameter the fracture energy increases almost linearly with increasing volume fraction of particles. However, the medium sized particles with a 74 nm diameter performed better than the 23 nm and 170 nm silica nanoparticles, where the smallest one had the least increase in fracture energy with increasing volume fraction. The small difference in the results for the different particles including the experimental error allows to assume that the difference in size has a rather marginal influence according to Bray et al [31]. An approximate quadrupling of fracture energy in comparison to the unmodified resin was achieved for the best performing combination of particle diameter and volume fraction, namely 74 nm and 30 vol%. As the tests were carried out on bulk resin specimens, it is safe to assume that the performance is less strong in fibre reinforced epoxy resins, as also highlighted by Garg et al [22].

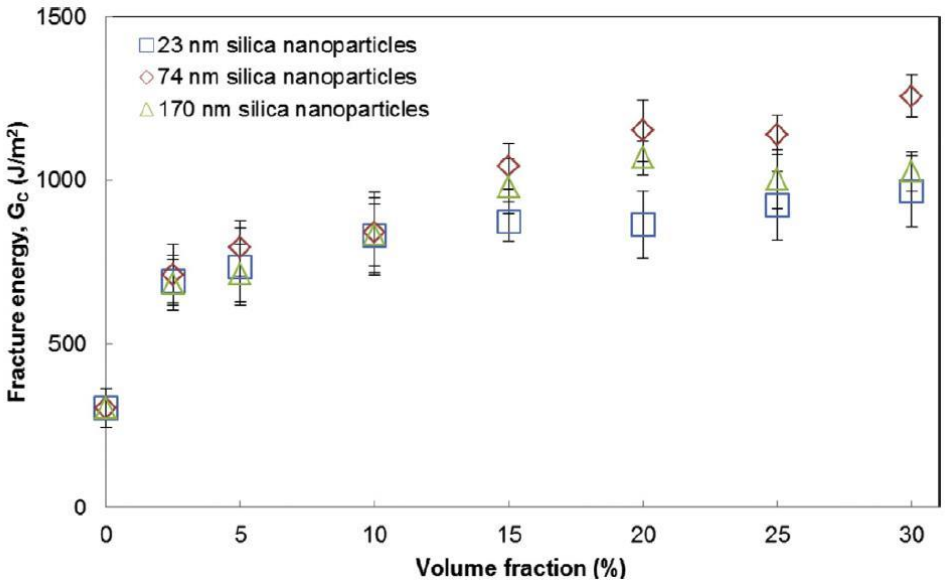

Figure 2.10: Fracture energy versus volume fraction of silica nanoparticles in bulk epoxy resin [31]

The main toughening mechanism identified is particle debonding followed by plastic void growth of the matrix. Figure 2.11 shows a SEM-image of a modified epoxy resin with 10 vol% of 170 nm silica nano particles. The arrows highlight particles still embedded into the matrix, whereas the circles show debonded particles including the plastically grown matrix around. Furthermore, localised shear band yielding has been identified as another toughening mechanism.

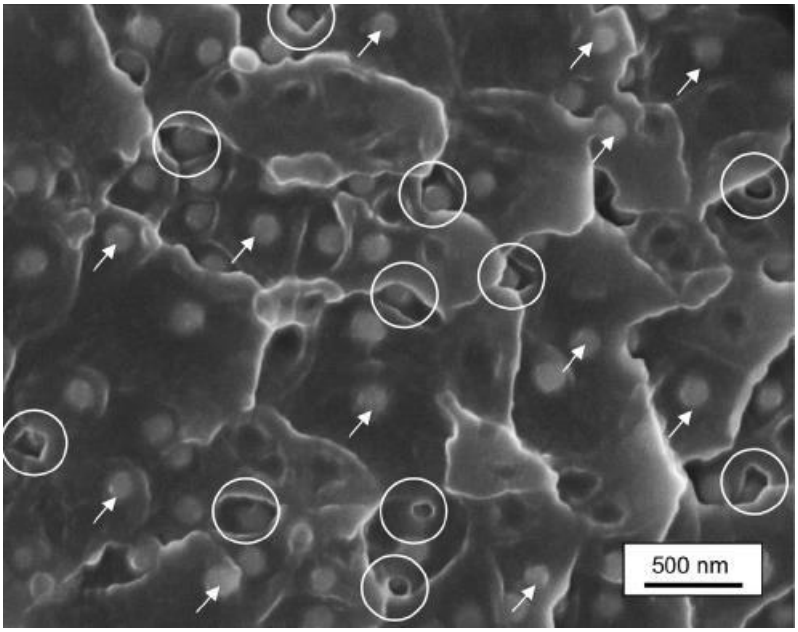

Figure 2.11: SEM images of epoxy polymers containing 10 vol% of 170 mm diameter silica nanoparticles [31]

Keller et al [20] performed tests on silica nano particle modified bulk fast curing epoxy resin systems. The particles had a diameter of 20 nm and concentrations of 10 wt% and 20 wt% were used. To determine the fracture toughness single-edge-notched bending (SENB) was performed. The results from the SENB-tests showed no significant increase in fracture toughness, which was supported by the SEM-images, which no toughening mechanisms usually induced by hard filler particles, such as debonding and plastic void growth. This can be due to the fast-curing resin system but was not further discussed. Shear bands were identified, but this toughening mechanism can also occur for non-modified epoxy resin systems.

Hsieh et al [26] analysed the toughening performance of silica nano particles in bulk resin and in glass-fibre reinforced composites. The used resin was based on a diglycidyl-ether of bis-phenol A (DGEBA) and the silica nanoparticles had a diameter of 20 nm. The concentrations tested ranged from 0 to 20 wt%. The bulk resin specimens were tested with a single-edge notch-bend test, whereas for the glass fibre composite a double cantilever beam test to evaluate the mode I fracture toughness was used.

For the bulk resin, the fracture energy increased from 77 J/m² to 212 J/m² for the specimens with 20 wt% of silica nano particles dispersed into the matrix. The fracture surfaces with and without silica nanoparticles did not differ clearly, as both had a brittle appearance with crack forging and feather markings. However, scanning electron microscopy showed voids around the silica nanoparticles, suggesting that particles debonded, which results in an increased fracture energy and therefore increased the toughness. The mean fracture energy for

the glass-fibre composite specimens increased from 330 J/m² to 1015 J/m² and decreased from 718 J/m² to 626 J/m² for unidirectional and quasi-isotropic layups, respectively. Both types had 10 wt% of silica nanoparticles incorporated into the matrix.
For the unidirectional GFRP the toughening effect is mainly due to fibre bridging, which was increased due to the presence of silica nano particles. For the quasi-isotropic layup, the fracture surface looked rather brittle. Kinloch et al [21] analysed the results of mode I and mode II fracture tests of GFRP composites, whose matrices were modified with silica nanoparticles. The particles used had a diameter of 20 nm and the matrix was a standard DGEBA resin. For the mode I fracture energy double cantilever beam testing was performed, whereas for the mode II fracture energy end-loaded split (ELS) tests were used.

2.5.1.3 Thermoplastic toughening mechanisms

Toughening mechanisms in thermoplastic modified epoxy systems show a mix of both elastomeric toughening behaviour but also nonorganic particle toughening behaviour. This is because of the particles being more ductile and tougher than inorganic particles, but also more rigid than elastomeric particles. Common toughening mechanisms are crack bridging, crack pinning, crack path deflection, shear banding and particle yielding according to Díez-Pascual [32].
In the crack bridging mechanism, the particles hold the two crack planes together while being stretched. This tensions the particles and causes the stress at the crack tip to be lessened. Due to the more rigid nature in comparison to elastomeric particles, it is not unlikely for the particles to tear apart in a more brittle manner. This particle tearing caused by the crack bridging consumes energy and makes the system tougher.
The crack pinning behaviour is similar to the pinning mechanism mentioned in the previous chapters, whereas it is more likely to happen with thermoplastic particles than with elastomeric additives.
Furthermore, similar to the inorganic particles, particle yielding induced shear banding causes stress concentrations, which eventually leads to shear banding in the matrix. According to Díez-Pascual [32] the most significant toughening mechanism in thermoplastic toughened epoxy resins is the particle-yielding-induced shear banding.
Thermoplastic materials can also act as tougheners of epoxy resin systems. A commonly used thermoplastic material is phenoxy resin, which is not added to the liquid resin, but incorporated into the layup process. It is a thin film interleaved between the carbon fibre plies. By adding thin films into the laminate, resin flow is hindered until the phenoxy film melts, which can cause increased infusion times. The study performed by Van Velthem et al [33] yielded an interlaminar fracture toughness increase of 100 – 150 %. However, the results are supported by the similar structure of the used resin – namely RTM6. The performance of phenoxy with other resins is not covered, but given the thermoplastic and therefore ductile nature, an increase in fracture toughness is expected. Phenoxy is also available as a powder and as fibres, which can be used to improve the resin flow and impregnation of the preform. Furthermore, the temperature range needs to be compatible to the curing cycle.

2.5.1.4 Hybrid toughening

Kinloch et al [21] analysed the behaviour of hybrid-toughened epoxy polymers by adding multiple plasticisers, namely a reactive liquid rubber and silica nano particles. Similar to the previously mentioned findings, an increase in interlaminar fracture toughness was achieved. This is supported by the work of Lobanov et al [34], who also mention the combination of different plasticizers. Yet, it is also highlighted that said combination, the volume fractions and geometry are dependent on the manufacturing process, the product, and the resin. Due to the generally higher viscosity of additives, the infusion time is likely to increase when using an RTM process. Furthermore, the compatibility to the resin needs to be given, as highlighted by Van Velthem et al [33].

2.5.2 Interlaminar layers

To improve the interfacial bond of the metal plate to CFRP, an option is to incorporate short fibres into the interface. As continuous fibre reinforced composite laminates have a resin rich region in the interface between adjacent plies, this resin rich region can be turned into a short fibre reinforced resin by incorporating chopped fibres [35]. The approach is similar to other interleaving approaches such as thermoplastic films, but a major benefit is the marginal weight and thickness increase that comes with it. Furthermore, including this step into the production has a negligible influence on the cycle time and cost [35, 36].
The approach was initially developed by Sohn et al [37], who analysed compression moulded CFRPs with aramid fibre reinforced interfaces. The motivation was impact damage causing unwanted multilayer delamination in continuous fibre composites, whereas chopped or short fibre reinforced plastics show localised and less critical damage. A visualisation is shown in Figure 2.12.

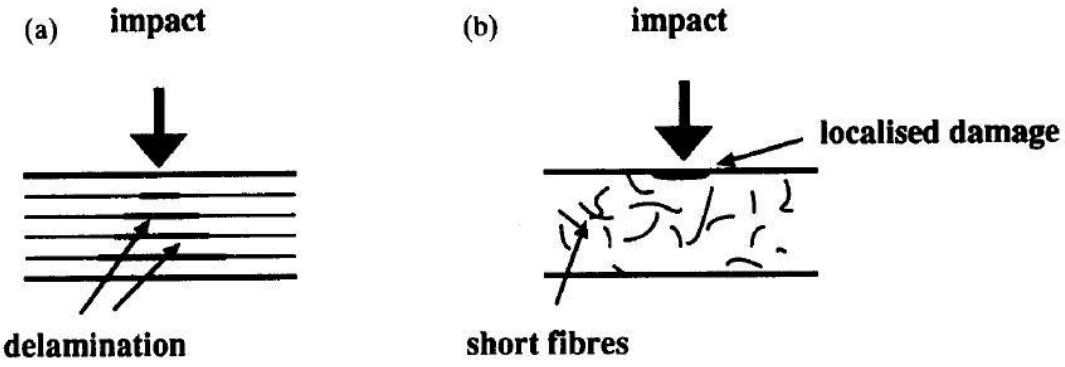

Figure 2.12: Impact damage in (a) continuous-fibre laminate and (b) short-fibre composite [37]

By combining both, the weak spot located in the interlaminar phase resulting in delamination is reinforced and the fracture toughness can therefore be increased. Furthermore, matrix modifications such as adding additives increases the overall fracture toughness, but an increase in delamination toughness cannot

necessarily be expected [37]. The main toughening mechanism is fibre-bridging causing multiple modes of energy dissipation, namely matrix spalling, fibre pull-out and fibre fracture in form of tensile fracture and fibre splitting [35–37].

The performed research done in that field mostly considered pre-impregnated glass or carbon fibre tapes and aluminium sandwich cores, but minimal information is given on interface toughening of metal-composite hybrids which are in-situ cured with resin transfer moulding. However, Sohn et al highlighted that it is easier to place the chopped fibres in the desired location instead of injecting a chopped fibre resin mixture, which also offers better distribution control [36].

Yasaee et al [38] performed similar tests and derived a model to estimate the improved impact resistance and increased interlaminar toughness by incorporating chopped aramid fibres in the interface. An 123 % increase for the mode II energy release rate was achieved, which is in line with previously reported experiments mentioned by Yasaee et al [38].

Further tests on metal-CFRP interfaces were performed by Sun et al [36], which focused on the aramid fibre length, on the surface treatment of the aluminium substrate and on the aerial density of the aramid fibres. Fibre lengths of 6 to 14 mm were tested and compared with a double cantilever beam test setup. The shortest fibres yielded an interfacial toughness increase by a factor of 1.8 and gradually decreased for increased fibre lengths, where the 14 mm long fibres yielded an improvement by a factor of 1.2. The weight increase compared to a non-short fibre reinforced specimen was 0.18 % for an aerial density of 12 g/m².

Furthermore, different surface conditions paired with 6 mm long aramid fibres in the interface were tested with an asymmetric double cantilever beam test. Depending on the surface treatment an increase in fracture toughness by a factor of 1.5 up to 20 was obtained. The highest relative increase was for the surface treatment with a pattern similar to the weaved carbon tape. The highest absolute performance was reached with an aluminium foam. The conclusion based on that by Sun et al [39] highlighted that an increased roughness of the aluminium substrate is proportional to the increased fracture toughness, as the aramid fibres have higher chances of interlocking in the substrate. A cross-sectional view of an aramid toughened interface is shown in Figure 2.13.

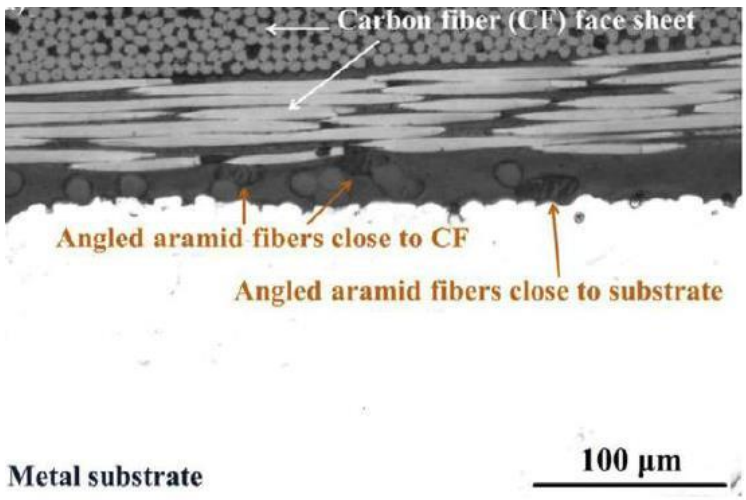

Figure 2.13: Short aramid fibre toughened interface [39]

By comparing different aramid fibre densities, where 3 g/m², 12 g/m² and 50 g/m² with fibre lengths of 6 mm and 14 mm were used, a clear trend was obtained by Sun et al [40]. The fracture toughness increases with increasing fibre density but flattens between 12 g/m² and 50 g/m² suggesting that using 12 g/m² is a good compromise between performance and added weight. Furthermore, the different fibre lengths yielded slight performance differences with the 14 mm fibres performing slightly better. The fracture toughness results were obtained with a 3-point-bending test.

2.6 Non-destructive testing

For composite structures various non-destructive testing (NDT) techniques and methods are available. Given the large number of damage types to occur and some of them being barely to not visible at all, it is crucial to have processes to be able to test the part's quality without adding further damage during testing. A commonly used term for this damage is the so-called barely visible impact damage (BVID). By using NDT, manufacturing defects can be identified, but also damage zones after the product has been used in field or was damaged during manufacturing due to a tool dropping on the structure for example. Common NDT techniques are manual inspection methods, ultrasonic testing and optical methods.

Manual inspection methods include visual inspection of the component, but also analysing the sounds a structure makes when tapping on it with something rigid such as a coin can provide information on potential damage. However, more precise and detailed information can be gained by ultrasonic testing.

Ultrasonic testing gives insight into the internal state of a structure by transmitting ultrasonic waves through the material. Depending on the materials, the waves propagate with different speeds through the structure, which can then be used to identify voids or delaminated areas for example. Ultrasonic waves have a frequency above 20 kHz and propagate well in liquids and solids but travel only for short ranges in gases. Commonly used wave frequencies can be categorised into two groups, namely low frequency testing around 20 to 1000 kHz and high frequency testing, which is above 1 MHz. The low frequency testing is used for analysing delamination areas or other imperfections and defects in the structure [41].

The two main waves propagating through a body is either longitudinal or shear, although other wave types co-exist [42, 43]. Longitudinal waves are more common than shear waves, as they can travel in both liquids and solids and are faster than shear waves [42]. Shear waves can only propagate in solids. A schematic of both wave types is shown in Figure 2.14. The longitudinal wave is also called compression wave, as the particles' vibration is going in the same direction as the wave propagation. Those waves cause density variations in the material. Shear waves or transverse waves cause the particles to move under an right angle with respect to the wave propagation. [42]

The flaws in the structure are identified by reflections or scatter at the boundaries between different materials and media resulting in spikes in the monitoring. At those boundaries, a part of the wave is reflected, whereas the other part continues to transmit through the material. The fraction, how much of the wave is reflected depends mainly on the wave velocity, material density and the beam incident angle [42].

The product of the wave velocity and the material density yields the acoustic impedance. Only, if the impedances of two adjacent materials differ, a fraction of the wave will be reflected. Otherwise, the entire wave will transmit through the boundary without any reflection. To detect flaws in composites, the different acoustic impedances of the fibres and the surrounding matrix needs to be kept mind, as these result in inevitable boundaries. However, an overall impedance can be derived for composite materials, so that delamination and voids can still be identified. At boundary layers, where reflections occur, longitudinal waves can cause shear waves to be initiated. This is called mode conversion. Figure 2.15 shows this phenomenon schematically.

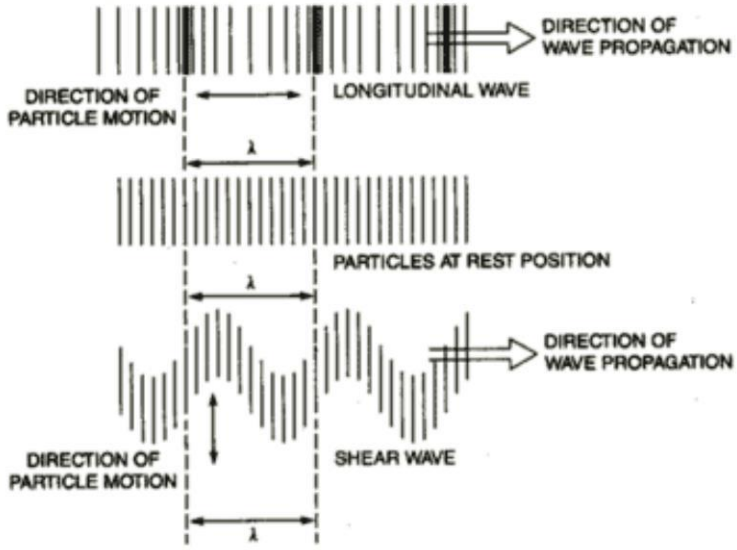

Figure 2.14: Schematic of longitudinal and shear waves [44]

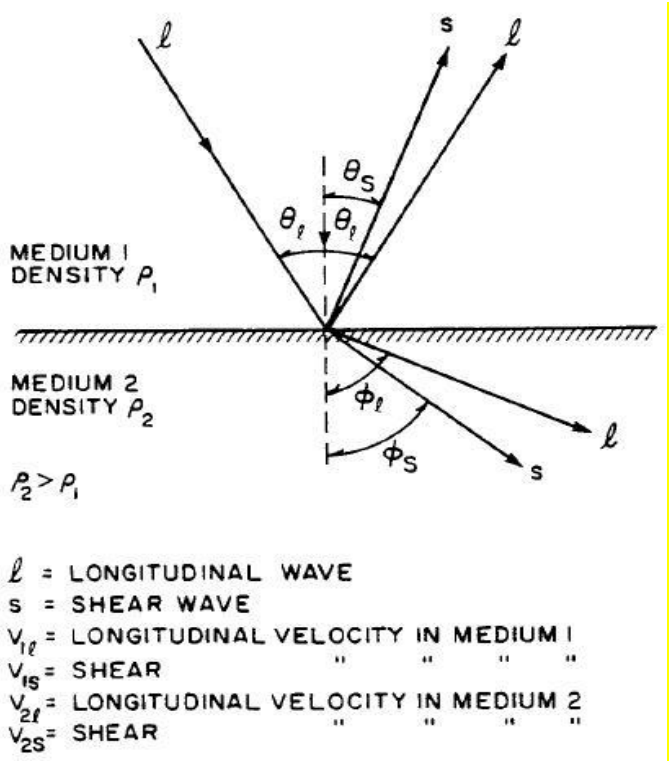

Figure 2.15: Reflection, refraction and mode conversion at a boundary of two different materials [42]

The position of the flaw can be identified by using the wave velocity in the different media. By relating this to the time the wave propagates through the material, the in-depth position can be identified. Furthermore, properties such as attenuation and wave velocity can be used to identify damage. There exist two methods used to send and receive the ultrasonic wave. In the pulse-echo method only one transducer is used, which acts as both the sender and receiver, but also two separate transducers adjacent to each other can be used. It is placed onto the structure to be tested. The pitch-catch method works with two transducers, where one is responsible for sending and the other one receives the signal. For the pitch-catch method, usually the receiver is on the other side of the structure, so that the ultrasonic waves travel through-thickness only once.
Commonly used scanning methods are A-scan, B-scan and C-scan. However, also other testing methods such as M-scan exist [45].
Using A-scan provides a 1-dimensional view of signal amplitude versus time. It shows the intensity of the reflected signals as a function of time (see Figure 2.16). The A-scan method works with a single transducer and therefore with the pulse-echo method. By post-processing the data, the time-of-flight can be correlated to a distance travelled. This information can be used to identify the in-depth position of the damage in the structure.

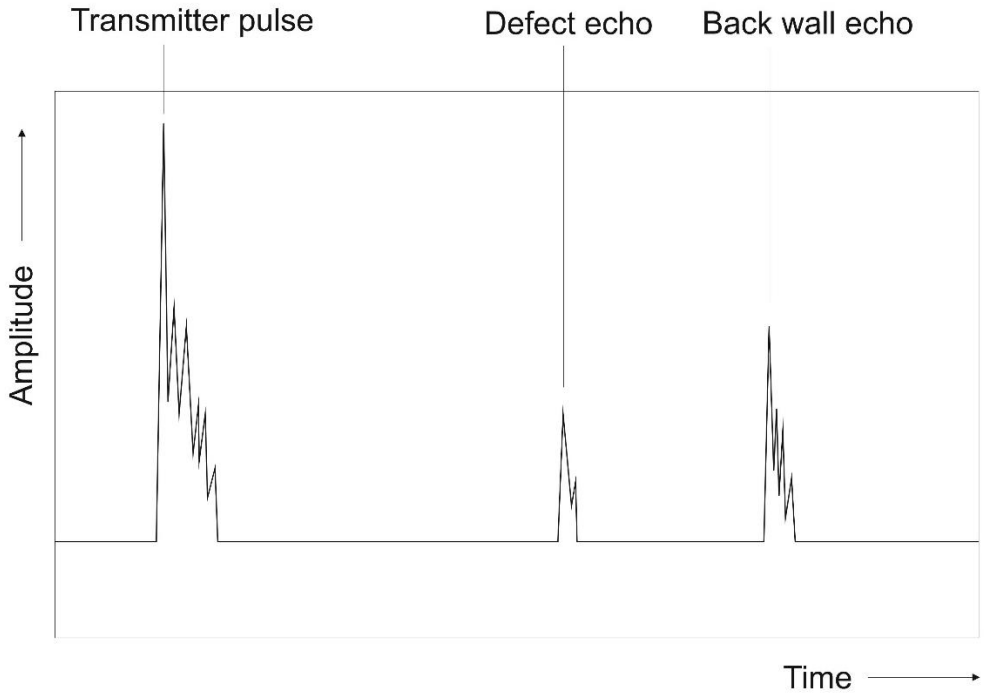

Figure 2.16: Typical plot for A-scan using the pulse-echo method [46]

The B-scan method is an extension to the A-scan method. With B-scan a cross-sectional view of a structure is obtained, which provides a two-dimensional array highlighting defect positions in the in-depth orientation and horizontal orientation. The cross-sectional view is put together by multiple A-scan measurements.
Different from the A- and B-scan, C-scan gives no information about the in-depth position of defects, but instead provides a surface view of the structure. It highlights where in a structure defects are from a top view, but to identify the in-depth position, A-scan is needed. [41]

A-scan is usually performed by handheld instruments using the pulse-echo method. By using a liquid couplant, which is grease, oil or water often [47, p. 16], the transducer is moved manually over the surface. The signal received should show a clear spike for the backwall. This offers the ability to detect any potential damage such as delamination, as beginning and end of the signal are clearly identifiable. By moving the probe over the surface, it can also be possible to create a cross-sectional B-scan image. [41]
C-scan is mostly done automatically due to the more complex setup. For C-scan the pitch-catch method is applied, which requires an emitting transducer on one side and a receiving transducer on the other side. This through-transmission measurement requires water jets to ensure proper coupling without any gaseous media present. In some cases, it is also possible to fully submerge the structure into a water tank, which acts as a couplant. However, depending on the geometry of the structure impose a risk to damage the structure due to water ingress. This automated C-scan yields a surface view of potential damages, which can be further analysed with A-scan to determine the in-depth location of the damage. [41]

2.7 Peel tests

To analyse the performance of the interface between the metal and the carbon fibre composite, peel tests can be used to analyse and compare the bond between the mentioned components. Different peel test setups are available. Depending on the setup, a mandrel is used, which is used to avoid or reduce plastic deformation of the adherend being peeled off. Commonly used and standardised test setups are the floating roller peel test [48], the climbing drum peel test [49] or the T-peel test [50]. Variations of the test standards exist, where the T-peel test can be modified into a variable angle fixed arm peel test. This allows for other angles between the two adherends to be tested [51]. Furthermore, a so-called mandrel peel test can be conducted, which is a more direct experimental route to determine the adhesive fracture toughness according to Kawashita et al [51]. For all peel tests, a flexible adherend is peeled off from a rigid adherend, which is adhesively bonded together.

2.7.1 Floating Roller Peel

The floating roller peel test setup is an apparatus, which can be attached to a standard tensile testing machine. The peeling is done by performing a displacement controlled tensile movement to peel off the flexible adherend from the rigid adherend. The apparatus has two mandrels, which hold the rigid adherend, but also provide support for the flexible adherend, so that it can conform to the mandrel radius to reduce plastic deformation.

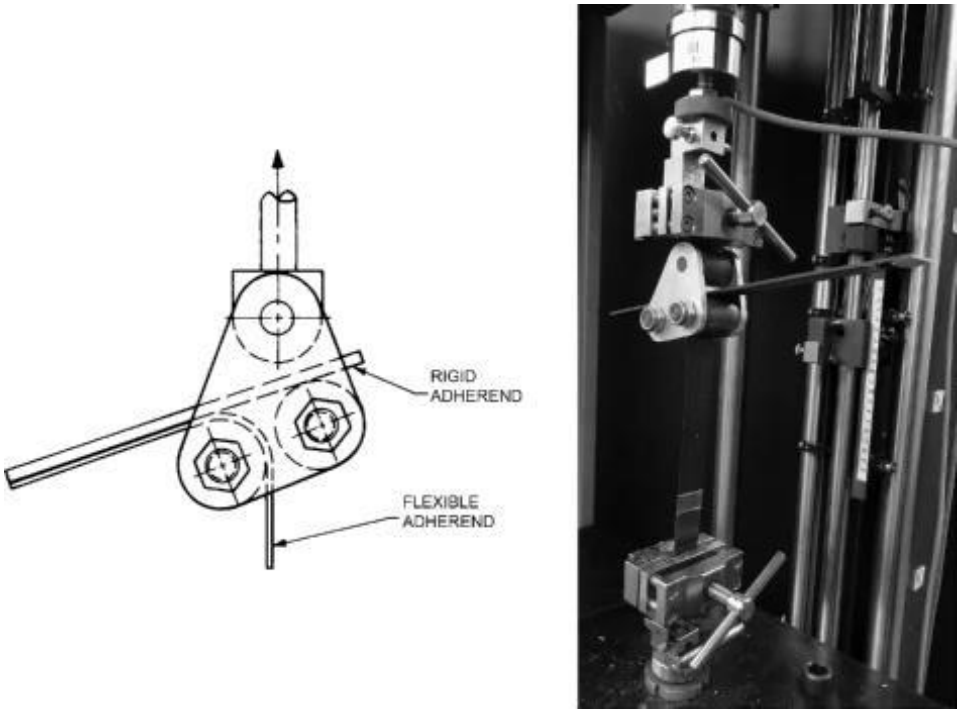

Figure 2.17: Floating roller peel test setup [52]

2.7.2 Climbing Drum Peel Test

The climbing drum peel test is using a similar mandrel, as it is the case for the floating roller peel test. However, in this case the mandrel is significantly larger (see Figure 2.18). This peel fixture allows for only peeling forces to occur making the measurement less prone to scatter or other influences. Furthermore, both a rigid and a flexible adherend is used for this peel test as well. [53]

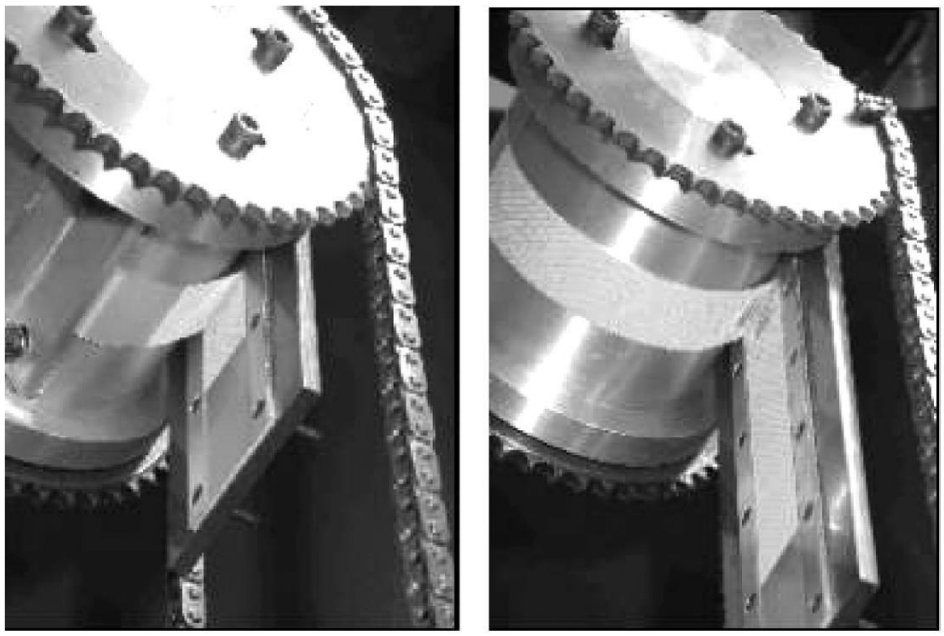

Figure 2.18: Climbing drum peel test setup [51]

2.7.3 Variable Angle Fixed Arm Peel and T-Peel Test

Both the variable-angle fixed-arm peel test and T-peel test are done without any mandrel. For the variable-angle fixed-arm peel test it is possible to change the angle under which the flexible adherend is peeled off from the rigid adherend (see Figure 2.19). This offers the possibility to test different fracture mode combinations, where a 90°-peel angle is mostly mode I and where a 0°-peel angle would be mostly mode II. However, usual test angles range from 45° to 135°. [51]

The T-peel test has a peel angle of 180°, where both adherends need to be flexible (see Figure 2.19). The ends of each adherend are positioned in opposing tensile grips and with a defined and constant rate of displacement the force needed to peel the two flexible adherend apart is measured. [54]

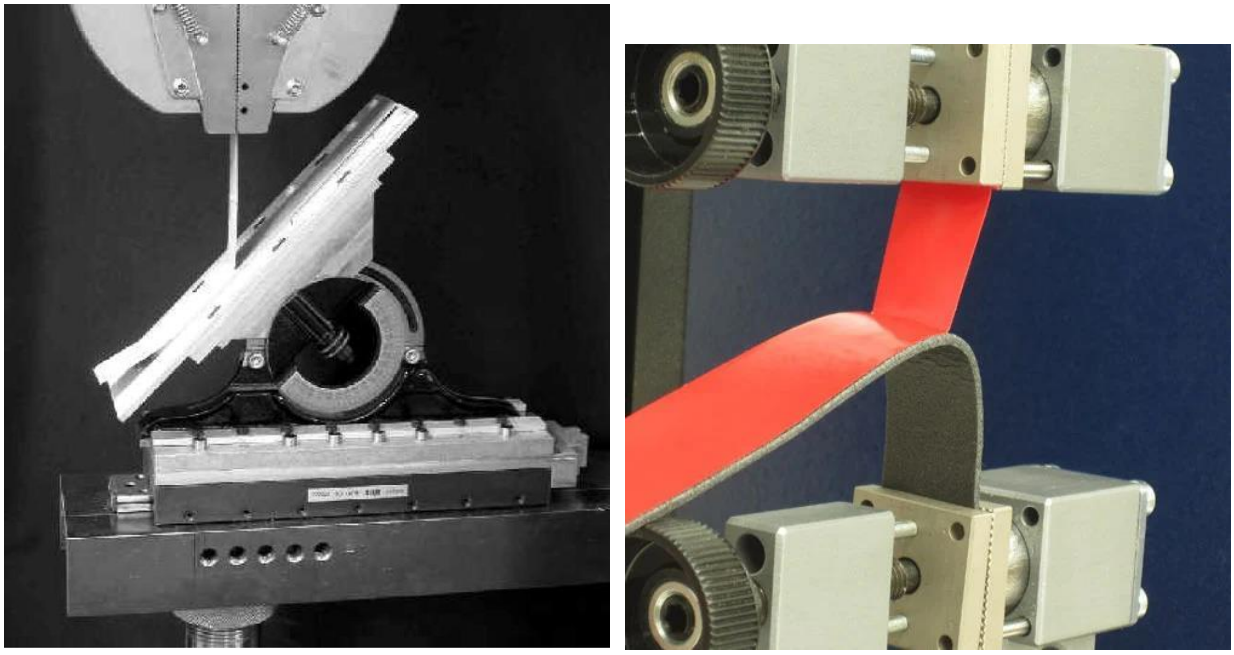

Figure 2.19: Variable-angle fixed-arm peel test [51] (left) and T-peel test according to ASTM D1876 [54] (right)

2.7.4 Mandrel Peel Test

The mandrel peel test peels a flexible adherend off of a rigid adherend. The laminate is positioned on a sliding table, which has a low friction to avoid deviations of the results due to friction. The flexible adherend is peeled off using a tensile force, which causes the peeling at the mandrel (see Figure 2.20). The mandrel acts as a guide to avoid plastic deformation, as this consumes energy as well causing the results to be less precise. Depending on the material's stiffness and elongation at break the mandrel radius needs to be adapted. Usually, too small radii can cause the flexible adherend not conforming around the mandrel, similar to what can be seen in Figure 2.21. However, in this test an alignment force can be applied, which tensions the laminate and therefore makes the flexible adherend conform to the mandrel more likely. The mandrel peel test resembles a mixed mode propagation. [51, 55]

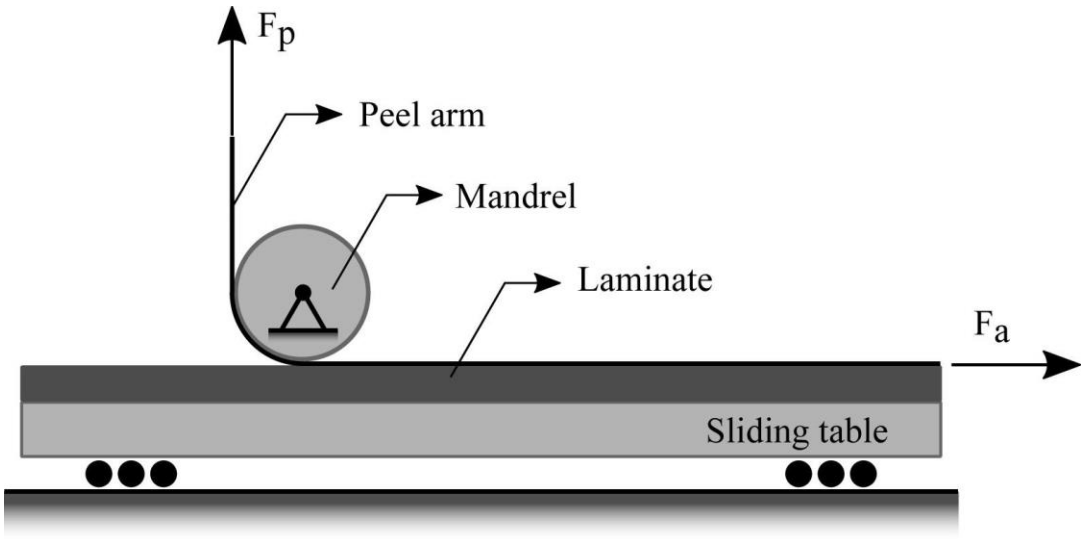

Figure 2.20: Schematic of a mandrel peel test setup [56]

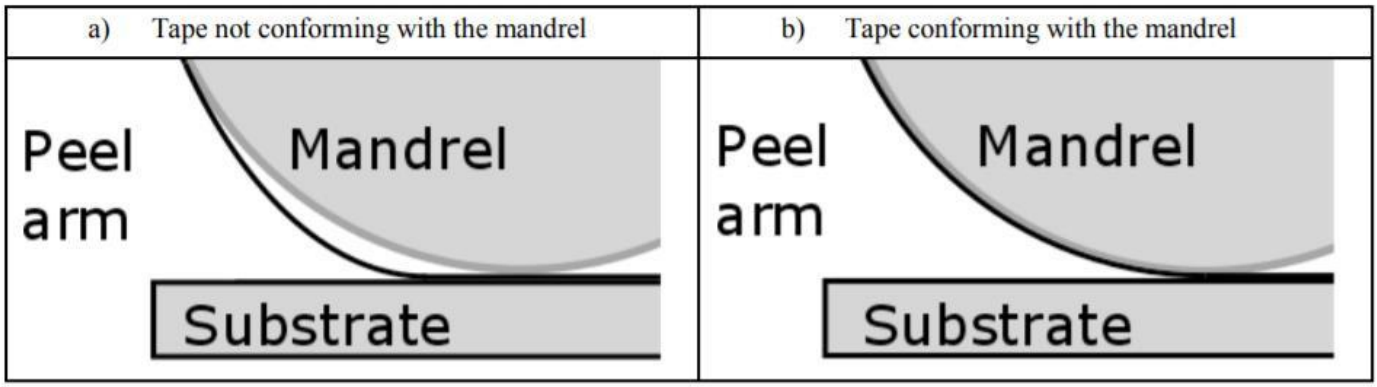

Figure 2.21: Conformity of the flexible adherend to the mandrel during a peel test [55]

2.8 Synthesis

An extensive literature review showed that both additives such as core-shell-rubber particles or silica nanoparticles can have a positive effect on the fracture toughness and therefore damage tolerance. Also, binder materials can have beneficial or detrimental effects on the damage tolerance. Furthermore, interface materials such as short fibre veils or weaves can improve the bond between fibre reinforced plastics and metals. The performed literature review shows that modifying the matrix with additives, but also interface materials in metal-CFRP hybrid structures can improve the fracture toughness of the material. Apart from that, different test setups were reviewed to understand, how possible toughness improvements can be tested. Based on the insights gained, the following test scope for the matrix toughening has been identified (see Figure 2.22). The impact performance is assessed based on the peel force for the interface materials and based on the energy loss and damage area for the matrix toughening.6wt%

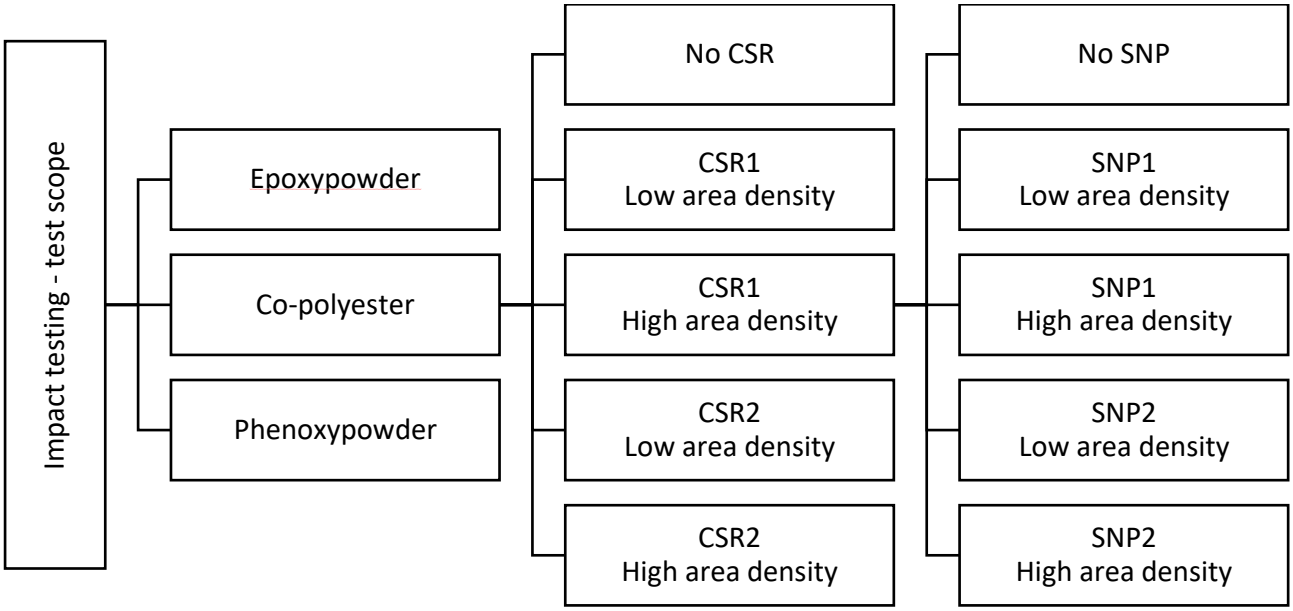

Figure 2.22: Tree diagram for the matrix toughening test scope - additives and binders

Similar to the matrix toughening test scope, a test scope based on literature review was defined for the interface toughening and is shown in Figure 2.23.

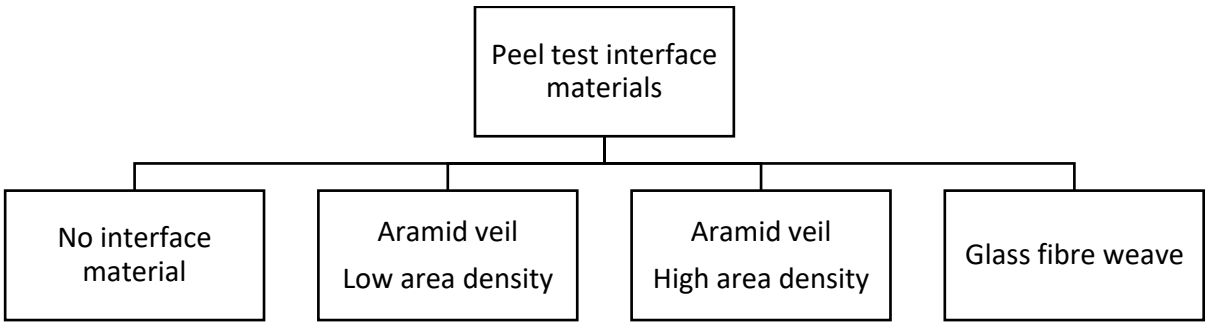

Figure 2.23: Test scope - interface materials

3 Materials and sample preparation

For this project, it is the goal to perform two individual tests, where one tests focuses the matrix toughening with additives inside the matrix and the other test focuses on the interface strength by incorporating different materials. The goal is to identify the influence on the impact performance, where the hypothesis based on the literature review is that an increasing additive content yields higher toughness. Furthermore, interface materials such as short-fibre aramid veils are expected to increase the interface strength over a given baseline. This chapter highlights the materials, that are identical for both experiments, as they are defined as constant. Furthermore, the manufacturing process used for both experiments is explained. Then, the interface toughening and matrix toughening both in regard to materials and sample preparation is further described.

3.1 Communal base materials

Both experiments are consisting of the same basis of materials. The materials kept identical are fabric materials composing most of the CFRP-body, the non-modified resin system and the steel sheet.

3.1.1 Fabrics and resin system

The used carbon fibre material is a biaxial non-crimp fabric. The used resin system is a fast curing resin system made from bisphenol A combined with an amine hardener.

3.1.2 Steel sheet

The used sheet metal is a stainless steel, which has a modified surface to increase the surface area and allow for mechanical interlocking between the resin and the steel sheet.
Figure 3.1 shows blue tape at the right side. This area is 50 mm wide and is included in the peel specimen. This tape is temperature-resistant for temperatures up to 180 °C and is made from polyester. It is used to initiate the peeling between the steel sheet adherend and the carbon fibre reinforced epoxy adherend. To ensure proper separation after curing, the data sheet suggests using release agent. So, both the metal surface in that area and the tape's surface was covered in release agent.
All steel sheets were cleaned with acetone and plasma treated with atmospheric plasma to further clean the surface to improve the interface to the epoxy matrix. The plasma treatment was not performed in the area where the blue tape for the peel specimens was placed. In addition to that, the other side of the steel sheet has been covered in release agent to be able to easily remove any excess resin, which reached the top surface during the injection process.

Figure 3.1: Steel sheet for peel specimens – peel area blurred

3.1.3 Ply cutting

The plies were cut manually with a stencil, so that the geometry of each individual ply is constant throughout all specimens. The plies were cut with a rolling knife. A photo is shown in Figure 3.2.

Figure 3.2: Cutting of plies (left: 0/90 - right: +-45)

3.2 Resin transfer moulding

The used mould for the specimens is an RTM mould for injection pressures up to 10 bar. The mould consists of a rectangular cavity allowing to produce laminates in the dimensions of 290 x 90 mm². This mould is designed for material and process development and includes cavities close to the inlet and outlet side of the mould which are filled with resin. Those resin samples have a size of 64 x 16 mm² with a thickness of 1.9 mm at the inlet side and 1.0 mm at the outlet side. Those resin samples are cured with the exact same conditions in terms of curing time and temperature and allow for more detailed material physics characterisation. Furthermore, the mould is designed in such a way that different laminate thicknesses can be produced. This allows for specimens with the thickness of either 2 mm, 3 mm or 4 mm. The resin sample thickness is unaffected. Figure 3.3 shows a drawing of the RTM mould. It can be seen that the inlet is located inside the specimen, which is not circular, but has an oblong flow channel.

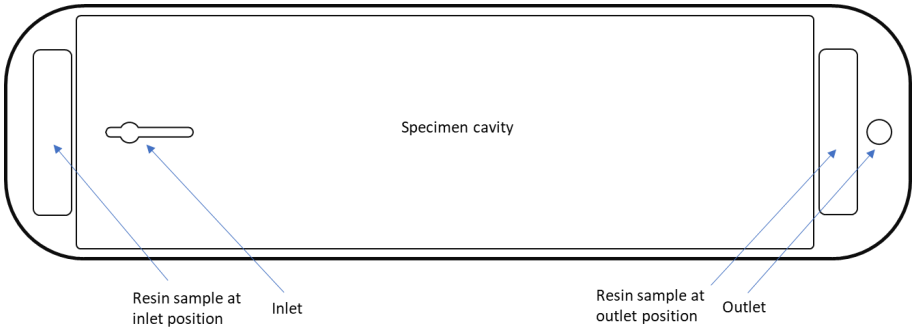

Figure 3.3: Drawing of the RTM mould

After all preparations, the CFRP-steel hybrids were manufactured with resin transfer moulding. For that, the preform is placed into the mould's cavity (see Figure 3.4). Around that is a frame that is used to be able to manufacture different specimen thicknesses, as it was mentioned before. The cavities for the resin samples are located in the other mould half. After positioning the preform in the cavity, the prepared steel sheet was added to the stack. The mould was closed and sealed with screws.

Figure 3.4: Preform positioned in RTM mould

In a next step, a vacuum pump evacuated the mould until reaching a defined level. The valve turns on whenever the threshold of the defined level is surpassed. The better the imperviousness of the entire system, the less frequent are the switching operations of the valves. Therefore, this was used to check the vacuum stability. Switching operations in the low one digit minute range are considered exceptionally good, whereas switching operations in a range of a few up to 30 seconds was considered too fast. This usually indicated an issue with the seal. Possible reasons are insufficient tightening of the screws, fibres on top of the seal allowing air to breach through or issues with the vacuum hoses and their connectors to the mould.

Only, when vacuum stability was considered good, the injection was performed. Prior to injection, the mould was heated to a defined temperature to reduce viscositury and improve the injection process and part quality. The resin is injected from a modified pressure tank. This modified pressure tank allows to draw the resin mixture into the tank with an applied vacuum at the lid (see Figure 3.5). The resin was mixed at 500 rpm for three minutes with a dissolver mixer if no additives are added. With additives, the additive resin mixture was mixed for three minutes without hardener and then two minutes with hardener.

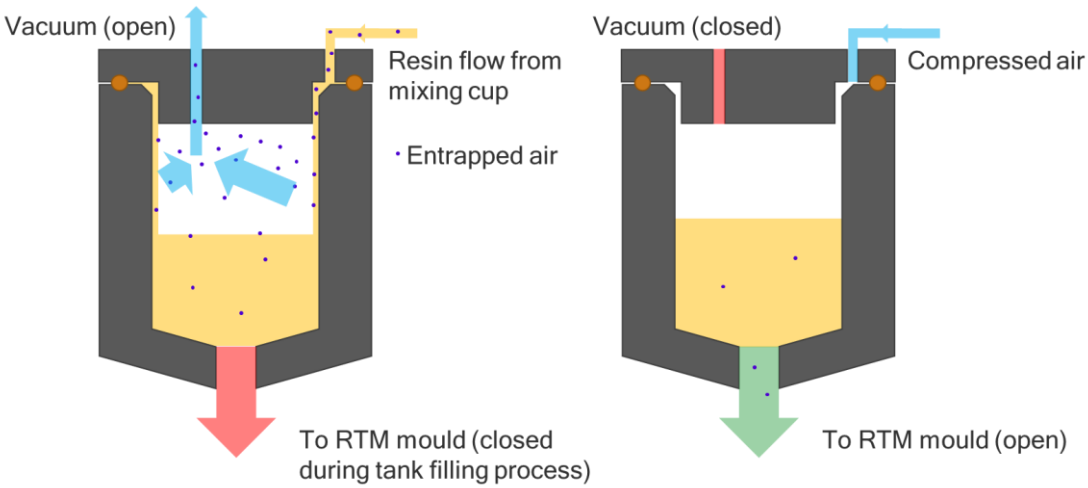

Figure 3.5: Pressure tank filling process

A defined and controlled flow of material along the walls combined with the applied vacuum allows for removing entrapped air. However – as also highlighted in the figure – the air is not removed entirely. Once everything of the resin mixture is drawn into the tank, the vacuum hose was removed from the connector and replaced with a filler plug. After that, the hose which has been used to draw the material into the pressure tank, is connected to compressed air to increase the pressure difference during injection. As the inlet in the mould is located not outside but inside the part, the resin was drawn into the mould with the vacuum without applying additional pressure. This was done to avoid fibre wash out. Only after the resin reached the inside of the mould, the additional pressure was increased to 1 bar.

The chosen curing cycle is a variothermal cure cycle reaching about 105 °C. After the cycle is finished, the part and the resin samples were demoulded. Cleaning the surfaces from resin residues and applying release agent was sufficient to prepare the mould for the next part.

3.3 Matrix toughening

In regard to the overall fracture toughness modifications, several components are considered. The first part is the binder material, which is needed for preforming, but which simultaneously can increase the toughness. For that, different options are available, which are polymers usually. Then, silica nano particles are considered, which can have different particle diameters and different base resins they are dispersed in. In addition to that, the coating of the particles may differ. Another component considered are core-shell rubber particles. Similar to silica nano particles, they come in different diameters and can also be dispersed into different resin systems, which are usually based on either Bisphenol A or Bisphenol F. Figure 3.6 shows a simplified tree diagram for the different additives and binder materials used for the impact specimens.

The used core-shell rubber particle is dispersed in a Bisphenol A resin and the particle diameter is around 200 nm with a concentration of 33 wt%. The silica nanoparticles are dispersed in a Bisphenol F resin. The particle diameter is 20 nm and the weight fraction in the master batch is 40 wt%.

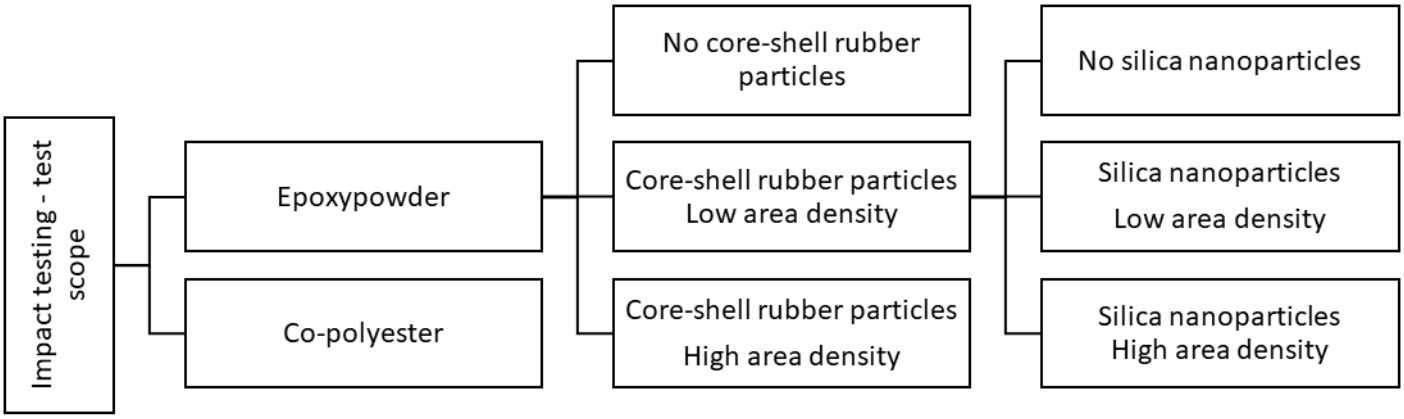

Figure 3.6: Tree diagram for the test scope - additives and binders

Most steps explained in the previous chapters for the sample preparation are identical for the impact sample preparation and are therefore not repeated here. The things added or changed, however, are mentioned. Table 3.1 relates the specimen number to the additives inside the specimen.

Table 3.1: Specimen number and corresponding material mixture

#	Binder	CSR (wt%)	SNP (wt%)	#	Binder	CSR (wt%)	SNP (wt%)
1	Epoxy	0	0	10	Co-polyester	0	0
2	Epoxy	0	10	11	Co-polyester	0	10
3	Epoxy	0	20	12	Co-polyester	0	20
4	Epoxy	6	0	13	Co-polyester	6	0
5	Epoxy	6	10	14	Co-polyester	6	10
6	Epoxy	6	20	15	Co-polyester	6	20
7	Epoxy	15	0	16	Co-polyester	15	0
8	Epoxy	15	10	17	Co-polyester	15	10

3.3.1 Epoxy binder

Cut plies were processed further by applying binder materials to one side of the plies. The epoxy binder's supplied form is a powder with high reactivity. The powder like form is due the base resin, which is a solid bisphenol-A epoxy resin. The powder has been applied manually at room temperature with a woven sieve. A good area density for preforming and binder purposes is between 10 – 15 g/m² according to the supplier. For that, the weight of each ply has been measured beforehand. Then, the binder has been applied evenly on one side of the ply and was then placed in an oven for three minutes at 80 °C. This offered sufficient time for the epoxy binder to melt and adhere to the carbon fibre plies. After, the plies have been set aside to cool down, so that the epoxy binder solidifies. The weight of the plies with epoxy binder has then been documented

again and the area density was calculated. The achieved area density was 12.94 g/m² on average with a standard deviation of 2.64 g/m² for +-45 plies and 0/90 plies combined.

Figure 3.7: Setup for applying epoxy binder onto the dry NCF plies

Figure 3.7 shows the setup of how the epoxy binder has been applied to the dry NCF plies. In the bottom left of the picture is the scale, which in combination with a foil pan and some weights in it were used to determine the weight of the NCF plies before and after adding epoxy binder to them. The foil pan in the middle left of the image shows the sieve which was used to apply the epoxy powder evenly. Three plies were put into the oven at once, which can also be seen in the bottom right of the picture, where three plies with distributed epoxy binder are shown. The top right shows the stack of plies to be covered with epoxy binder. The following images (Figure 3.8 and Figure 3.9) show how the epoxy binder melts during the three-minute phase in the oven and then adheres to the NCF ply. The duration of three minutes has been identified by trial and error. The temperature of the oven has been chosen as suggested by the manufacturer.

Figure 3.8: NCF plies in oven at the beginning of the 3-minute melting process (epoxy binder is still solid and whitish)

Figure 3.9: NCF plies in oven at the end of the 3-minute melting process (epoxy binder is molten and transparent)

3.3.2 Co-polyester binder

Similar to the further processed plies with epoxy binder, the same has been performed with an elastomeric co-polyester. However, instead of being in a powder form, this material was provided as pellets. To apply the material to the NCF plies, a setup has been used that allows for applying the material as a hot-melt (see Figure 3.10). From a heated tank, in which the polymer pellets are added, the molten material is pushed through a heated tube with a pump. The extrusion die is heated as well and has multiple outlets arranged in a line. Connected to a linear axis powered by a DC servo motor, the molten polymer is applied in lines with a width of approximately 25 mm. After each line of binder material applied, the plies are moved manually by 20 mm to allow for some slight overlap. This overlap avoids any dry spots, as most of the material is located in the middle of the line applied to the ply.

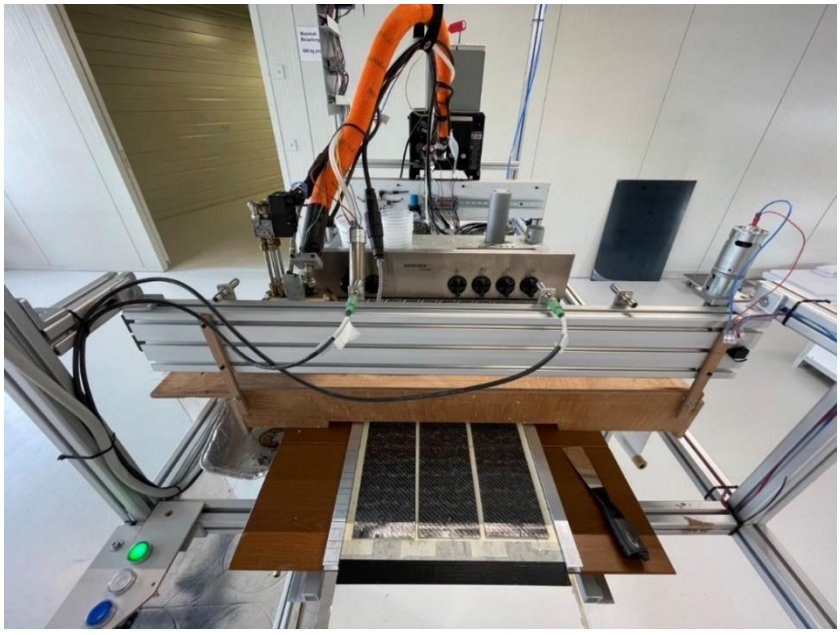

Figure 3.10: Hotmelt-Setup

To ensure a more even distribution of the polymer on the plies, compressed air is added to further distribute the melted polymer, which is extruded from the nozzle. The air can also be heated to various temperatures to avoid cooling the polymer during the time of leaving the nozzle and impinging on the NCF plies.
According to literature a value of about 3 wt% with respect to the resin weight in the specimen is good amount to allow for solvate the polyester in the epoxy resin while still allowing for good preforming abilities [57]. The 3 wt% can be translated to an area density by considering the number of plies in the specimen, the overall volume of the specimen and the fibre volume fraction. Based on that an approximate area density of 5-7 g/m² was defined.

3.3.3 Layup

After cutting the plies and applying binder material to them, preforming was done. For each impact specimen, eleven NCF-plies and one plain weave ply were put together. The NCF layup is shown in equation 4.1. Furthermore, a carbon fibre plain weave ply is added. Not included in the preform, but added as a dry ply, a glass plain weave layer is added on top of the carbon fibre plain weave. Furthermore, impact damage is expected to occur in between the NCF plies.

$$[0/90, (\pm 45, (0/90))_5] \tag{4.1}$$

The side with the binder material faces inwards, so that no binder adheres to the mould's surface. Furthermore, as the binder material faces inwards, the middle ply being oriented in ± 45-direction is without any binder on it, as both adjacent plies are faced towards it with the binder material on it. This has been done for all specimens. To resemble the preforming process, which – due to the geometry of the specimens – is rather simple, the plies were consolidated in the closed mould above their melting temperature and immediately cooled down after. For the epoxy resin this temperature is 80 °C and was then left to cool to about 50 to 60 °C before the preform was demoulded. Due to a large melting range of the co-polyester, the temperature was slightly higher at about 90°C and was cooled down to 40 °C before it was demoulded. Usually, each ply is heated and then patched onto the continuously growing preform, but in this case, the preforming and consolidation step was combined in the RTM mould.
Using the co-polyester binder material or the epoxy binder has significant differences on the preforming process, but also on the preform quality. For the co-polyester, the time window to handle the ply to be patched is larger, as the melting range is bigger, and the overall tackiness is higher. However, the epoxy binder offers high stiffness and maintains the shape of the preform (see Figure 3.11), whereas the co-polyester's elastomeric component causes the preform to be more elastic. The image shows that it maintains its shape and does not bend downwards, which shows the high stiffness of a preform made with epoxy binder. Figure 3.12 shows a side view of the co-polyester variant. This has a significant influence on the preforming process,

especially when it comes to patching complex shapes and should therefore be considered as well alongside the other results.

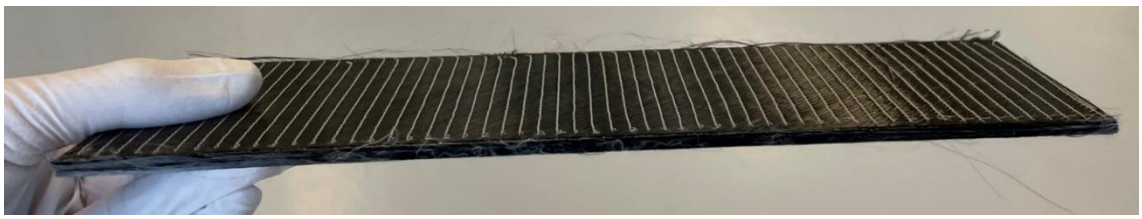

Figure 3.11: Side view of a consolidated preform with epoxy binder

Figure 3.12: Side view of a consolidated preform with co-polyester binder

3.3.4 Resin transfer moulding

The process is identical to the RTM process for the peel test specimens. However, as for some samples additives are included, the viscosity increases. In this case, the resin was mixed at 500 rpm for three minutes with the additives before the hardener was added and 2 minutes after the hardener was added. Identical to the peel test specimens, a dissolver mixer was used. With increasing viscosity of the resin system, the amount of entrapped air inside the pressure tank prior to the injection increased as well.

After all parts were manufactured, they have been waterjet cut to their smaller actual specimen size. Waterjet cutting was chosen to achieve high precision, but more importantly to avoid any influences on the matrix due to heat by either laser cutting, or friction induced during milling. The six specimens of size 40x80 mm² were declared as shown in Figure 3.13.

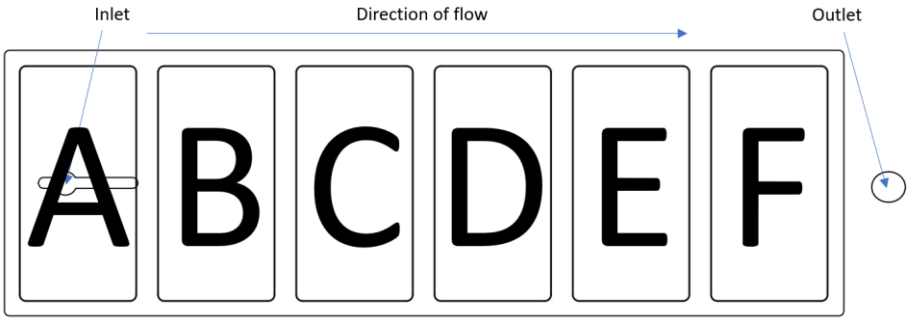

Figure 3.13: Mould cavity highlighting inlet, direction of flow, outlet and specimen declaration

3.4 Interface toughening

The goal of this test is to evaluate, how different interface materials have an influence on the force required to peel off a flexible adherend of a rigid adherend. In this case, the steel sheet positioned in the front is the flexible adherend and the CFRP-body is the rigid adherend. The other materials used are two different aramid veils with a different area density of 14 g/m² and 26 g/m². Both aramid veils have an individual fibre length of 12 mm. This is based on the literature review and then adapted due to availability at the supplier. In addition to that, the use of no interface material is included as well. The test scope is shown in Figure 3.14. The glass fibre weave is added in a dry, non-bindered state right before injection. That means that the preform is patched and consolidated with a binder material in-between, whereas the glass weave is positioned in a dry state in between the steel and the CFRP-preform. This was done identically for both the glass weave and aramid veils.

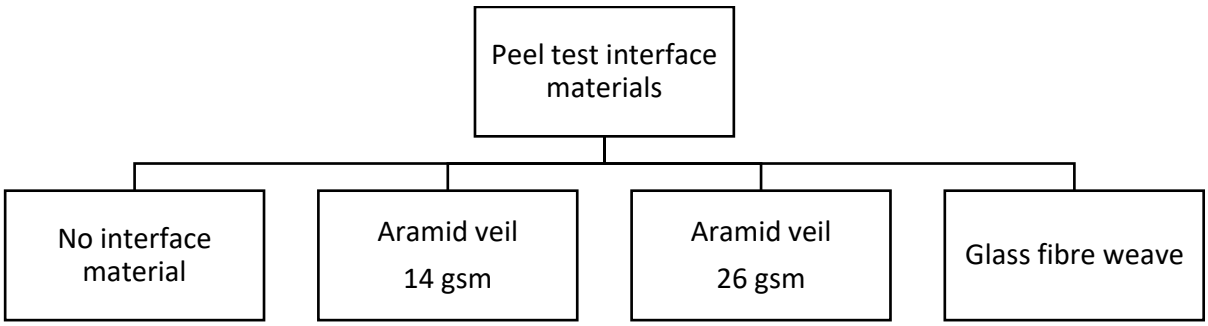

Figure 3.14: Test scope - interface materials

3.4.1 Layup

Due to the simple geometry the dry plies were positioned in the mould's cavity with high precision. To ensure comparable compaction values throughout the entire testing series for the peel tests, the fibre volume fraction

of the NCF portion of the hybrid structure was kept identical at 41.5 %. The resulting layups are shown in Figure 3.15.

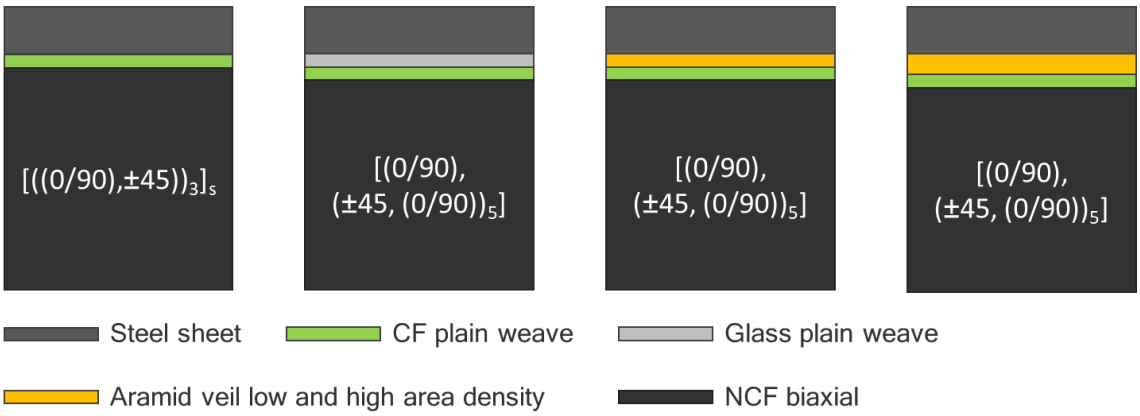

Figure 3.15: Layups for all peel test specimens

3.4.2 Resin transfer moulding

Additionally, to the standard manufacturing process explained before, the interface material was added according to the test scope for the peel specimens on top of the non-crimp fabric (see Figure 3.16). Then, the prepared steel sheet was added to the stack. The manufactured part was then waterjet cut into three specimens with the dimensions of 270x20 mm² of which 220 mm in length are usable for peeling.

Figure 3.16: Added materials on top of the NCF preform (top: aramid veil - bottom: glass fibre plain weave)

4 Methods

In this chapter the methods to perform and analyse both the matrix toughening and interface toughening are described. First, the impact experiment for the matrix toughening is explained, which is followed by the peel test setup for the interface toughening. Furthermore, the performed injection process analysis is described. Then, the methodologies for the used ultrasonic testing setup, the microscopes and differential scanning calorimetry are explained.

4.1 Impact testing

The impact testing series was done with a ball cannon available at *adultimum ag*, for which an impact fixture was developed to test the impact performance of the specimens manufactured. This chapter also explains the methodology for the impact test evaluation.

4.1.1 Ball cannon and impact fixture development

A ball cannon including high speed cameras is available. The setup allows for different mounting apparatuses to be installed. Depending on the air pressure applied the impactor speed varies.

4.1.1.1 Given base setup

To perform impact testing, a ball cannon is used. The ball cannon setup is shown in Figure 4.1. The ball is inserted into a launching tube made of steel. Inside the steel tube is a guide carriage made from carbon fibre reinforced plastics. It is made from CFRP to reduce the weight that needs to be decelerated and hence allows for reducing the braking distance. A combination of a foam like bumper and an air pad created when reaching the foam like bumper with the guide carriage allows for braking distances below five centimetres.
The ball is pushed into the tube with the guide carriage being pushed all the way to the end stop. Right behind that is a pressure tank which is controllable with a valve to be able to release the compressed air towards the guide carriage. Opening the valve forces the guide carriage to be pushed towards the exit of the launching tube causing the ball to accelerate with the same speed. At the foam like bumper the carriage decelerates causing the ball to be ejected into the impact area.

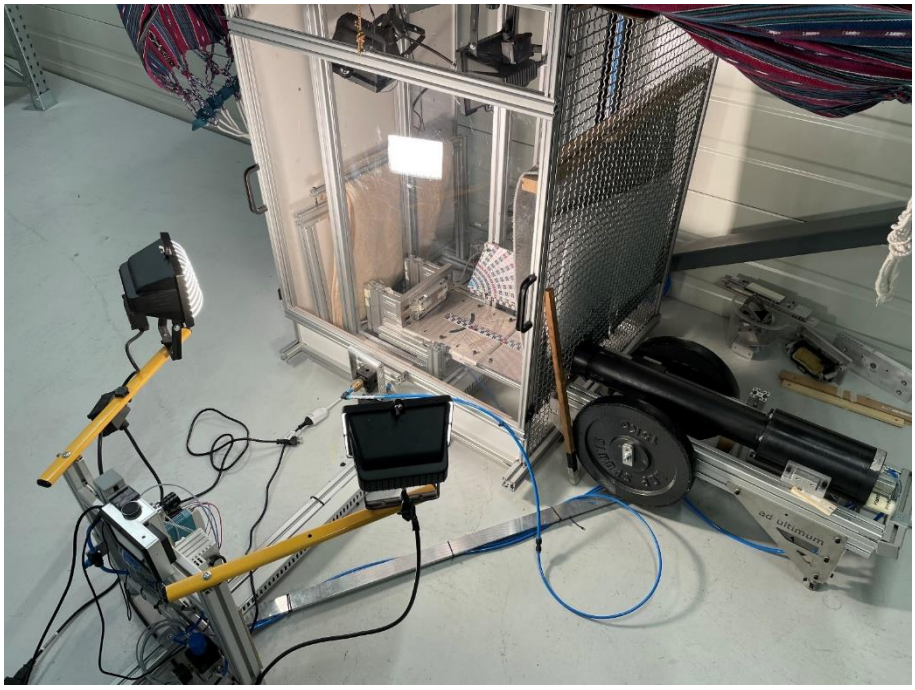

Figure 4.1: Ball cannon

This impact area of the ball cannon is surrounded by steel mesh and in the front by a clear polycarbonate panel. Furthermore, dampers made from different materials surround the impact zone to decelerate the ball after it rebounds from the specimen surface. By varying the pressure in the pressure tank, the ball's speed can be adjusted. To measure the speed, a scale has been installed in the impact zone. This scale in combination with a high speed camera is used to measure the time needed to cover a measured distance. The high speed camera is able to take videos with up to 3600 frames per second. Multiple spotlights ensure constant lighting conditions for the high speed camera.
A separate software is used to control the pressure in the pressure tank. Safety is ensured by checking if the front polycarbonate panel is closed before triggering the shot. The moment the shot is triggered, the high speed camera starts recording.

4.1.1.2 Considerations

The impactor speed used was defined as 146 kilometre per hour, which translates to 40.55 metres per second. To achieve this speed, the pressure used has been experimentally identified as 3 bar.

4.1.1.3 Final design

The impact fixture used for the specimens for this project were designed with the main goal being the shape of the specimens. The designed impact fixture consists of three mandatory components and one optional component. A CAD image is shown in Figure 4.2.

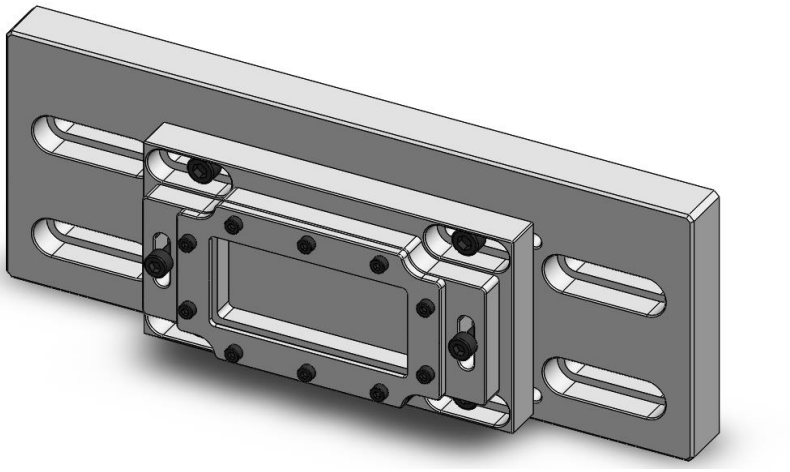

Figure 4.2: CAD drawing of the used impact fixture

The largest component at the back is used to do an initial calibration and positioning, which is why the oblong holes have been included in that component. This way the horizontal position can be adjusted, so that the ball hits the middle of the fixture. The second component from the back is used for horizontal adjustments in 5 mm steps. For that, guide pins have been attached to this component, which can be positioned in drilled holes in the back plate. This can be seen in Figure 4.3. The third component from the back is to adjust the position in the vertical direction. Again, oblong holes allow for stepless adjustment.

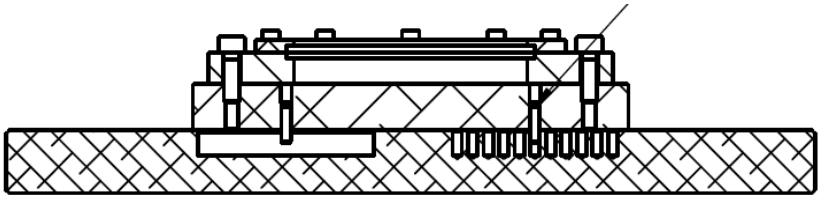

Figure 4.3: Cross section of the assembly drawing of the impact fixture

The fourth component is a frame that can be placed on the top. This component can be used to fully clamp the specimen in the impact fixture. This has an influence on the boundary condition. Hence, depending on the boundary condition to be tested, the top component can either be included or not. If the top frame to clamp the specimen is not used, it is comparable to a simply supported situation, as the edges of the specimens are free to rotate. Figure 4.4 shows the impact fixture installed in the ball cannon setup. The impact fixture allows for specimens with different thicknesses to be tested. The dimensions of the specimens fitting inside the fixture are 80 mm in width and 40 mm in height.

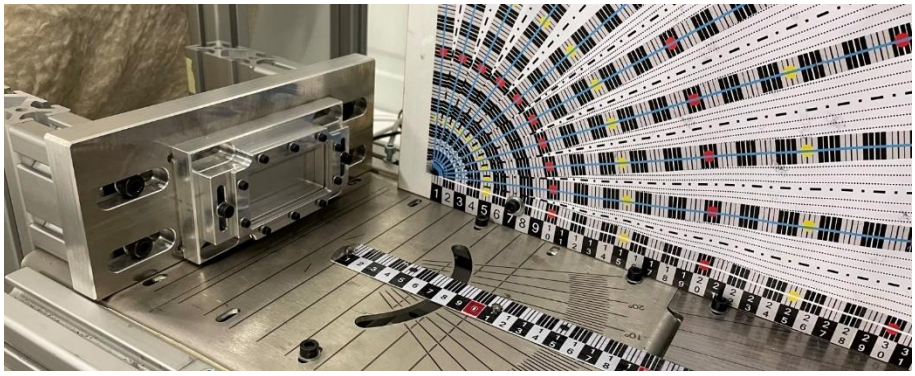

Figure 4.4: Close-up photo of the impact fixture installed in the ball cannon setup

4.1.2 Impact test methodology

During impact testing the adjusted pressure of the ball cannon accelerated the ball to a speed of 40.84 m/s (147,02 km/h) with a standard deviation of 0.115 m/s based on all shots performed, which translates to 37.5 J. The impactor speed was identified with a high speed camera capable of capturing 3600 frames per second. With a scale in the back the distance travelled was measured. The footage of the high speed camera has been saved for the first, fifth and tenth shot, depending on how many shots were planned for that specimen. If the specimen's delamination reached the edges, the testing series was stopped for that specimen and the footage was saved, too. For each additive and binder combination, the number of impacts varied from 1, 5, 10 to 20 impacts per specimen. However, due to early failure for most specimens, the range was reduced to one impact, five impacts, ten impacts and then stopped, whenever a specimen failed after ten impacts. In most cases, the lowest number of impacts was always done with specimen A and increased from there. That means that specimen A was designated for single impact testing, specimen B for five impacts, specimen C for 10 impacts and so forth. Depending on specimen quality the order can change or move.

4.1.3 Impact test evaluation

Similar to calculating the impactor speed before hitting the specimens, the same was done after the impact to be able to identify the change in speed and therefore energy loss. Figure 4.5 shows an image captured by the high speed camera showing the used scale in the back and the moment of impact.

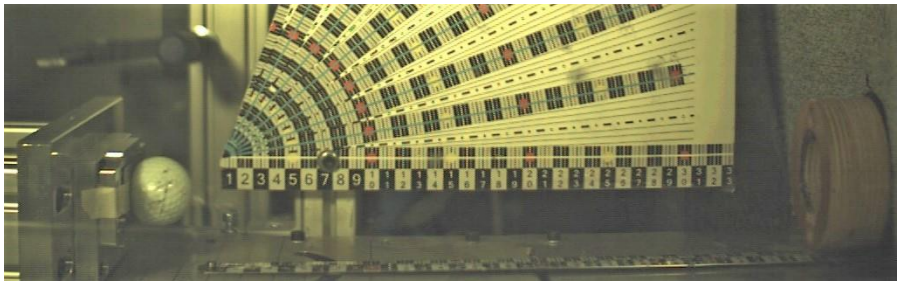

Figure 4.5: Image captured by the used high speed camera

4.2 Peel testing

In this chapter the peel testing setup including the motivation for the mandrel peel test setup is described. Furthermore, the method on how to analyse the results is explained.

4.2.1 Mandrel peel test setup development

The following chapter explains the motivation for choosing the mandrel test, which is then followed by a chapter highlighting the considerations that went into the design of the peel test setup. Along that the final design of the mandrel peel test setup is presented.

4.2.1.1 Motivation

For the interface toughening analysis various tests were considered. Given the universal testing machine environment at *adultimum ag*, a setup fitting into this environment without major modifications was one of the main objectives. Furthermore, the peel forces obtained should be easily comparable and represent a scenario as close as a peel test can get to the real circumstances of a steel-CFRP structure exposed to out-of-plane impacts. Different peel tests were presented in a previous chapter and each of them have benefits and drawbacks. A benefit for this mandrel peel test is a very defined and guided peel process, which is supported by the counterweight forcing the flexible adherend that is being peeled off to conform to the mandrel. This yields constant peel angles and in the case of non-conformity of the adherend to the mandrel adjustments can be performed without having to remodify the entire setup. This can either be achieved by increasing the counterweight or by varying the mandrel diameter. Even though the setup is more sophisticated than a standard floating roller peel test or T-peel test for example, it offers more flexibility and more precise results. This can be different for other adherends being peeled, but for this scenario the mandrel peel test is chosen as the most suitable setup.
When designing the mandrel peel test setup, it is the goal to keep the friction of the system as low as possible, so that the force applied is used for peeling of the flexible adherend, which is in this case a 0.5 mm thick steel sheet.

4.2.1.2 Considerations and final design

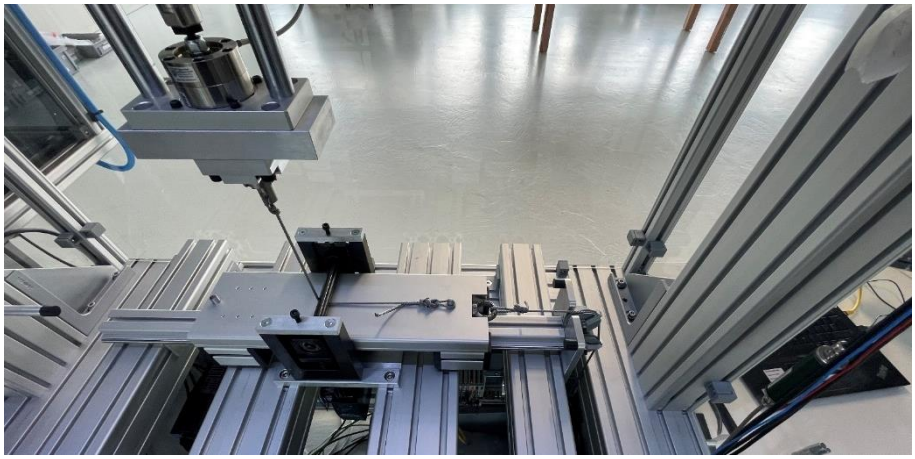

Figure 4.6: Developed mandrel peel test setup

The developed setup is shown in Figure 4.6. For that a slide unit from manufacturer *item* is chosen that is mounted on a linear slide. At the back of the slide unit, a ring nut is used to connect the rope with the counterweight. Two cylindrical pins are positioned inside the slide unit. One at the front side and one at the back side close to the ring nut. To ensure a press fit, the holes drilled into the slide unit are slightly smaller in diameter than the cylindrical pins. By heating the slide unit to 200 °C and freezing the pins to -30 °C, the assembly was possible without any additional force. Letting both components reach room temperature, the pin is hold in position due to the press fit.

Depending on the specimen configuration, either pin can be used to induce the force of the counterweight into the specimen (see Figure 4.7). Either a hole drilled into the end of the specimen with the same diameter as the pin would allow for attaching the specimen to the back pin close to the ring nut to induce the counterweight force equally both into the flexible and rigid adherend. Alternatively, without a hole in the specimen, the rigid adherend can be positioned with its edge to the front pin, introducing shearing forces into the interface. However, due to a peeling distance of more than 200 mm the force induced by the counterweight has a marginal impact on the mode I/mode II distribution.

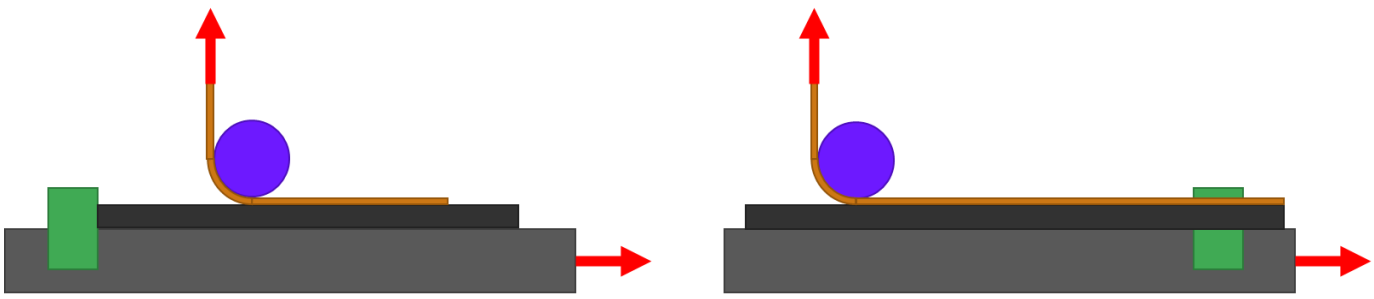

Figure 4.7: Schematic of the different mounting options available - left: rigid adherend being pushed forcing the flexible adherend to be pushed around the mandrel - right: both adherends being pulled causing flexible adherend to conform to the mandrel

The mandrel and the deflection pulleys for the rope attached to the counterweight are ball bearing mounted to reduce friction even further. For the mandrel the ball bearings are included in flange bearings. The mandrel's diameter is 10 mm. According to the following formula, where the elongation at break and modulus define the radius of the mandrel, a diameter of 1 mm for the used stainless steel is required to make the flexible adherend conform to the mandrel [58]. The equation is shown below (see equation 3.1). R depicts the minimum mandrel radius. h is the thickness of the flexible adherend to be peeled off and ϵ is the elongation at break. The diameter has been chosen higher than that, so that also flexible carbon fibre peel arms can be peeled off, which have an elongation at break at around 1.7 to 1.8 % depending on the material used. Apart from that, a mandrel with a diameter of 1 mm is prone to bending when the peel forced is applied.

$$\mathrm{R} > \frac{\mathrm{h}}{2\epsilon} \tag{3.1}$$

To make the process more robust and stiffer, a diameter above that is chosen. This diameter is also suitable for most carbon fibres and therefore needs no replacement when peeling off other materials. However, changing the mandrel and therefore its diameter is possible without any problems. This is possible with the mounting of the mandrel, which allows for the height to be adjusted. This is also important for different specimen thicknesses, so that the mandrel can be placed just above the specimen to avoid any clamping and therefore induced friction.

Figure 4.8 shows the mandrel peel test setup with a specimen being peeled off. For all specimens the front cylindrical pin is used. It shows that the force of the counterweight is pushing against the rigid adherend forcing the flexible adherend to conform around the mandrel. The weight and therefore force of the counterweight to find a good conformity of the flexible adherend around the mandrel has been identified with trial and error. A force of 50 N or approximately 5 kg were identified as ideal. Each peel test is video captured.

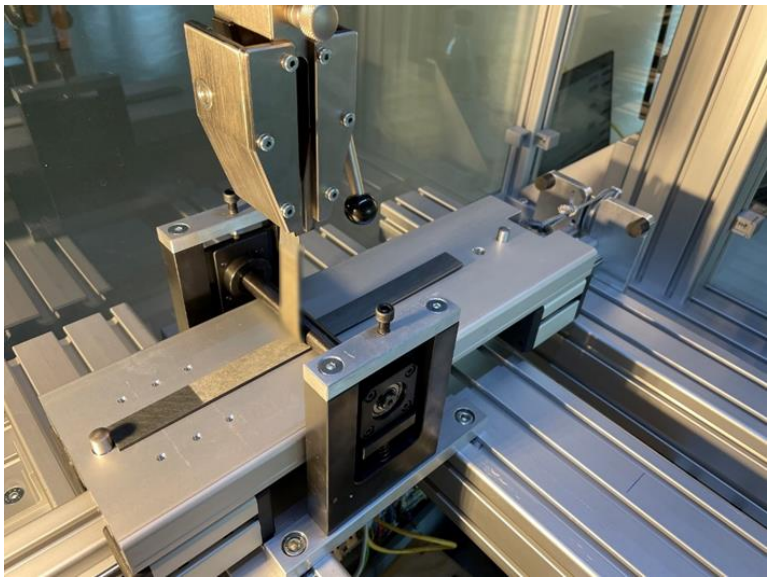

Figure 4.8: Specimen peeled off halfway in the mandrel peel test setup – partially blurred

4.2.2 Peel test methodology and evaluation

To compare the specimens without any friction and other influences, the true peel force was determined. This means that the initial force-time diagram values were put in relation to a second peel test performed, where the flexible adherend was no longer bonded to the rigid adherend. This was done to reduce the error due to force required to bend the specimen elastically and plastically, but also due to friction, which can be reduced to a minimum, but not avoided entirely. Those two values were then subtracted from each other.

4.3 Injection process analysis

Furthermore, for every RTM cycle performed the time between resin entering the mould and reaching the outlet was measured. These injections times are related to things such as binder type, additive concentration or viscosity. The dynamic viscosities of the resin mixtures are estimated based on the Refutas model [59, p. 379]. For that, the individual viscosities at injection temperature and weight fractions of the component in the mixture are considered. This includes the resin, hardener, silica nanoparticles and core-shell rubber particles. In a first step, the viscosity blending index is determined for each component with the following equation (see equation 4.1).

$$VBI = 10.975 + 14.535 * \ln(ln(\nu + 0.8)) \tag{4.1}$$

VBI stands for viscosity blend index and is calculated based on the kinematic viscosity ν of the individual component at a given temperature, which is 60 °C in this case. The kinematic viscosity is obtained by relating the dynamic viscosity to the density of the medium (see equation 4.2).

$$\nu = \frac{\mu}{\rho} \tag{4.2}$$

The viscosity blend index is calculated for every component of the system. For the blend, which is a mix of the resin and different additive contents, the VBI is multiplied by the respective weight fraction to obtain a VBI for the resin blend. To then obtain the viscosity of the resin blend, equation 4.1 is solved for the kinematic viscosity, yielding the following (see equation 4.3).

$$\nu = \exp\left(exp\left(\frac{VBI - 10.975}{14.535}\right)\right) - 0.8 \tag{4.3}$$

To obtain dynamic viscosity, equation 4.2 is solved for dynamic viscosity and the kinematic viscosity obtained from equation 4.3 is multiplied with the density from the resin blend.

4.4 Ultrasonic testing

After all impact specimens were shot at, they are further analysed using ultrasonic C-scan. Using a pitch-catch method through-transmission measurements are performed in a water tank. The specimens are submerged in the tank and positioned, so that they are centred between the sender and receiver. The measurement is done automatically with prior defining the start and end point. This allows for testing multiple specimens at once, accelerating the scanning. The data provided from the C-scan is interpolated with a Python script. The attenuation through water was close to zero and for a neat specimen around -9 dB to about -12 dB. Increasing attenuation and therefore a change in colour means a higher increase in damage, as the signal is dampened due to delaminated area and deformation of the specimen. To avoid water ingress during the C-scan measurement, the edges for the visibly delaminated specimens are sealed off with tape. The C-scan setup is shown in Figure 4.9.

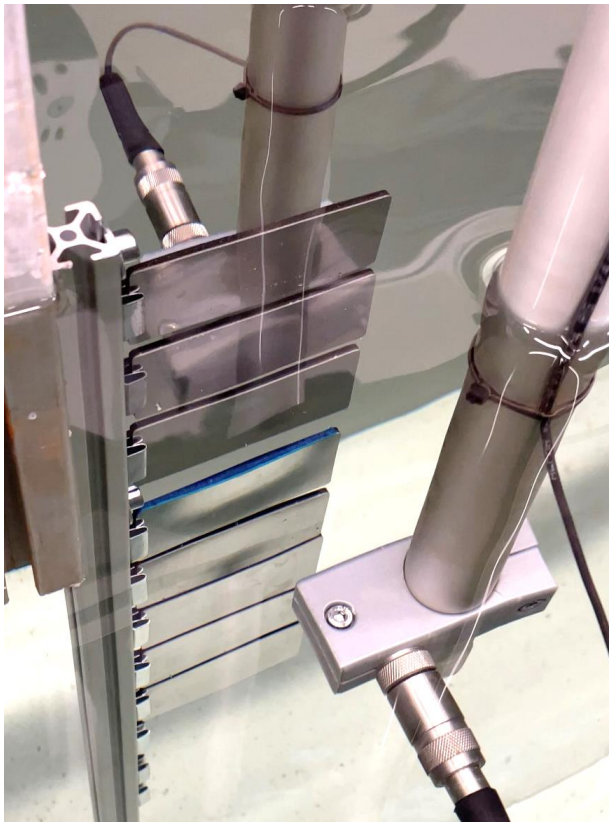

Figure 4.9: Impact specimens submerged in water during ultrasonic testing - blue tape is visible at the 4th specimen from the top

4.5 Microscopy

Also, the samples were scanned with a 3D-scanning microscope by *Keyence* to quantify the deformation of the specimens. Furthermore, smaller samples were cut from the centre of the specimens with a diamond disk saw to further analyse them with a high resolution laser confocal microscope and a scanning electron

microscope. Figure 4.10 shows how the samples were cut to prepare them for the higher resolution microscopes. The red zone in the drawing to the left highlights the impact zone.

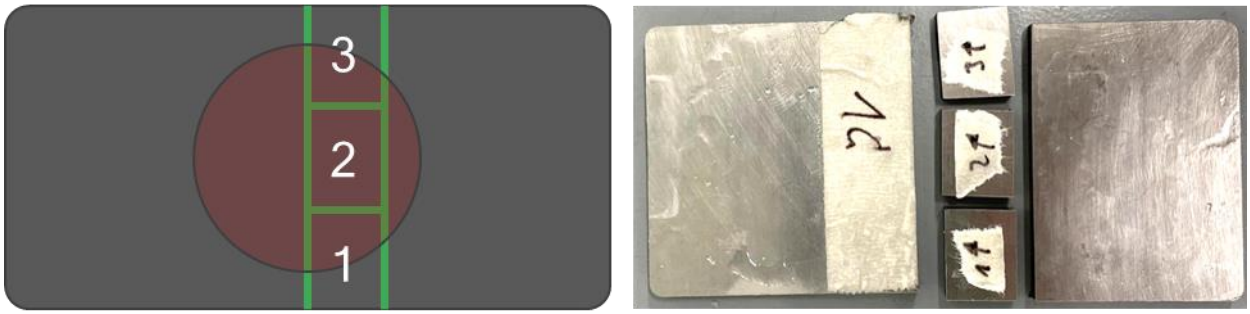

Figure 4.10: Sample cutting for microscopy (red highlights impact zone)

4.6 Differential scanning calorimetry

The resin samples from each additive combination were used to determine the glass transition temperatures using differential scanning calorimetry (DSC). Figure 4.11 shows the sample positions in the RTM mould, which is a cavity without any fibres in it and therefore yielding pure resin samples. One sample is located at the inlet, whereas the other one is located right next to the outlet of the mould. For the DSC measurements, two ramp heatings were done consecutively. Each ramp heating starts at 25 °C and increases with 10 °C per minute to 150 °C. A cooldown phase between the two runs is done with a decreasing temperature of 10 °C per minute. This way, the glass transition temperature after the curing cycle and after a tempering cycle can be compared. Furthermore, as two resin samples per additive and binder combination are given, additive filtering can be investigated by comparing the glass transition temperature values of both samples. Also, the influence of the binder is checked and compared.

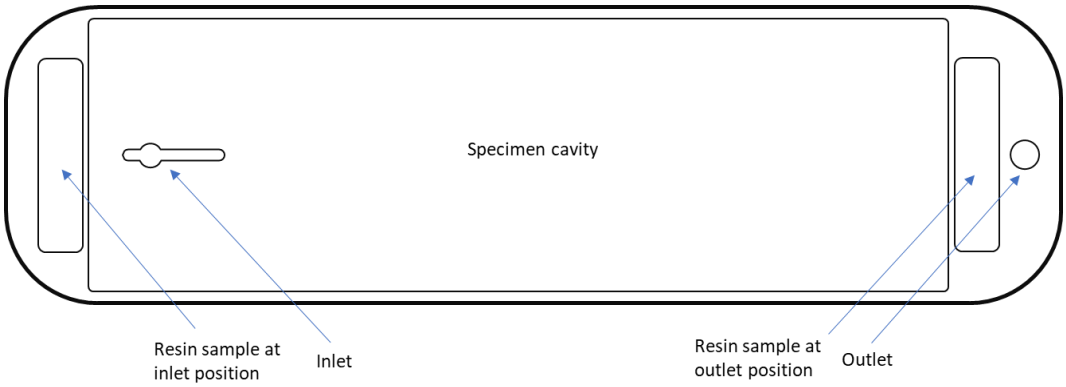

Figure 4.11: RTM mould incl. resin sample position

5 Results and discussion

The aim of the proposed project including the two individual experiments is to make steel-CFRP hybrid structures more damage tolerant. For this, different interface materials and additives to be incorporated into the matrix are considered. Both aspects were tested with different setups, where the interface toughening was analysed with a mandrel peel test setup and the matrix toughening was evaluated with impact testing and a series of different methods to analyse the impact tolerance. The results of the testing series to investigate the hypothesis, where an increasing additive content or different interface material should yield increasing impact performance or damage tolerance, is presented in this chapter. This includes the influences of the manufacturing aspects.

5.1 Interface toughening

One part of the project dealt with the peel testing of different interface material included in between the CFRP body and the steel sheet. For that, the mandrel peel test was used. In this chapter the results of the peel testing experiment are presented, which goes along with a discussion of those results.

5.1.1 Results and discussion

Figure 5.1 shows the true peel results. The peel force shown on the y-axis is in N/20 mm due to the specimen width of 20 mm. More common are specimen widths of 25 mm or 1 inch. However, due to the RTM mould's size a slight reduction in width was chosen. Before comparing the results, it is important to mention that the relative difference between the peel forces of the different interface materials is higher in reality, as the plastic deformation was not manually reverted after the first peel run. Therefore, a contribution of the additionally required force to plastically bend the flexible adherend in the first run, falsifies the results slightly. Nevertheless, the absolute comparison is as valid, only the relative difference between the individual specimens appears smaller than it actually is.

It can be seen that the specimens with glass weave in the interface perform the worst in comparison to the other three interface materials tested. The glass weave specimens reach about 80 N/20 mm on average. Interesting to see is the difference between the two aramid veils. Both veils consist of aramid fibres with the same length, the only difference is the area density being 14 g/m² and 26 g/m² for Aramid14 and Aramid26, respectively. An increased content of short aramid fibres did not yield an increase in peel strength, but rather resulted in a more constant performance. Fibre bridging of a specimen with a 14 gsm aramid veil as an interface material is shown in Figure 5.2. The time given in the description indicates from where in the video the photo was taken from.

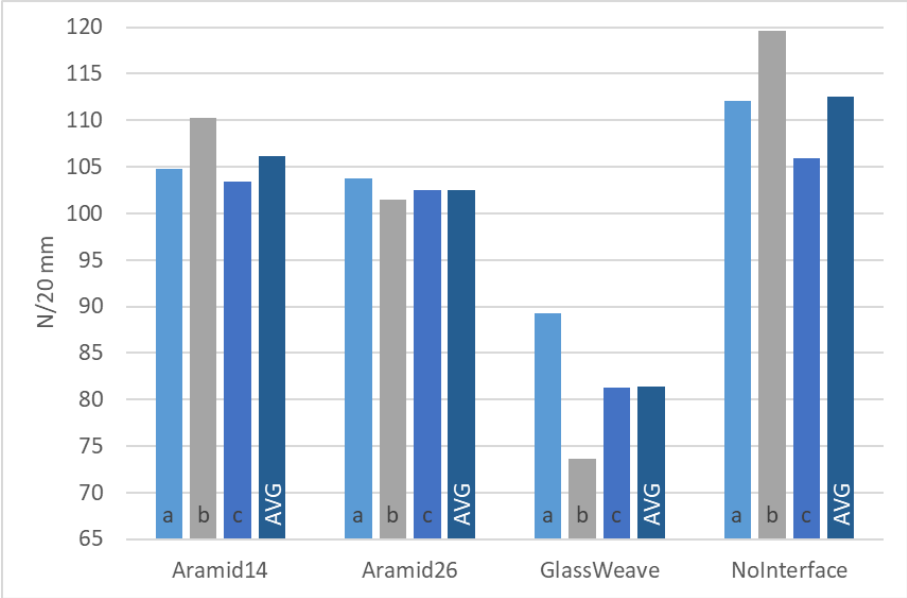

Figure 5.1: Peel testing results

The fibre bridging shows that the short aramid fibres adhere to both the CFRP body and the steel surface causing an increase in peel load. At the left end of the yellow highlighted area also a chunk of resin is visible. Resin with embedded aramid fibres are mechanically interlocked to the steel surface. This holds the fibres in place until they either get pulled out of the surround matrix or fail under tension.

The specimens with no interface material included yielded the highest peel forces. Unlike the specimens with the additional interface material, the steel sheet was in closer contact to the consolidated preform for the specimens with no interface material. This is due to the higher degree of compaction of the NCF plies because of their non-woven structure. Therefore, the randomly oriented aramid fibre veils and the glass weave cause a lower fibre volume fraction in the interface area, contributing to a weaker bond due to an increased resin rich region.

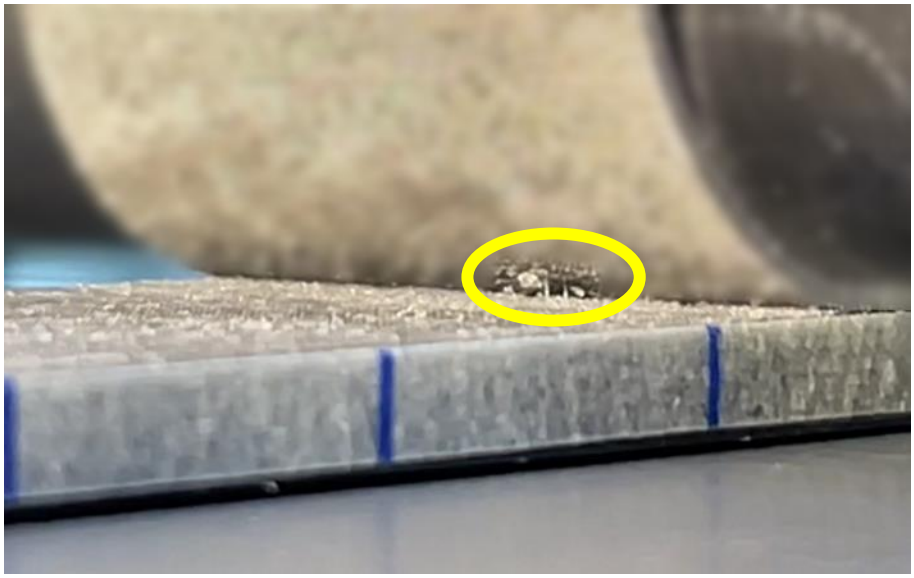

Figure 5.2: Fibre bridging (Aramid 14 gsm, specimen b, 3:29) – blue markings 10 mm apart – partially blurred

Figure 5.3 shows a specimen without interface material during the peel off test. The white fibres pointing upwards from the CFRP body are stitching yarns, which keep the bi-axial non-crimp fabric and their individual fibres in place. It is an elastic and weaker material in comparison to carbon fibre, suggesting that the stitching yarn is not contributing to an increase in peel force. However, the yellow highlighted zone shows bundles of carbon fibres bridging between the flexible steel adherend and rigid CFRP adherend. This paired with the bundles on the surface in and around the yellow area show that the bond between fibres, matrix and steel sheet is strong enough to break individual carbon fibres and tear them upwards while peeling. The image shows that the fibres are oriented 90 degrees turned towards the peeling direction. Having the fibres rotated by 90° resulting in a 0°-orientation and cause them to be parallel to the peeling direction, further improvements can happen. The fibres are embedded in resin over a larger distance resulting in higher forces necessary to tear the fibres out of the matrix and pull them upwards with the steel sheet that is being peeled off.

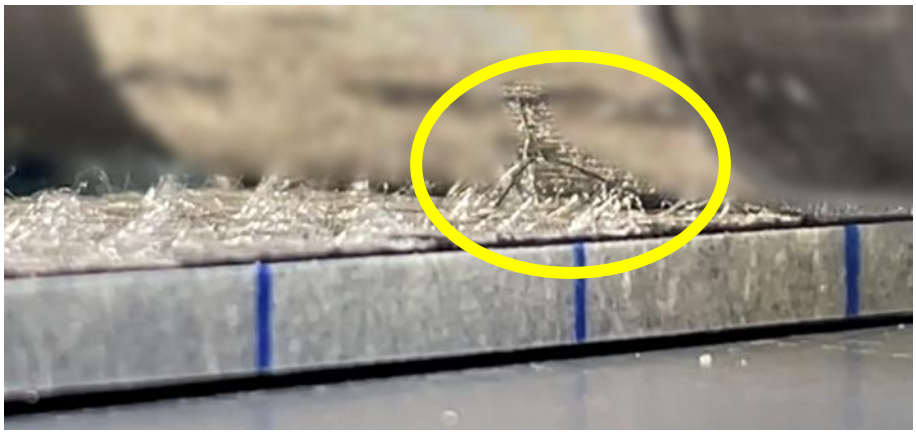

Figure 5.3: Fibre-bridging (no interface, specimen a, 4:31) – blue markings 10 mm apart – partially blurred

Impregnation for the version with additional interface materials was not hindered and validated with microscopy. However, as initially hypothesised, the glass weave did not mechanically interlock with surface of the steel sheet, supporting the weaker performance, as the interface is only matrix based. Right underneath the steel the glass weave is visible, which does not interlock with the steel. As this shows an impact specimen, right under the glass weave is also a carbon fibre plain weave. In fact, the glass weave-matrix bond was the weakest in the entire interface, as after peeling the aforementioned resin-rich region caused by the glass weave and aramid veil adhered to the steel sheet. So, the resin between the steel sheet and the glass weave debonded from the glass weave and adhered to the steel sheet. This can have various reasons. The glass weave sizing might not be ideal, or simply the bond of steel sheet to resin outperforms the interface of glass weave to resin. To fully understand why this happened, further analysis is necessary. However, it shows that the glass weave acted as a boundary layer regardless.

Apart from the performance results, the incorporation into the automated manufacturing process in regard to economic feasibility needs to be considered as well. One material may be the best performing material available, but if including this material into the automated production is not possible, it is not going to be tested. Therefore, a short analysis of where and how the individual interface materials will be incorporated

into the production process is performed. By doing that, it can be evaluated, if the material can also be economically incorporated into the serial production later.
Both aramid veils need to be cut to the right shape and then automatically positioned on the preform in a similar fashion as it is the case for the carbon dry fibre. To be able to hold the aramid veil in position, binder material might be necessary. This would cause no additional steps in the production process, as the binder is also needed for the dry fibres. Therefore, it can be incorporated without any extra effort. The same applies for the glass fibre weave, which needs to have a binder on it to be able to hold it in its position. Similar to the aramid veil, it is the same process, just with a different material.

5.1.2 Concluding remarks

The peel tests yielded insight into the influence on peel strength of different interface materials. The chosen test setup – namely a mandrel peel test – offers a simple test procedure in comparison end-notched flexure test for example. However, when analysing and interpreting the results, it needs to be considered that a peel test is a mixed mode loading condition, where mode I predominates. Also, the peel forces might differ, when the interface materials are included in the preforming and consolidation process. This most likely requires them to have binder material applied to them as well, offering better compaction and therefore higher fibre volume fractions. However, given the current process at *adultimum ag*, the results indicate and show that the forces required to peel off a steel sheet with the given specifications from a rigid CFRP adherend are the highest when no interface material is included and the ply adjacent to the steel sheet is made from biaxial non-crimp fabric. Also, the different coefficients of thermal expansion and material stiffnesses influence the peel strength.

5.2 Matrix toughening

This chapter presents the results of the impact testing experiment. Alongside the results presentation a discussion is done. The injection times and energy losses due to impact are presented, but also the results from the ultrasonic testing as images and quantified results are described. After presenting the results and insights gained from microscopy, all analyses and results are discussed summatively. This chapter also includes results from a DOE analysis highlighting significantly contributing factors.

5.2.1 Injection process

Three to five specimens out of the six specimens per additive combination manufactured showed no visual imperfection such as dry spots. Due to the mould’s design race tracking is inevitable and depending on the

resin mixture's viscosity dry spots varied in size. Due to the race tracking dry spots formed in and around specimen position E (see Figure 5.4).

Figure 5.4: Impact specimens after the RTM process - dry spots are visible at the right side of the part

The following graph (Figure 5.5) shows the relation of injection time to dynamic viscosity for all the impact specimens manufactured with co-polyester and epoxy binder. The y-axis shows the resin viscosities based on the Refutas model for the different additive combinations. The x-axis shows the time needed to infuse the preform. It can be seen that for all resin mixtures tested the infusion time was lower for the specimens manufactured with the co-polyester binder.

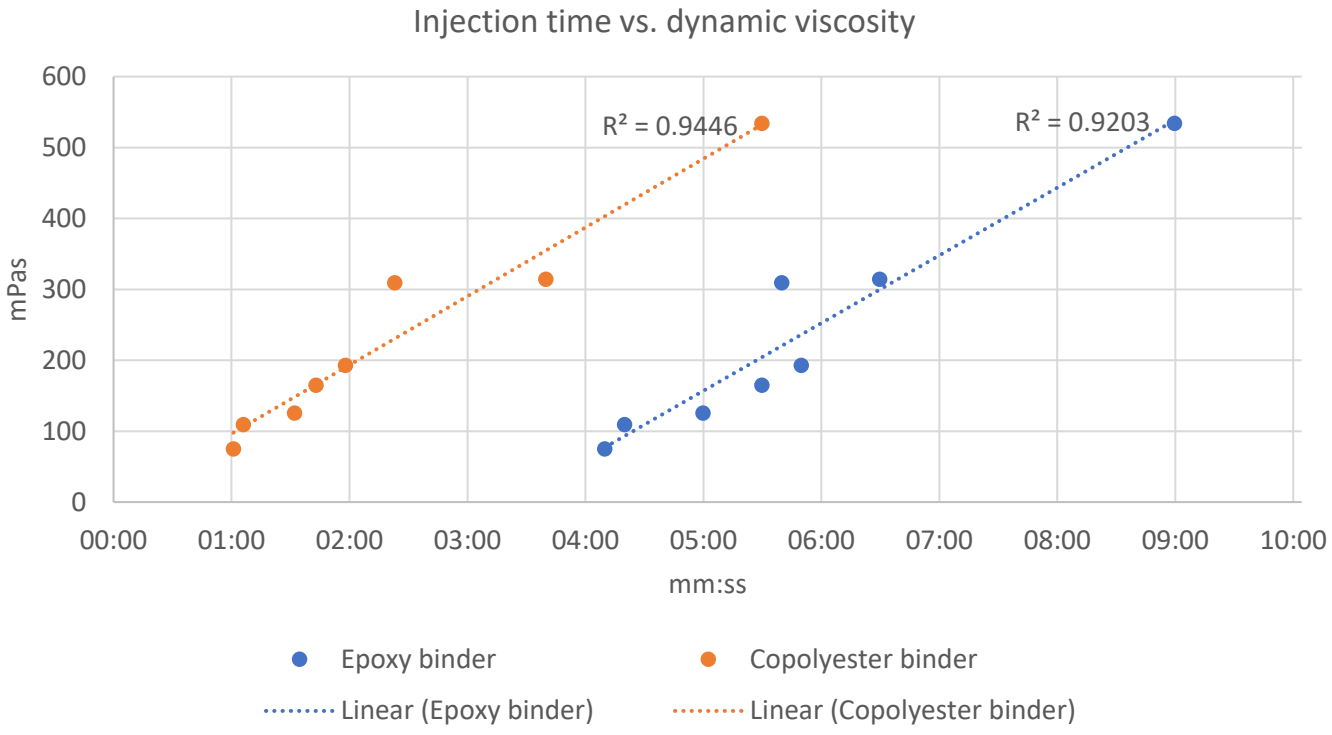

Figure 5.5: Injection time vs. dynamic viscosity

A linear trend can be assumed based on Darcy's law (see equation 6.1).

$$t = \frac{L^2 * \nu}{\Delta \mathrm{p} * \mathrm{k}} \tag{6.1}$$

t resembles the injection time needed to inject the dry fibre preform with resin. L is the part's length, which depends on the flow direction. The length from inlet to outlet defines the length to be used to calculate the injection time. ν is the kinematic viscosity of the medium flowing through the preform, whose permeability is defined by k. $\Delta \mathrm{p}$ describes the pressure difference between inlet and outlet.

It can be seen that an increasing pressure difference and permeability reduce the injection time, whereas increasing the injection length and viscosity increases the injection time. The injection length's influence is the biggest due to it being squared.

However, for this comparison the viscosities, the pressure difference and length are identical for all specimens, regardless of the binder material used. Therefore, the only influence is the permeability of the preform. Of course, variations can be caused by numerous things. The vacuum level and stability varies slightly during injection and throughout all specimens created. Furthermore, all preforms including applying the binder material was done manually, which has an influence on the permeability. Mixing viscosities are assumed based on the Refutas model, which does not resemble reality accurately, but is rather an approximation. Also, the included steel sheet hinders flow and can have varying gap sizes due to tolerances during manufacturing.

Clearly, the reduced area density of co-polyester applied in comparison to the epoxy binder specimens has an influence on the permeability. The difference is a factor of approximately two, where the epoxy binder's grammage on the plies is higher. In addition to that, the melting ranges differ, and the epoxy binder remains solid at injection temperature, unless it goes into solution right away. The co-polyester, however, is in its melting range at injection temperature and is therefore more likely to dissolve in the injected resin.

For automation and industrialisation these differences in injection time apart from the impact performance need to be considered. Longer injection times cause longer cycle times and need to either be compensated with longer working hours, more machinery or a shift in the balance of Darcy's law. That could mean to reduce the viscosity, which can be achieved by example increasing the injection temperature. Alternatively, the pressure difference can be increased, but that comes with modifications to the mould's closing and sealing mechanism, as it needs to be able to withstand higher pressures. Changing the inlet and outlet to reduce the length is difficult to accomplish in already machined and assembled RTM moulds.

5.2.2 Energy loss

With the footage from the high speed camera, which was used to track the speed before and after the impact, the energy loss was determined. The energy of the impactor was at a constant 37.5 J and was then compared to the remaining kinetic energy of the ball after impact. Figure 5.6 shows the mean energy loss grouped by binder type and number of impacts. A scale to the right shows the mean energy loss for that binder type and

number of impacts. White areas indicate that for this specific combination no data points are available. This comparison shows that the energy loss is in general higher for the co-polyester specimens and increases from one to five impacts. No co-polyester specimen was impacted more than five times due to visible delamination and therefore high damage. The epoxy binder specimens' energy loss is lower than for the co-polyester specimens, but never reaches values as high, even when impacting it 13 times, where visible delamination occurred as well. Interestingly to see are the energy losses for epoxy binder specimens with one or two impacts. The energy loss is higher than it is for specimens impacted four to ten times. This can be due to the sample position, as lower impact numbers were always used with the sample at the inlet of the RTM mould. The samples at the inlet showed imperfections due to fibre washing an due to the uneven surface of the inlet, as also highlighted by a photo in a previous chapter.

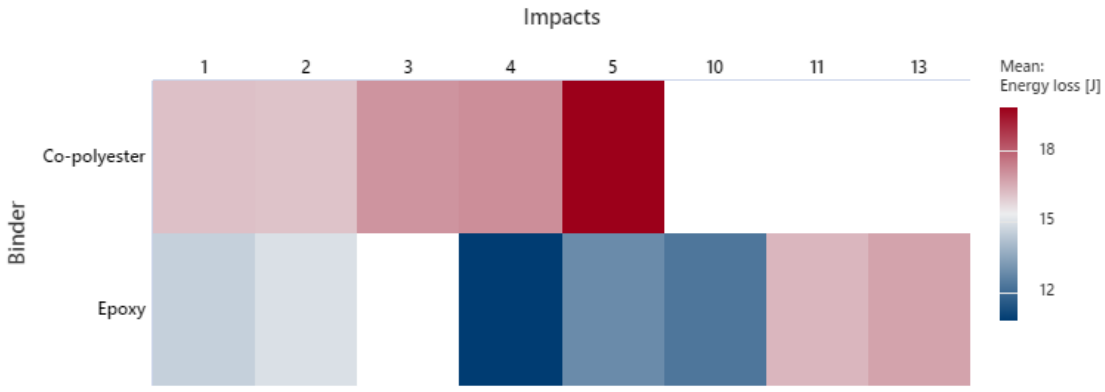

Figure 5.6: Mean energy loss grouped by binder type and number of impacts (Impact energy 37.5 J)

Figure 5.7 shows the energy loss due to impact for the specimens with epoxy binder and co-polyester. This only shows the shots performed without visual delamination. The energy loss is averaged for different numbers of impacts for the respective additive combination, as the change in energy loss before visual delamination occurred, is marginal. The diagrams for the energy losses after visible delamination can be found in the annex. The energy losses for those were higher in comparison to the ones without visual delamination at the sides in all cases. Considering the diagram shown on the left, it can be seen that the smallest energy loss occurred for the non-modified specimens. CSR0 SNP0 means 0 wt% of both core-shell rubber particles and silica nanoparticles. The increasing number behind either CSR or SNP describes the weight percentage of the additive used in the specimens. However, the error for each additive combination does not provide a clear trend. Nevertheless, the combination of 6 wt% and 20 wt% performs worse than both the CSR0 SNP0 and the CSR15 SNP10 variant, even when including the error.

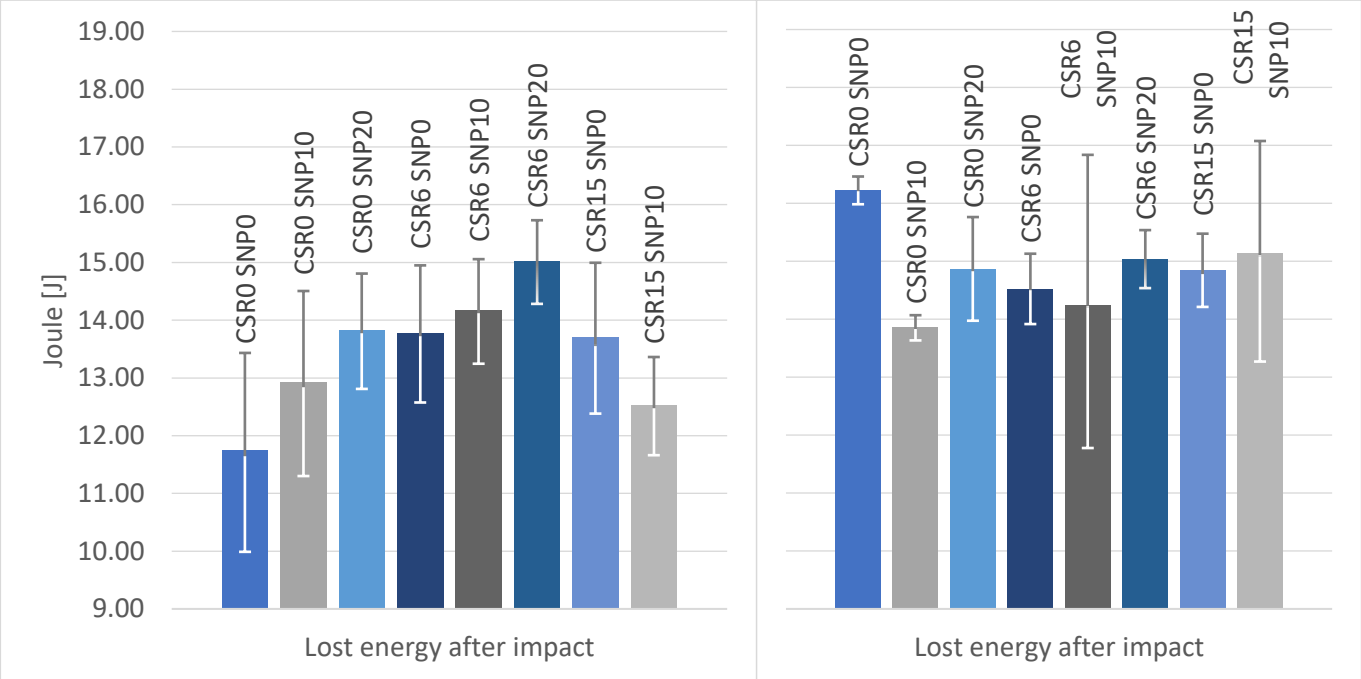

Figure 5.7: Energy losses for epoxy binder specimens (left) and co-polyester specimens (right)

The right diagram of Figure 5.7 shows the energy losses due to impact for the specimens manufactured with co-polyester binder. Due to large error and less data points available, no trend can be identified from this data. However, comparing this data to the epoxy binder specimens on the left, it becomes apparent that the energy losses for the co-polyester binder specimens are generally higher with the main exception being the epoxy binder specimen with 6 wt% of CSR and 10 wt% of SNP, which has also been highlighted in Figure 5.6. Furthermore, apart from comparing the energy losses for both binder types including all the additive combinations, the co-polyester specimens were less durable than the epoxy binder specimens. Most specimens with co-polyester, regardless of their additive content failed after one to three impacts with a few exceptions reaching four or five impacts without visual delamination at the sides. On the other hand, most epoxy specimens managed to withstand the impact energy and reached up to 13 impacts.

Based on a DoE-analysis (Design of Experiments) the main effects were analysed. Figure 5.8 shows a main effects plot for the epoxy binder specimens without the specimens at location A. Due to the fibre washing and irregular surface at the back the impact performance was worse with less impacts in most cases. Furthermore, considering the better performance of the epoxy binder, this has been looked at separately. The diagram shows the mean energy loss on the y-axis and this energy loss is related to three different variables and their values. The variables are the position of the RTM manufactured part, the viscosity of the resin during injection and the number of impacts. The viscosity of the system is dependent on the additive content.

Looking at the position in relation to the energy loss, it becomes apparent that the further away from the injection location, the higher is the mean energy loss. Comparing this to the large dry spots at position E of the RTM manufactured part, it supports the argument of worse filling behaviour with increasing distance from the inlet. This can be due to several factors. Race tracking is inevitable with this mould and could only be reduced to some extent. Furthermore, due to a low permeability injection is hindered and slowed to a point,

where the curing of the fast curing resin system slows the injection process even further. And, apart from that the air that was injected with the resin into the mould, is more likely to get compressed closer to the inlet, as the injection pressure has less difficulty compressing the mentioned air. However, it needs to be kept in mind that this graph does not consider that the number of impacts is higher with specimens further away from the inlet. Therefore, this curve is influenced by hidden effects, namely being the number of impacts.

Apart from some outliers a trend is identifiable, where increasing resin viscosity relates to an increase in energy loss during impact. Of course, this does not directly correlate, but a higher viscosity can have influences on several impact performance defining factors. Higher viscosities make the injection longer and more difficult in regard to compressing the medium. Longer injection times in combination with a fast curing system must be avoided, so that the injection process allows for perfect filling behaviour. If the filling behaviour is not ideal, voids weakening the structure can form.

The third variable in that diagram is the number of impacts. Similar to the viscosity graph, outliers are present. With an increasing number of impacts the mean energy loss increases. This allows to assume that an increasing number of impacts causes larger and more damage resulting in a higher energy consumption causing the energy loss to increase. To further support this argument, ultrasonic testing was done, and the results are described in the next chapter.

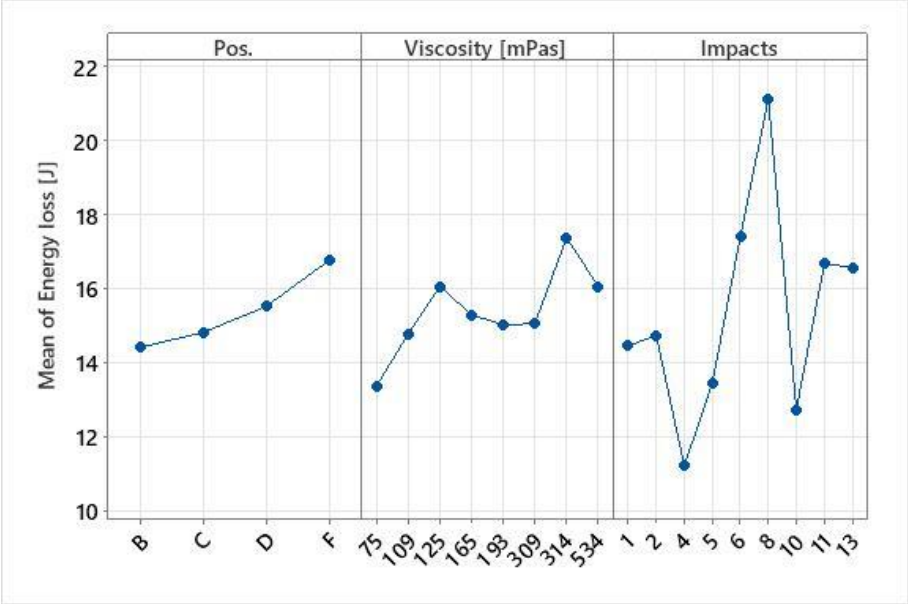

Figure 5.8: Main effects plot for epoxy binder specimens - excluded: position A

5.2.3 Ultrasonic testing

After all impact specimens were shot at, they were further analysed using ultrasonic C-scan. For convenience the drawing highlighting the specimen declaration and its position in the RTM manufactured part is shown in Figure 5.9 .

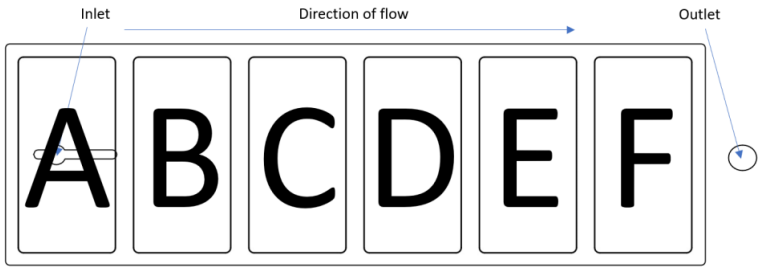

Figure 5.9: Mould cavity highlighting inlet, direction of flow, outlet and specimen declaration

Figure 5.10 shows the results from the C-scan measurements. The black area at the top of all specimens is due to the clip holding the specimens in place. The image shows the damage growth with an increasing number of impacts – especially for specimen B and C. Specimen A shows clear delamination in the centre of the specimen and an increased damage zone in shape of a line to the left. This damage occurs throughout all additive and binder combinations, which is due to the resin inlet of the mould. Fibre washing and not a perfectly even back surface allowed for damage to happen earlier than for specimens B to F. The C-scan images of the other specimens are shown in the annex. With an increasing number of impacts the damage inside the specimen reached the edge of the specimen causing visible delamination.

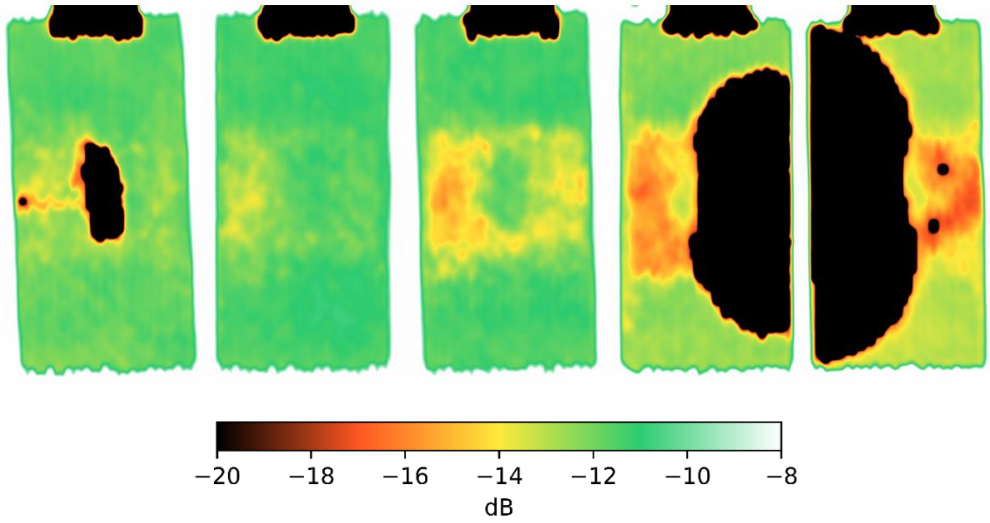

Figure 5.10: Specimens modified with epoxy binder and no additives - # of impacts from left to right: 1, 5, 10, 8, 11 - position from left to right: A, B, C, D, F

The specimens with co-polyester binder failed after one impact for the most cases, where a few exceptions reached between two and five impacts. The C-scan images show that the overall part quality was worse in comparison to the epoxy binder specimens, regardless of the additive content (see Figure 5.11). Unlike the epoxy binder specimens, the co-polyester specimens showed no trend of growing damage, but rather going from imperfect specimen quality to visibly delaminated specimens right away. The inconsistency in attenuation even for non-visibly delaminated specimens suggests that the co-polyester did not dissolve into

the epoxy resin and therefore having an influence on the propagation of the ultrasonic signal. Furthermore, the co-polyester can support void formation, which is further analysed in the microscopy chapter.

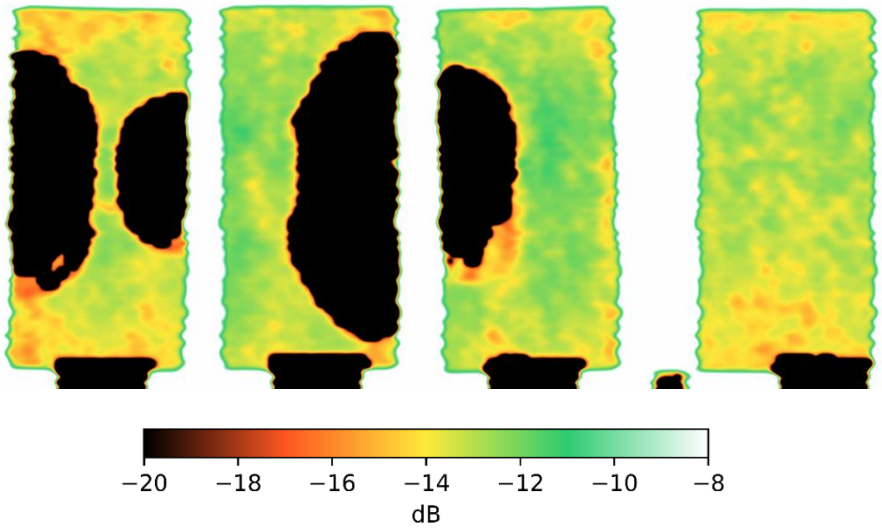

Figure 5.11: Specimens modified with co-polyester binder and 6 wt% CSR - # of impacts for all: 1 - position from left to right: A, B, C, D

To further understand the C-scan images, the raw data was run through another Python script, so that the visual representation of the damage growth is quantifiable. For that, the area with the clip holding the specimen has been cut off, so that it is not included in the counting process. Figure 5.12 shows the results for all epoxy binder specimens with 5 impacts. As the numbers of datapoints slightly vary due to the cut off of the area with the clip, the data points are compared relatively by setting one set of datapoints to 100 % individually. Green means almost no attenuation apart from the attenuation caused by the neat specimen. Yellow is considered damage initiation or slight damage, whereas red means multiple damage locations above each other or more severe damage. Black indicates full delamination or severe damage up to the point that it is visible from the outside.

The first thing becoming apparent is that the non-modified sample shows the least damage after five impacts, and it decreases gradually with increasing additive content with an exception being specimen 3B, which contains 20 wt% of silica nanoparticles and 0 wt% of core-shell rubber particles. However, looking at the C-scan images in the annex, one can see that the overall quality of the specimen group 3 is not as good as the other specimens. When looking at specimen 3B specifically, the surrounding area away from the impactor site show a larger area of attenuation in the -12.5 dB to -15 dB range, suggesting a worse quality in comparison to the other additive combinations. This can be due to various reasons. The process depends on a right vacuum level, the quality of the seal of the mould, the amount of entrapped air in the resin during injection and other reasons. As most parameters are controlled, deviations can occur, nevertheless. This can also be seen in the microscopy images for that specimen, which can be found in the annex. The highest additive contents with 15 wt% CSR and 0 wt% and 10 wt% SNP for specimen 7C and 8B, respectively,

showed visible delamination after five impacts, indicated by the larger fraction of attenuation less than -19 dB. In this case, the highest additive combination caused a twice as severe delamination.

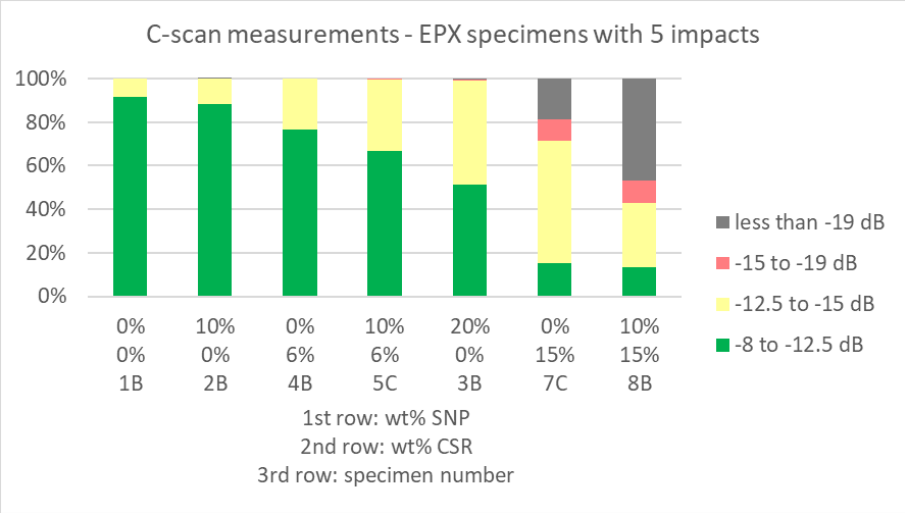

Figure 5.12: Results C-scan - epoxy binder with 5 impacts

Figure 5.13 shows two heat maps. The one on the left relates the core-shell rubber particle and silica nanoparticle content to the relative damage tolerance for epoxy binder specimens impacted five times. The right heat map highlights the influence of CSR and SNP contents on the dynamic viscosity at a temperature of 60 °C. The additive combination of 6 wt% CSR and 20 wt% SNP was not impacted five times. It can be seen that the specimens without any additive contents yielded the highest damage tolerance after five impacts. With increasing additive contents, especially with increasing CSR-content, the damage tolerance decreases to below 30 %. The highest SNP-content without any CSR-particles in it caused a similar decrease, though it is not as much as it is for the CSR particles around 50 %. The smallest decrease in damage tolerance for the specimens with additives are those manufactured with 10 wt% SNP. When comparing it to the viscosities for each additive combination, one can see a correlation between these results. It is not necessarily the additives that cause a decrease in damage tolerance, but rather the ramifications caused by an increased viscosity. These ramifications are an increased number of dry spots and voids, which is further highlighted and explained in the microscopy chapter.

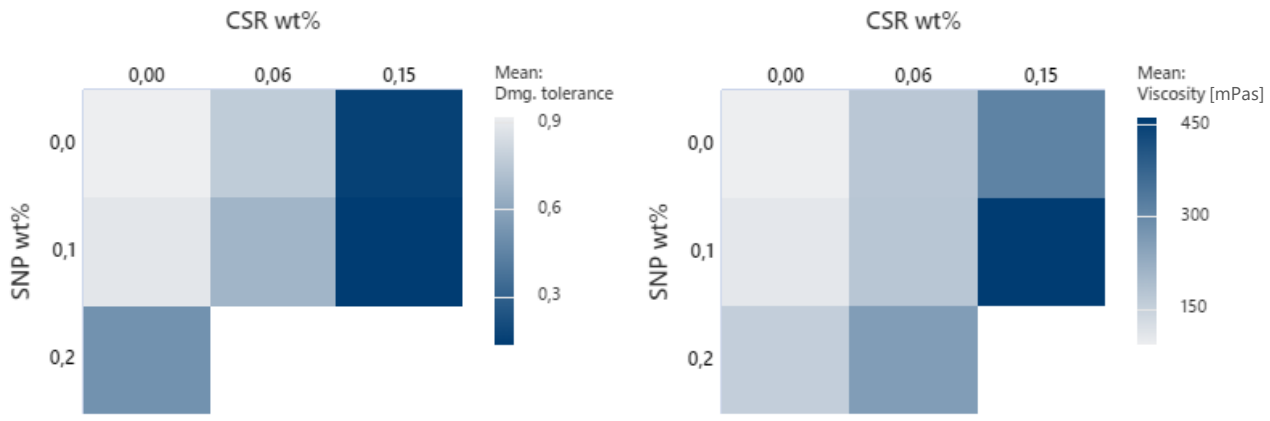

Figure 5.13: Heat maps - left: damage tolerance for epoxy binder specimens with 5 impacts - right: viscosity vs. additive contents

Figure 5.14 shows specimens manufactured with epoxy binder, but instead of showing the damage distribution after five impacts, the damage distribution after 10 impacts is shown. Most specimens show their damage as intended after ten impacts, but due to deviation and high additive contents not all specimens reached 10 impacts, which is in this case specimen 6C2 with 20 wt% SNP and 6 wt% CSR. Apart from the high additive contents – in this case specimen 6 and 8 – no visible delamination occurred after the defined number of impacts. Also, the trend of increasing additive content does not go in line with the increase in damage. It does for specimens 1C, 3C and 4C, but specimen 5B and 2C performed better than the non-additive specimen 1C. Here, specimens from position C are compared with specimen 5B, which is closer to the inlet. Closer to the inlet means that it is less likely to have dry spots or voids. Regardless of that one can see that the highest additive contents caused the severest damage growth. Specimen group 7, which was manufactured with 0 wt% SNP and 15 wt% CSR had dry spots too large to have sufficient specimens and could not be tested for this number of impacts.

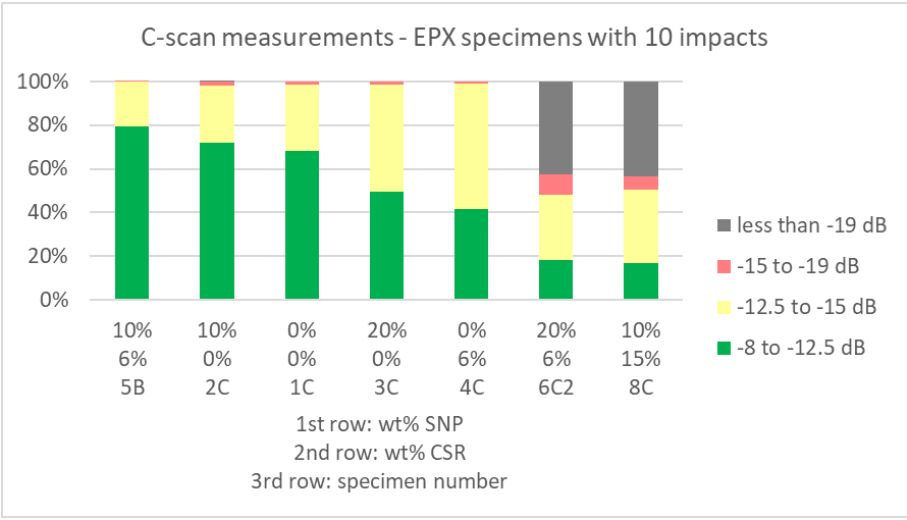

Figure 5.14: Results C-scan - epoxy binder with 10 impacts

Figure 5.15, unlike for the specimens with epoxy binder, shows the 10 best performing specimens manufactured with co-polyester binder after at least one impact. The co-polyester specimens performed significantly worse than the epoxy binder specimens. Most specimens failed after one impact causing visible delamination at the edges. Therefore, it was not possible to compare the specimens after five and 10 impacts like it was done for the epoxy binder specimens. Therefore, the ten specimens with the largest area of lowest attenuation reaching from -8 dB to -12.5 dB and highlighted in green in the diagram are presented. Contradictory to the epoxy binder specimens, the best specimens were the ones with the highest additive content, namely 15 wt% of CSR and 10 wt% SNP. Apart from the specimen with the highest additive combination located at position A, the other specimens from that batch show a trend, which shows increasing damage with every impact. This can be due to the effect of the inlet located in the middle of specimen A, where both fibre washing and uneven surfaces have an influence on the impact performance. However, both specimen C and F made with the highest additive combination showed visible delamination after their last impact. Furthermore, the specimens without any additives at position C and B both failed after the first impact, the specimen at position C almost twice as severe as the one at position B. This can also be due to an increasing number of dry spots due to an increased distance away from the inlet.

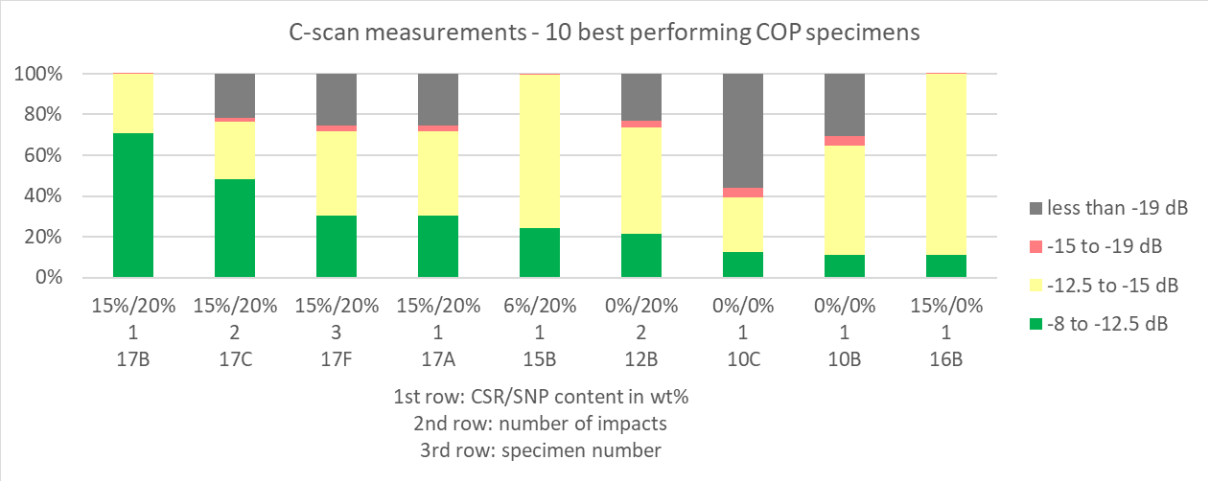

Figure 5.15: Results C-scan - best performing specimens with co-polyester binder

Figure 5.16 shows the Pareto chart of the standardized effects for the factors influencing the damage tolerance. The used data is based on every specimen C-scanned and therefore including both co-polyester and epoxy binder specimens. A significance level of 0.05 is used, which yields the red line at 2.052. Any value higher than that suggests a statistical significance for that parameter. Furthermore, interaction effects can occur, where the parameter alone has a marginal contribution, but the combination does have a significant influence. It can be seen that the binder plays a significant role in the damage tolerance, but the interaction of effect of binder and viscosity is statistically more relevant. This suggest that not only the binder, but also the viscosity of the system during injection has an influence on the damage tolerance. Of course, not the viscosity itself causes a worse damage tolerance, but rather the effects caused by it, such as subpar filling behaviour causing dry spots due to hindered injection or more entrapped air in the injected resin. However, it

is clear that the binder has a significant influence on the damage tolerance, namely making it worse in comparison to the epoxy binder specimen. The position and number of impacts are less significant when considering the data as a whole. However, they should not be neglected, as of course both the position and number of impacts influenced the impact performance. An example is the energy loss analysis, where the position and number of impacts had an effect on the mean energy loss.

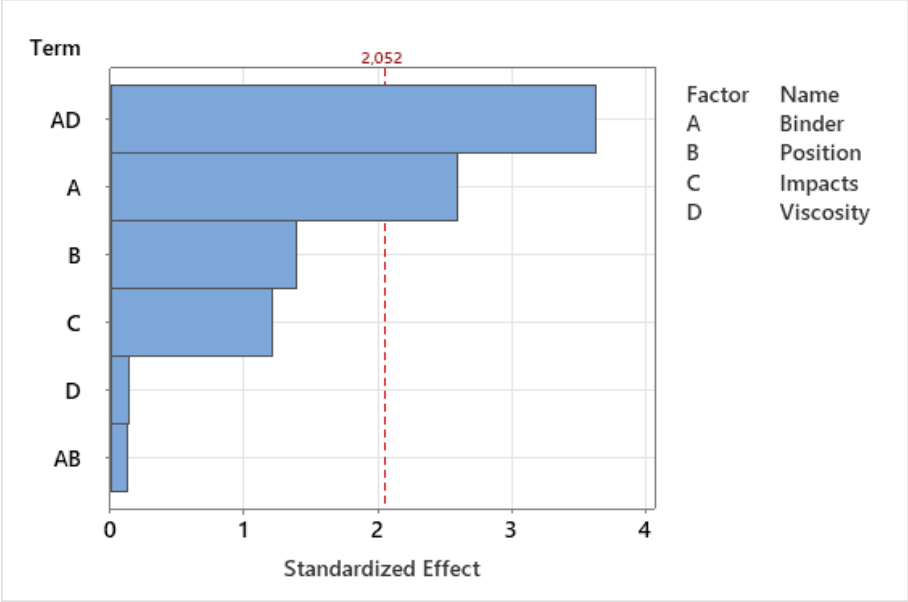

Figure 5.16: Pareto chart of the standardized effects (response is relative damage tolerance; α = 0,05) - input variables: binder, position, impacts, viscosity

As the highest significance is the interaction effect of binder and viscosity, this particular combination was analysed further. Figure 5.17 shows the interaction plot for the relative undamaged area or relative damage tolerance. The x-axis differs between co-polyester binder and epoxy binder. Each data point relates to an injection viscosity, which relates to a specific additive content. However, regardless of the specific additives used, one can see that for viscosities up to 309.2 mPas the damage tolerance or the relative undamaged area is higher for the epoxy binder specimens. The resin mixtures with viscosities of 314.1 mPas and 534.1 mPas show an inverted effect. The damage tolerance for those resin mixtures is higher when paired with the co-polyester binder. When considering the different injection times for co-polyester and epoxy binder specimens, one can assume that a two- to threefold higher permeability for the co-polyester specimens allows for higher additive contents to travel easier through the preform during injection. Faster and easier injections reduce the number of imperfections making the high viscosity resin mixtures performing better than their epoxy binder counterpart. Nevertheless, the number of impacts irrespective on the damage tolerance for that high additive concentration was still lower than for the epoxy binder specimens, suggesting that the binder material is a major cause in regard to the damage tolerance.

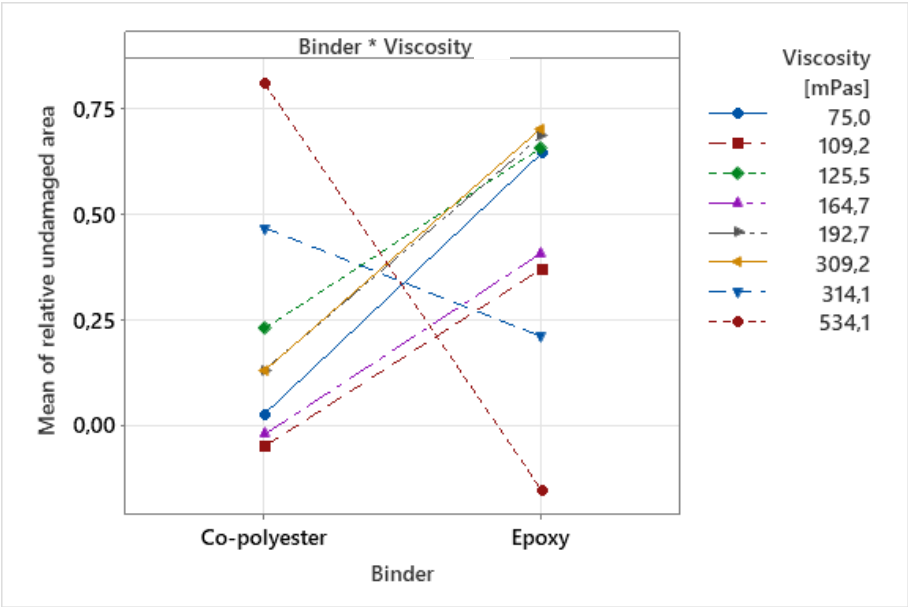

Figure 5.17: Interaction plot for the relative undamaged area - fitted means

When removing the binder variable and only considering the epoxy binder specimens, the following Pareto chart is obtained (see Figure 5.18). The chart now considers the variables position, number of impacts and viscosity of the resin system during injection. Identical to the other Pareto chart above, a significance level of 0.05 is used. The graph shows that no variable can be considered statistically significant, but the influence of the position is marginal in comparison to the viscosity and number of impacts. It is logical that the number of impacts influences the damage tolerance, where an increasing number of impacts causes damage growth, as it can be seen in the images obtained from the ultrasonic testing. The viscosity and its effect on filling behaviour is the main driving factor when it comes to damage tolerance for the specimens manufactured with epoxy binder. This also supports the argument that was made in a previous chapter regarding the energy loss. There, an interaction plot for the mean energy loss related to the position showed a trend, which however was affected by the number of impacts per position. This dependency is to be kept in mind.

When excluding the position from the input variables, as its influence is less significant in comparison to the remaining factors, the viscosity and number of impacts was considered to be the sole contributors affecting the impact performance. This graph is shown in Figure 5.19. It can be seen that both variables are now considered significant when ruling out the influence of the position. As explained previously, the number of impacts logically has an influence on the damage tolerance, but also the ramifications of higher viscosity that come with it. Therefore, regardless of the number of impacts, the impact performance and damage tolerance decreases with increasing viscosity and thus increasing additive contents. To further understand why that is the case, microscopy was done to understand the influence of the viscosity and the permeability on the filling behaviour.

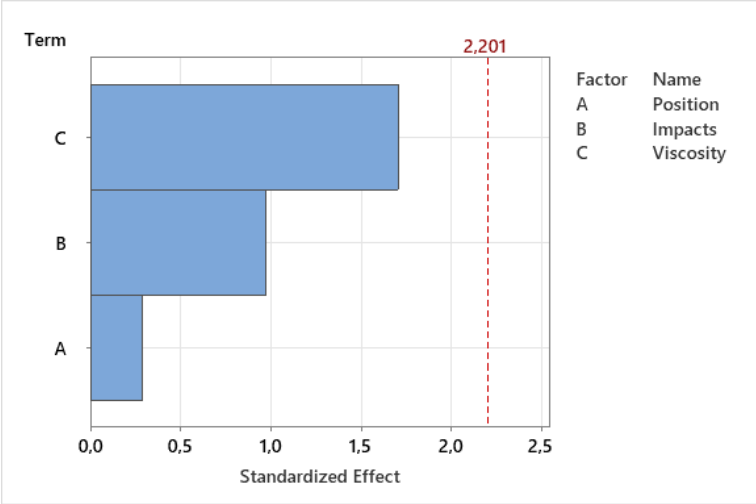

Figure 5.18: Pareto chart of the standardized effects (response is relative damage tolerance; α = 0.05) - only epoxy binder specimens considered - input variables: position, impacts, viscosity

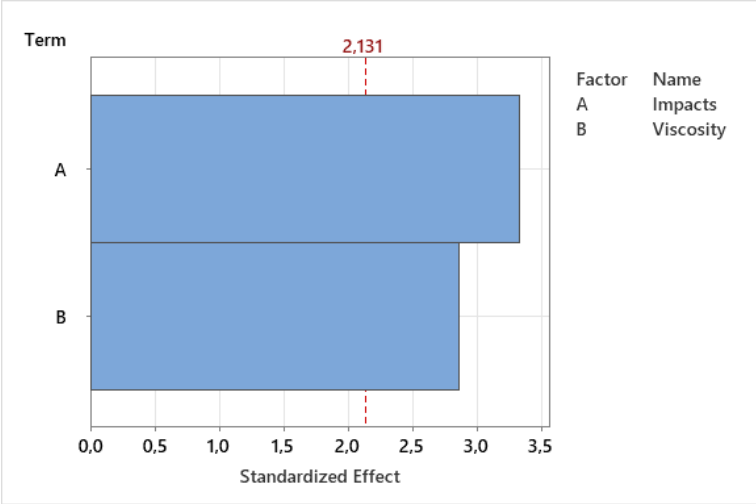

Figure 5.19: Pareto chart of the standardized effects (response is relative damage tolerance; α = 0.05) - only epoxy binder specimens considered - input variables: impacts, viscosity

5.2.4 Microscopy

To further understand the results from the ultrasonic testing, microscopy was done. The impact tolerance of the specimens manufactured with co-polyester binder was considerably less in comparison to the epoxy binder specimens. Taking a look at the microscope images, the co-polyester is clearly visible, making the assumption that the co-polyester dissolves into the epoxy resin during injection and curing invalid. In fact, the co-polyester caused voids inside the specimen (see Figure 5.20). The specimen shown is a specimen manufactured with 10 wt% SNP and 6 wt% CSR. The voids inside the co-polyester suggest that they were there before the impact already. The shape and clear separation from the co-polyester-epoxy interface support this argument. The air can be entrapped during the application process with the hotmelt machine, but also during the consolidation or preforming process. With applied vacuum before the injection process these

voids grow in size due to the pressure difference. The surrounding co-polyester acts as a barrier making it impossible for the epoxy to impregnate these areas.

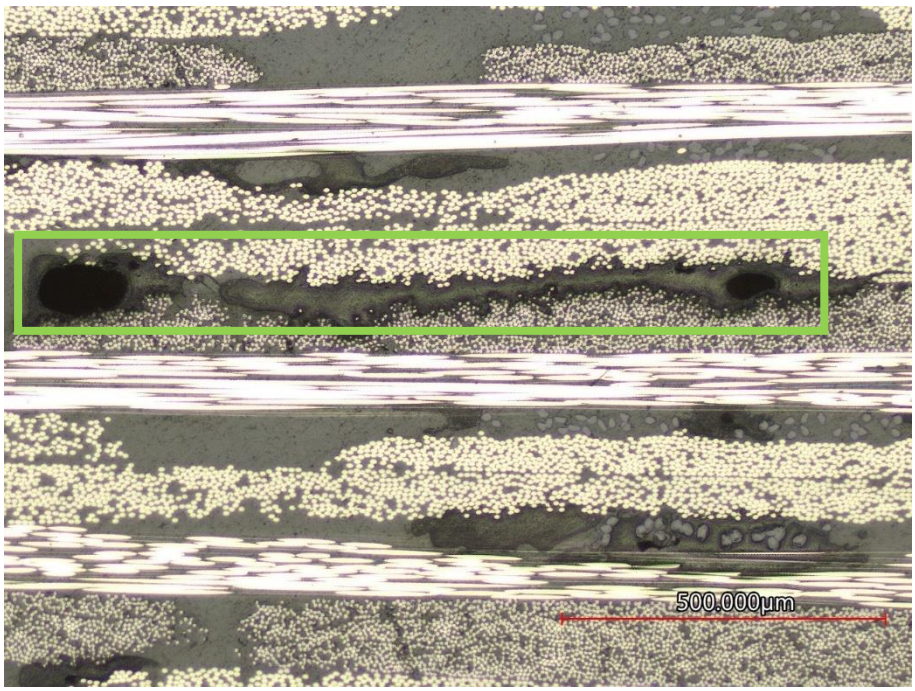

Figure 5.20: Co-polyester phase (highlighted in green box) with voids (specimen 14C-1)

Further analysing the co-polyester specimens shows that also fibre failure occurred due to impact. Figure 5.21 shows a co-polyester specimen without any additives inside. The green box highlights the interface between carbon fibre plain weave and carbon fibre non-crimp fabric. Interply delamination is visible, but also delamination between the differently oriented carbon fibre strands of the plain weave delaminated. The region is rich of co-polyester. The co-polyester is darker in comparison to the epoxy matrix when looking at it with an optical microscope. This image supports the argument of the co-polyester acting as a weaker link in the structure and causing crack and damage nucleation sites.

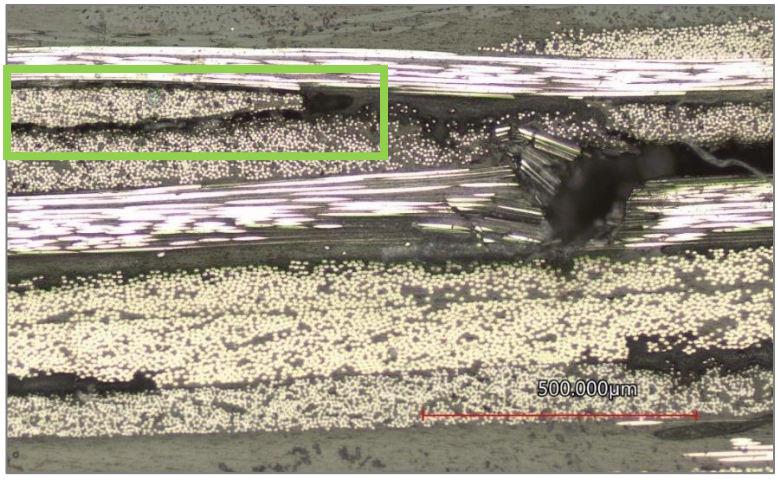

Figure 5.21: Co-polyester specimen without additives (position 1) – fibre failure due to impact – green box highlighting delaminated co-polyester rich region

Figure 5.22 shows another co-polyester specimen, where a void is highlighted with a green box surrounding it. The co-polyester phase can be seen in the interface between the 0/90 degree and ±45 degree ply. Both, the fact that the co-polyester already entrapped air prior to the injection process, but also the co-polyester hindering the resin flow are contributes to the formation of these voids. In this image, the flow direction during injection is from right to left. As the interlaminar zone is filled with co-polyester, the resin is deviating through the fibres, where the permeability is significantly lower than in the interlaminar area. The co-polyester blocking the way for the resin flowing in the interlaminar zone is highlighted by a blue in the image. Furthermore, in this particular case the adjacent fibres are not in flow direction, but either 45 degrees or 90 degrees to the flow direction for the ±45 degree ply and 0/90 degree ply, respectively. A magnification of this image is shown in Figure 5.23. Apart from the highlighted void in the previous image, another void between the blue and green box of the previous image is visible. It also highlights an insufficient impregnation, which can be caused by both the hindered resin flow and the entrapped air during hotmelt application and consolidation. Of course, not both scenarios need to be valid, but either one is sufficient to cause void formation, especially given the higher viscosity of the resin system due to the additives included.
Further microscopy images show the highlighted observation, where the co-polyester causes imperfections to the specimen in form of imperfect impregnation.

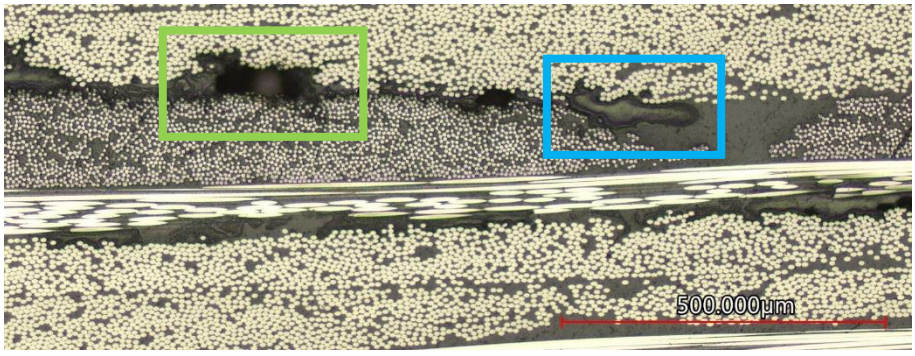

Figure 5.22: Co-polyester specimen with 10 wt% CSR and 6 wt% SNP (position 3) - visible is a co-polyester induced void (green box) – flow direction during injection from right to left – co-polyester hindering flow (blue box)

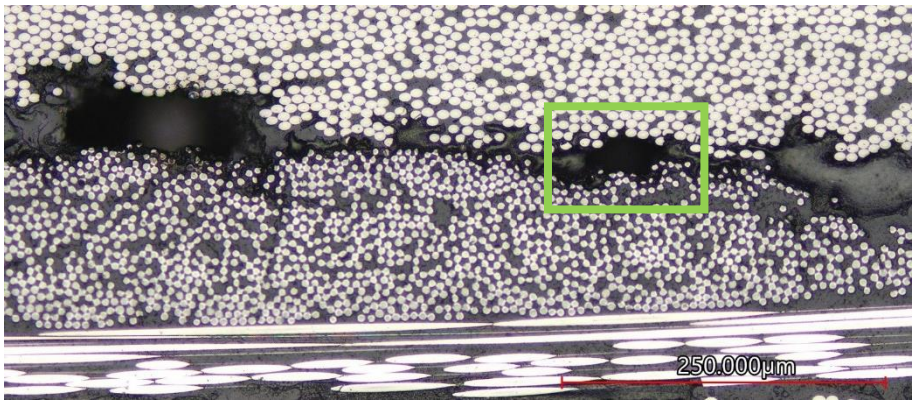

Figure 5.23: Magnification of Figure 5.22 – another void visible (green box)

Looking at the microscopy images from the specimens manufactured with epoxy binder, no separate phase was identified. However, similar to the co-polyester specimens, voids are present (see Figure 5.24). A set of different specimens with different additive combinations were analysed and compared. Furthermore, images from a scanning electron microscope yield further insight.

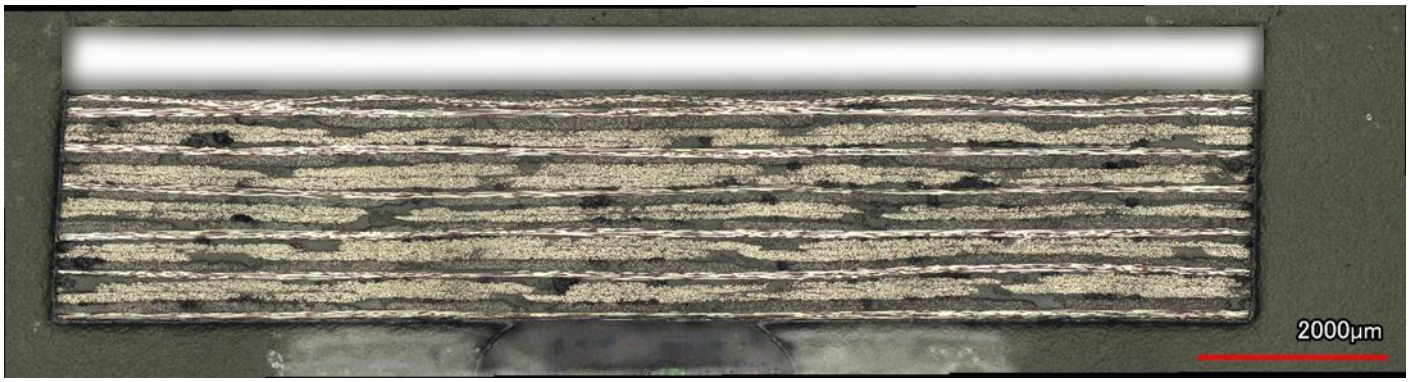

Figure 5.24: Epoxy binder specimen with 20 wt% SNP and 0 wt% CSR (position 1) - voids visible in the interlaminar layers - flow direction right to left – partially blurred

Figure 5.25 shows an epoxy binder specimen with 6 wt% of CSR and 10 wt% of SNP particles. A void formed in a 90-degree ply is presented in the centre of the upper half of the image. Furthermore, right behind the scale marking in the bottom right of the image a smaller void is present. To the left of this void the stitching yarn can be seen. The additive combination shown in the image has an approximately 2.5 times higher viscosity in comparison to the unmodified resin system. A higher viscosity makes injection take longer, which with a decreased permeability in the interlaminar region can cause dry spots or subpar impregnation. Furthermore, this specimen was impacted 10 times, which also may have contributed to the void's size, namely causing cracks inside the surrounding matrix causing the void to grow. The void position indicates that the voids are caused by the binder material located in that region.

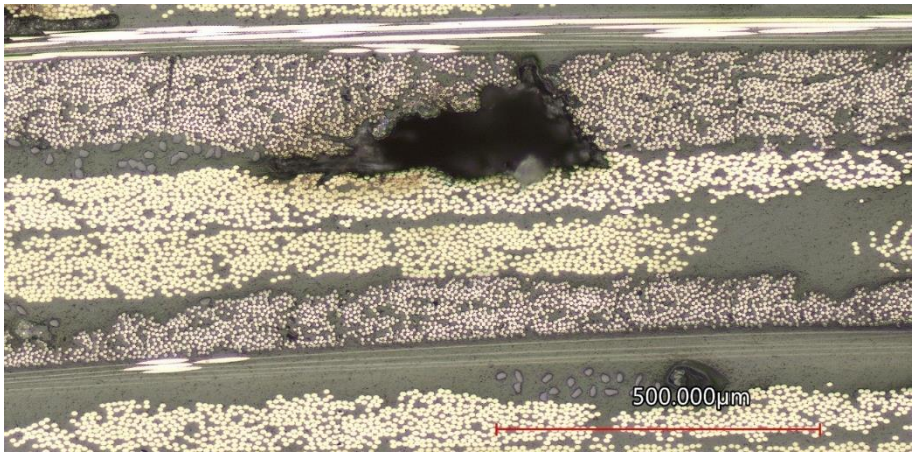

Figure 5.25: Epoxy binder specimen with 6wt% CSR and 10 wt% SNP (position 1) – a void formed in a 90-degree layer – flow direction right to left

Similar to the previous image, Figure 5.26 shows voids formed. This image shows an epoxy binder specimen with 6 wt% CSR and 0 wt% SNP particles. The void shown in the centre of the image is mainly interlaminar but breached partially into the adjacent ±45 ply. This sample was impacted 10 times as well. Apart from the largest void in the centre of the image multiple smaller voids formed in the interlaminar zone between 0/90-degree and ±45-degree plies. Voids mostly formed in these zones, whereas inside an NCF-ply, namely intralaminar between a 0- and 90-degree layer or between a +45- and -45-degree layer, the number of voids is lower than for interlaminar voids. Referring to the sample preparations, the epoxy binder was applied to one side of the NCF plies, meaning that when patching each ply on top of each other that there is binder in every interlaminar region between two NCF-plies, but rarely inside one ply, which consists of two perpendicular to each other oriented unidirectional layers.

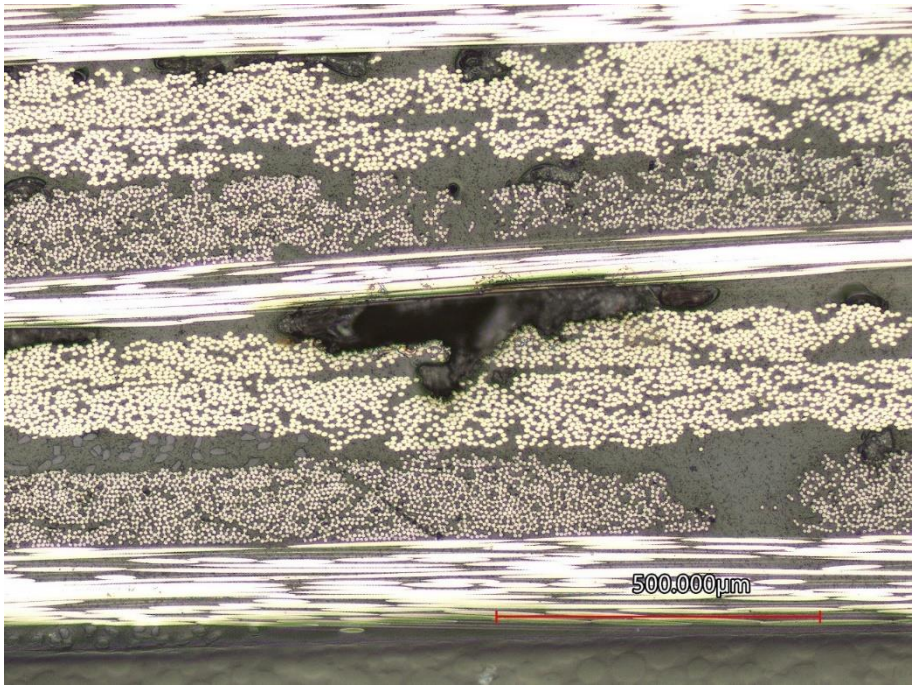

Figure 5.26: Epoxy binder specimen with 6 wt% CSR and 0 wt% SNP (position 1) – flow direction right to left

Additionally, to the optical microscopy, scanning electron microscopy was performed to further understand the damage growth in the specimens. Throughout all specimens analysed, microcracks were present. A specimen with microcracks is shown in Figure 5.27. This epoxy binder specimen is manufactured with 6 wt% CSR and apart from the microcrack in the centre of the image, fibre-matrix debonding is visible in the bottom left corner. The number of impacts for this specimen is 10. This type of specimen does not allow for identifying the individual particles incorporated into the matrix. For that, resin samples without fibres would be more suitable to identify the particles incorporated into the matrix. However, this would have made impact testing impossible and therefore the gained data in this regard would not be beneficial. Nevertheless, insight into the damage progression is yielded, which is further supported by other SEM images.

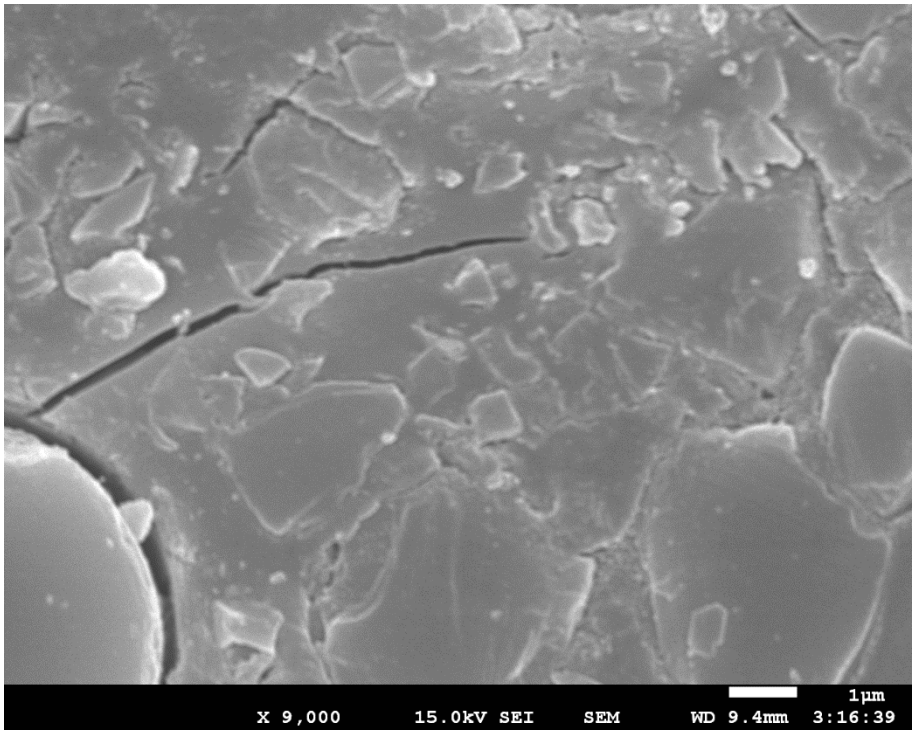

Figure 5.27: Microcracks (epoxy binder specimen with 6 wt% CSR)

Apart from microcracks originating from debonding fibre-matrix interfaces, further cracks were identified originating in the voids shown in the previous figures. This is highlighted in Figure 5.28. The surface is magnified by a factor of 100, whereas the previous figure was magnified by a factor of 9000. The yellow circles highlight voids, where cracks are present. This specimen was shot at 10 times and is manufactured with 20 wt% of silica nanoparticles. The binder in this specimen is epoxy. This shows that due to impacts the voids grow by cracks originating from there. A larger number of voids therefore offers more possible options for cracks to initiate and propagate. A close up of the void in the centre of Figure 5.28 is shown in Figure 5.29. The significantly larger void in comparison to the surrounding voids shows cracks forming at the back of the void. Furthermore, the crack extended to the right with pieces of matrix material debonding and breaking. Similar to the optical microscope images, the scanning electron microscope images show the voids between the individual NCF plies. Based on this one can see that the cracks tend to propagate horizontally. Horizontally in this case means that the cracks follow along the interface between to NCF-plies, turning the voids and propagating cracks into delaminated areas. When looking at specimens which visually delaminated, this conclusion is logical. With multiple impacts the matrix' strength decreases to a point, where the impact of 37.5 J is sufficient to delaminate large portions of the specimen. Apart from the largest void in the centre of the image and the yellow highlighted areas, multiple smaller voids can be seen throughout the entire image. These also act as crack nucleation sites and can grow with an increasing number of impacts.

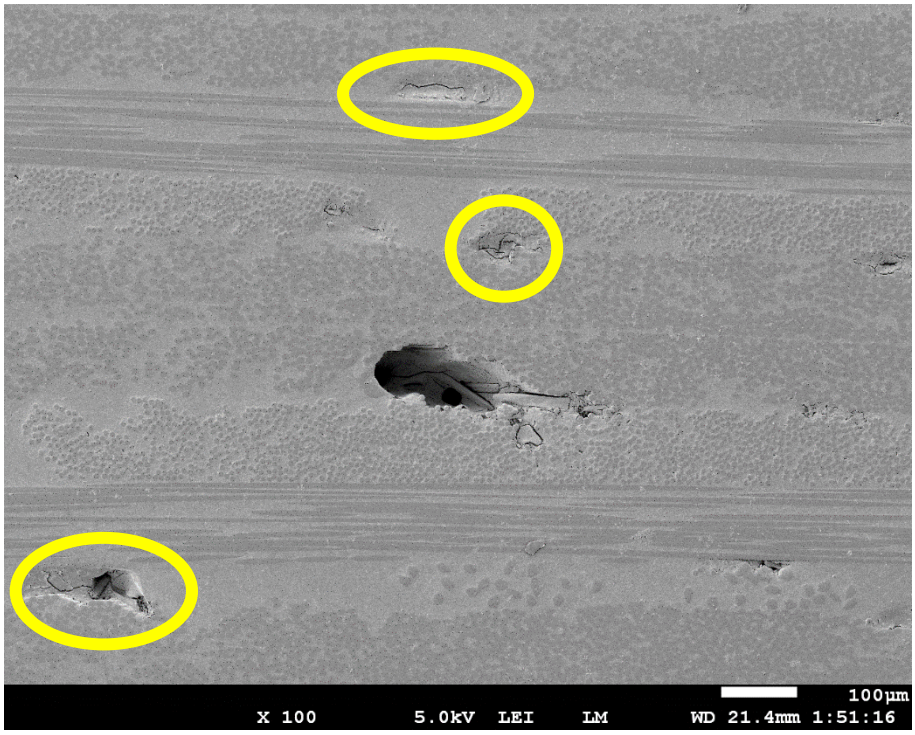

Figure 5.28: Cracking voids - lower magnification (epoxy binder specimen with 20 wt% SNP)

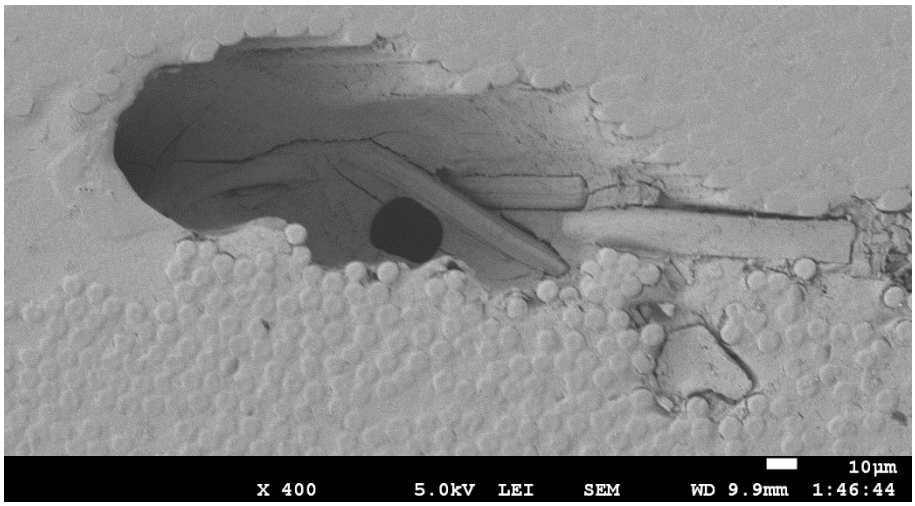

Figure 5.29: Cracking voids – higher magnification (epoxy binder specimen with 20 wt% SNP)

Apart from optical 2D-scanning, 3D-scanning was done to visualise the plastic deformation of the specimen's front face. A too severe plastic deformation can have an influence on the flight path for example. Figure 5.30 shows the 3D-scanned surface of specimens manufactured with epoxy binder and 15 wt% CSR and 0 wt% SNP. The number of impacts range from 0 to 5, where the second specimen from the left was impacted 5 times and then second specimen from the right was not impacted. The remaining specimens were short at once. It can be seen that both with increasing number of impacts, but also depending on the position the deformation varied. As this is a resin mixture with high additive content and therefore high viscosity, specimen quality was not ideal due to the mentioned dry spot around specimen E. The steel bents upwards at the sides when impacted by the ball causing the matrix to be tensioned, whereas right in the impact zone the matrix is

compressed. This is also visible by the colourmap, when comparing the impacted specimens to the non-impacted one. For most cases, the centre is lower in thickness direction, whereas the sides are higher resulting in an increased thickness there.

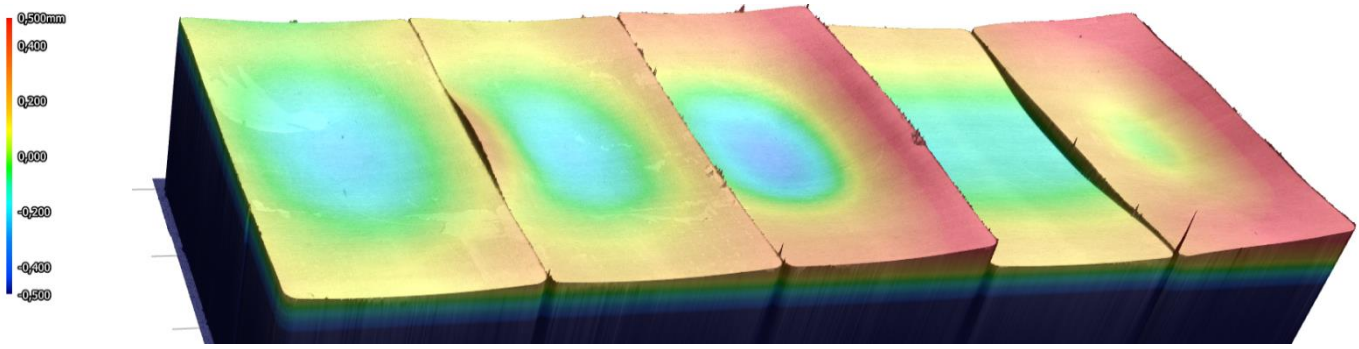

Figure 5.30: 3D-scanned surface of specimens manufactured with epoxy binder (15 wt% CSR, 0 wt% SNP) - specimens from left to right: B, C, D, E, F – scale goes from +0.5 mm to -0.5 mm

Figure 5.31 shows another set of specimens. These specimens are also manufactured with epoxy binder and instead of 15 wt% CSR particles, it is now 6 wt% CSR particles. The difference to these specimens is better specimen quality due to better injection, which is because of the lower viscosity of the resin system. The dry spot at specimen E is smaller, too. These specimens were impacted 5, 10, 2 and 0 times going from left to right. Similar to the previous set of 3D-scanned specimens, here both an increase in impacts, but also a position closer to the dry spot caused more plastic deformation. The edges also bent upwards, whereas the centre remains similar to the non-impacted specimen. The other 3D scans are shown in the annex.

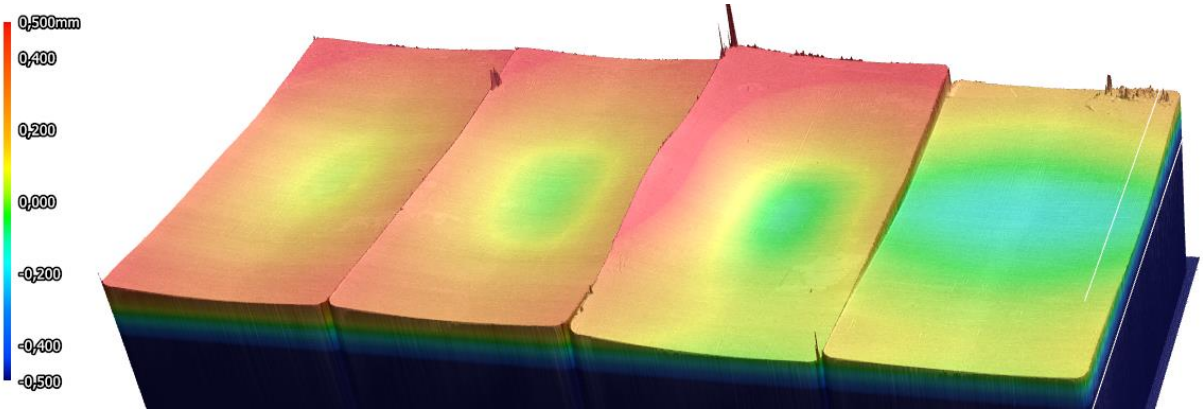

Figure 5.31: 3D-scanned surface of specimens manufactured with epoxy binder (6 wt% CSR, 0 wt% SNP) - specimens from left to right: B, C, D, E - scale goes from +0.5 mm to -0.5 mm

5.2.5 Differential scanning calorimetry

The DSC measurements to determine the glass transition temperature showed no difference depending on the binder type used. Furthermore, the difference was less than 1 % depending on the inlet or outlet side,

allowing to assume that no filtering of additives occurred. Figure 5.32 shows two heatmaps for the glass transition temperatures averaged for each additive combination grouped by the first and second run. The left heatmap ranges from 94.16 °C for 20 wt% SNP and 0 wt% CSR to 104.01 °C for 0 wt% SNP and 15 wt% CSR. The right heatmap ranges from 107.42 °C for 20 wt% SNP and 0 wt% CSR to 122.09 °C for 0 wt% CSR and 15 wt% CSR. A trend is visible, where with increasing CSR content the glass transition temperature increases, whereas with increasing SNP content the glass transition temperature decreases. The reason for the different temperature values are not caused by the additive itself, as those particles are chemically inert. However, the resin formulation the particles are dispersed in have different properties in comparison to the resin part of the fast curing resin system. This difference causes a change in the crosslink density, overall molecular structure consisting of more or less flexible backbones.

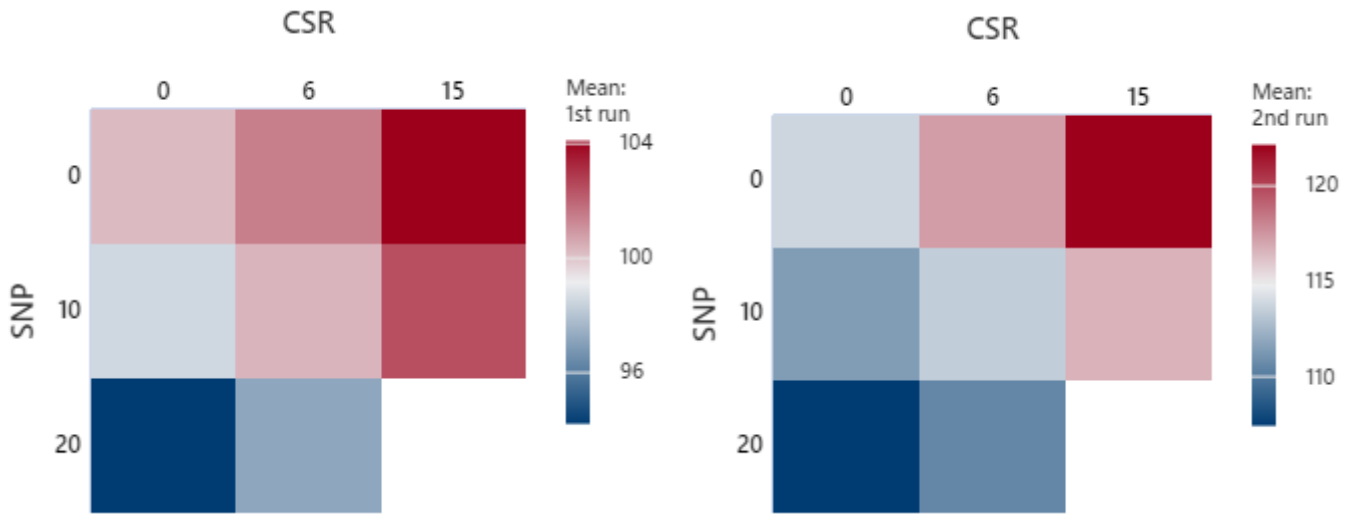

Figure 5.32: Heatmap showing the influence on Tg after curing cycle (left) and after heating to 150 °C with 10 °C/min ramp heating (right) depending on additive contents in wt%

5.2.6 Discussion

The impact testing series yielded various insights into the influence of different binder materials and additives incorporated into the resin matrix. The goal with this testing series was to identify how different additive combinations influence the impact performance while keeping the process parameters as close as possible to the actual process. Literature review showed that additives such as core-shell rubber particles and silica nanoparticles can improve the damage tolerance of an epoxy resin. However, the manufacturing process plays a significant role when it comes to damage tolerance, too. The process needs to be capable of producing perfect, void-free specimens to be able to neglect the effect of the manufacturing process on the impact performance.

As the injection times showed, regardless of the binder used, with increasing viscosity the injection time increased, which is in line with Darcy's law. Considering the epoxy binder specimens, injection times were in

the 4- to 9-minute range, suggesting a permeability low enough to avoid proper impregnation. For comparison, a non-bindered preform's injection time is around 45 seconds with a non-modified epoxy resin. The assumption of an increased void formation due to an increased resin viscosity was further analysed with C-scan images and analyses, but also microscopy. The C-scan analyses in combination with a DoE-analysis showed the damage growth with increasing number of impacts, but also highlighted, which variables had the most significant influence on that damage growth. When only considering the epoxy binder specimens, no statistical significance was identified, but it showed that the most-contributing factors are the viscosity and the number of impacts. It is logical that an increasing number of impacts has an influence on the damage growth. The influence of the increasing resin viscosity would not be the cause for an accelerated damage growth, but rather the voids and dry spots that form due to the higher viscosity and therefore due to the worsened filling behaviour. This hypothesis was further analysed with the images obtained from microscopy. The images show that more voids formed with higher additive contents, but it also needs to kept in mind that these specimens were impacted already. For this, it would have been ideal to quantify the void contents before the specimens were shot at. However, for this to be accurate, multiple measurements along the injection direction might have been necessary, as the impregnation was better close to the inlet in all cases and decreased until specimen E, which is the second to last specimen out of the six specimens cut from the RTM manufactured CFRP-steel hybrid sheet. Microscopy showed that the voids and damage zones were always located in-between two NCF-plies, not inside the biaxial NCF ply itself. This allowed to assume that the epoxy binder hindered the injection, which is still in its solid powder form due to the temperature, even though it was melted once in the oven process. If the epoxy powder dissolves into the resin during injection, was not determined. However, it does melt during the curing cycle and therefore cured with the fast curing resin. If during injection dry spots form around the non-melted epoxy binder, these entrapped voids will remain at that location supporting the findings from the microscopy images.

For the co-polyester specimens, the injection times were in the 1- to 5-minute range, which is about half as much in comparison to the epoxy binder specimens. Even though the permeability was higher for the co-polyester specimens, their impact performance was significantly worse. Most specimens failed after a single impact, where the delamination propagated to the edges making further impact testing pointless. Specimens who did not show visible delamination after one impact, also did not show the typical damage formation around the impact zone, as it was the case for the epoxy binder specimens. Instead, the quality appeared to be worse due to a larger amount of high attenuation areas. The areas with higher attenuation are assumed to be due to the co-polyester, which did not dissolve into the epoxy resin. The microscopy images support this argument, but also highlighted that air is entrapped inside the co-polyester for a number of specimens analysed. This air is either introduced during the application with the hot-melt machine or during preforming. Either way, with applied vacuum these air pockets grow in size due to the pressure difference and then act as damage nucleation sites. Furthermore, the binder distribution is inhomogeneous, which does not matter for the preforming, as the tackiness is still sufficient, but can influence impact tolerance instead.

The energy loss analysis was done to identify, whether the additives incorporated into the matrix, or the binder have an influence on the energy loss due to impact. The energy loss for the co-polyester was higher in all cases when comparing it to the epoxy binder specimens.

5.2.7 Concluding remarks

The matrix toughening testing series yielded two main results. Comparing the epoxy binder to the co-polyester binder, a significant difference in impact tolerance was observed. The co-polyester caused the structure to be considerably weaker causing it to fail after a single impact for most specimens. The other result is the reduced impact tolerance with increasing additive contents, which is contradictory to the insights gained from the literature review. The cause for this has been identified by the filling behaviour, which worsens with increasing viscosity and therefore increasing void contents. This hypothesis was supported with insights gained from both C-scan data and microscopy, which was used to perform a more detailed DoE-analysis. However, this hypothesis could not be proofed entirely. For that, more insight into the void contents and filling behaviour would be necessary. As this testing series was aimed at improving the damage tolerance of steel-CFRP hybrid structures, the results are valuable notwithstanding. The results show that an increasing additive content needs to come with a process ensuring perfect filling behaviour. Of course, at some point the viscosity and therefore the additive content is too high to consider the process feasible but avoiding entrapped air prior to the injection and ensuring a sufficient permeability by adjusting the area weight of the epoxy binder, better filling is obtainable.

Nevertheless, given the obtained results, further valuable insights can be obtained by comparing perfectly filled specimens with a specific additive concentration and no additives at all. This way, filling behaviour, void contents and impact tolerance can be compared, and the hypothesis constructed based on the findings during this project can be further analysed.

6 Conclusion and recommendations

Options to improve the damage tolerance of steel-CFRP hybrid structures prone to impact were analysed at *adultimum ag* in Gossau, Switzerland. This project offered an interlink between scientific research and commercial industrialisation by aiming for an improved material combination with respect to economical manufacturing in terms of cycle time and part quality.
Silica nanoparticles (SNP) and core-shell-rubber particles (CSR) were analysed alongside different binder materials. Furthermore, different interface fabric materials to improve the bond between steel and CFRP were tested and compared. The technology used was resin transfer moulding (RTM), as it is implemented at *adultimum ag*. The following main research question is formulated:

> "What is the influence on the impact performance when adding additives and interface materials to CFRP-steel hybrid structures - using the manufacturing process implemented at *adultimum ag* – and how do filling behaviour and injection times affect these results?"

The main research question is answered in chapter 6.1 and recommendations for further research are proposed in chapter 6.2.

6.1 Conclusion

Epoxy resins are thermosetting polymers, which are known for their brittle behaviour. The impact tolerance of carbon fibre reinforced epoxy resins can be improved with additives of either thermoplastic, elastomeric or non-organic materials. Most common materials used and researched are silica nanoparticles and rubber particles, either it being reactive elastomers or so-called core-shell rubber particles. These particles have various influences on the properties of the base resin, such as increasing or decreasing the modulus, glass transition temperature or exothermic peak during reaction. However, those additives can also improve the fracture toughness. For this project core-shell-rubber particles and silica nanoparticles were chosen to perform an impact testing series to understand how the particles influence the impact performance while keeping the manufacturing process effects in mind. The additive master batches usually have significantly higher viscosities in comparison to the base resin, causing an overall increase in viscosity. Particle concentrations were chosen based on literature and company references.
When considering steel-CFRP hybrids, the interface between those two experience significant stresses only due to manufacturing alone. Both materials have different coefficients of thermal expansion, which causes thermal stresses frozen in the material due to the curing cycle. Furthermore, both materials have different stiffnesses and moduli making them perform differently. To improve the bond between those two components,

different interface materials were analysed in a separate experiment. Based on literature review, short fibre aramid veils with different area weights, but also glass weave were considered. Common toughening effects when including fabric materials are fibre bridging or fibre pull out causing the bond strength to increase. The bond strength was tested with a mandrel peel test setup.

The hypothesis developed after the performed literature review stated that an increasing additive content can improve the impact tolerance and therefore damage tolerance of steel-CFRP hybrid structures. However, an increasing additive content causes increasing viscosities, which can have detrimental effects on the filling behaviour. Apart from that, the permeability of the preform to be impregnated, plays a crucial role in the filling behaviour and filling time. Various analyses were performed to understand the results obtained. C-scan footage and its quantified data showed that for specimens preformed with an epoxy binder, a decreasing impact and damage tolerance was obtained with increasing additive contents. Specimens manufactured with a co-polyester binder showed significantly worse impact and damage tolerance in comparison to the epoxy binder specimens, regardless of the additive concentrations used. To further understand the cause for this, microscopy was done. The co-polyester acted as a weak point in the structure causing premature failure of the specimens. For the epoxy binder specimens, it was identified that the binder concentration caused voids in the interlaminar regions, which is due to the decreased permeability in this region caused by the binder paired with increasing resin viscosities. Furthermore, DoE-analyses (design of experiments) were performed, to understand which factors contribute to the reduced impact and damage tolerance. The results support the assumption that the ramifications due to higher viscosities have a significant influence on the damage tolerance.

Contradictory to the constructed hypothesis, the effect of toughening the matrix was detrimental rather than beneficial with increasing additive contents. However, this effect is due to the increased viscosities yielding an imperfect filling behaviour paired with the reduced permeability due to the binder in the interlaminar regions. The used manufacturing process – namely RTM – and the chosen process parameters made dry spots inevitable.

For the interface toughening, the peel test results obtained showed that when using no interface material at all, but rather curing the steel sheet right onto the bi-axial non-crimp fabric (NCF) – which was used to compose the main CFRP-body – the bond strength was the highest. The glass weave used acted as a barrier and caused matrix rich regions. Contradictory to originally anticipated, the glass weave did not interlock with the roughened steel surface. The aramid veils did show fibre bridging and fibre pull out and performed better than the glass weave specimens. However, when using no interface material at all, entire carbon fibre bundles were pulled out during the peel test increasing the bond strength.

6.2 Recommendations

To further support the results obtained during this project, the experiment should be repeated with a reduced test scope, but an increased number of tests for the same additive concentration. This gives further insight

into the influence of the manufacturing process and how to improve the process in regard to the filling behaviour. Then, the toughening performance with the additives could be analysed in a following step. However, void content analyses can support the arguments done in this project and should be carried out alongside the repeated experiment mentioned. Furthermore, epoxy binder contents and its influence on the permeability should be analysed, as the injection times were significantly higher with epoxy binder than they were for the co-polyester binder specimens. An ideal spot, where good automated preforming is feasible, but also a low permeability is crucial for the overall automated manufacturing process.

7 References

[1] C. Soutis, “Fibre reinforced composites in aircraft construction,” *Progress in Aerospace Sciences*, vol. 41, no. 2, pp. 143–151, 2005, doi: 10.1016/j.paerosci.2005.02.004.

[2] F. C. Campbell, *Manufacturing processes for advanced composites*. New York, NY, USA: Elsevier, 2004.

[3] P. K. Mallick, *Polymer matrix composites: Processing and applications*. Boca Raton, FL, USA: CRC Press, 2018.

[4] Joe Carruthers, *What is Resin Transfer Moulding (RTM)?* Accessed on: Dec. 1 2020. [Online]. Available: https://coventivecomposites.com/explainers/resin-transfer-moulding-rtm/

[5] T. Kruckenberg and R. Paton, *Resin transfer moulding for aerospace structures*. Dordrecht, The Netherlands: Springer, 2013.

[6] R. R. Johnson, M. H. Kural, G. B. Mackey, “Thermal expansion properties of composite materials,” National Aeronautics and Space Administration, Sunnyvale, California, NASA-CR-165632, Jul. 1 1981.

[7] F. Cverna, *Thermal properties of metals - 2. Thermal Expansion*. Materials Park, Ohio, USA: ASM International, 2002.

[8] G. J. Appleby-Thomas, P. J. Hazell, and G. Dahini, “On the response of two commercially-important CFRP structures to multiple ice impacts,” *Composite Structures*, vol. 93, no. 10, pp. 2619–2627, 2011, doi: 10.1016/j.compstruct.2011.04.029.

[9] W. J. Cantwell and J. Morton, “The impact resistance of composite materials — a review,” *Composites*, vol. 22, no. 5, pp. 347–362, 1991, doi: 10.1016/0010-4361(91)90549-V.

[10] H. Ullah, A. R. Harland, and V. V. Silberschmidt, “Damage and fracture in carbon fabric reinforced composites under impact bending,” *Composite Structures*, vol. 101, pp. 144–156, 2013, doi: 10.1016/j.compstruct.2013.02.001.

[11] S. Abrate, “Impact on Laminated Composite Materials,” *Applied Mechanics Reviews*, vol. 44, no. 4, pp. 155–190, 1991, doi: 10.1115/1.3119500.

[12] Emile S. Greenhalgh, “Defects and damage and their role in the failure of polymer composites,” in *Failure Analysis and Fractography of Polymer Composites*, Emile S. Greenhalgh: Elsevier, 2009, pp. 356–440.

[13] V. V. Silberschmidt, *Dynamic deformation, damage and fracture in composite materials and structures*. Amsterdam, The Netherlands: Elsevier, 2016.

[14] D. S. Kammer, “Slip Fronts at Frictional Interfaces:A Numerical and Theoretical Study,” , 2014.

[15] C. T. Sun and Z.-H. Jin, *Fracture Mechanics*: Elsevier, 2012.

[16] G. R. Irwin, “Analysis of stresses and strains near the end of a crack transversing a plate,” *Trans. ASME, Journal of Applied Mechanics*, vol. 24, pp. 361–364, 1957.

[17] A. A. Griffith, “VI. The phenomena of rupture and flow in solids,” *Philosophical Transactions of the Royal Society of London. Series A, Containing Papers of a Mathematical or Physical Character*, vol. 221, 582-593, pp. 163–198, 1921, doi: 10.1098/rsta.1921.0006.

[18] M. Janssen, J. Zuidema, and R. Wanhill, *Fracture Mechanics*: CRC Press, 2004.

[19] A. Keller, H. M. Chong, A. C. Taylor, C. Dransfeld, and K. Masania, “Core-shell rubber nanoparticle reinforcement and processing of high toughness fast-curing epoxy composites,” *Composites Science and Technology*, vol. 147, pp. 78–88, 2017, doi: 10.1016/j.compscitech.2017.05.002.

[20] A. Keller, K. Masania, A. C. Taylor, and C. Dransfeld, “Fast-curing epoxy polymers with silica nanoparticles: properties and rheo-kinetic modelling,” *J Mater Sci*, vol. 51, no. 1, pp. 236–251, 2016, doi: 10.1007/s10853-015-9158-y.

[21] A. J. Kinloch, K. Masania, A. C. Taylor, S. Sprenger, and D. Egan, “The fracture of glass-fibre-reinforced epoxy composites using nanoparticle-modified matrices,” *J Mater Sci*, vol. 43, no. 3, pp. 1151–1154, 2008, doi: 10.1007/s10853-007-2390-3.

[22] A. C. Garg and Y.-W. Mai, “Failure mechanisms in toughened epoxy resins—A review,” *Composites Science and Technology*, vol. 31, no. 3, pp. 179–223, 1988, doi: 10.1016/0266-3538(88)90009-7.

[23] H. Kargarzadeh, I. Ahmad, and I. Abdullah, “Mechanical Properties of Epoxy–Rubber Blends,” in *Handbook of Epoxy Blends*, J. Parameswaranpillai, N. Hameed, J. Pionteck, and E. M. Woo, Cham: Springer International Publishing, 2016, pp. 1–36.

[24] A. Zotti, S. Zuppolini, M. Zarrelli, and A. Borriello, “Fracture Toughening Mechanisms in Epoxy Adhesives,” in *Adhesives - Applications and Properties*, A. Rudawska: InTech, 2016.

[25] S. Awang Ngah and A. C. Taylor, “Toughening performance of glass fibre composites with core–shell rubber and silica nanoparticle modified matrices,” *Composites Part A: Applied Science and Manufacturing*, vol. 80, pp. 292–303, 2016, doi: 10.1016/j.compositesa.2015.10.036.

[26] T. H. Hsieh, A. J. Kinloch, K. Masania, J. Sohn Lee, A. C. Taylor, and S. Sprenger, “The toughness of epoxy polymers and fibre composites modified with rubber microparticles and silica nanoparticles,” *J Mater Sci*, vol. 45, no. 5, pp. 1193–1210, 2010, doi: 10.1007/s10853-009-4064-9.

[27] B. B. Johnsen, A. J. Kinloch, R. D. Mohammed, A. C. Taylor, and S. Sprenger, “Toughening mechanisms of nanoparticle-modified epoxy polymers,” *Polymer*, vol. 48, no. 2, pp. 530–541, 2007, doi: 10.1016/j.polymer.2006.11.038.

[28] D. Quan and A. Ivankovic, “Effect of core–shell rubber (CSR) nano-particles on mechanical properties and fracture toughness of an epoxy polymer,” *Polymer*, vol. 66, pp. 16–28, 2015, doi: 10.1016/j.polymer.2015.04.002.

[29] S. M. George, P. Vijayan, A. Surendran, C. V. Pious, and S. Thomas, “Nanostructures and the toughening of thermosets,” in *Thermosets*: Elsevier, 2018, pp. 173–229.

[30] M. S. Goyat, S. Rana, S. Halder, and P. K. Ghosh, “Facile fabrication of epoxy-TiO2 nanocomposites: A critical analysis of TiO2 impact on mechanical properties and toughening mechanisms,” *Ultrasonics sonochemistry*, vol. 40, Pt A, pp. 861–873, 2018, doi: 10.1016/j.ultsonch.2017.07.040.

[31] D. J. Bray *et al.,* “The modelling of the toughening of epoxy polymers via silica nanoparticles: The effects of volume fraction and particle size,” *Polymer*, vol. 54, no. 26, pp. 7022–7032, 2013, doi: 10.1016/j.polymer.2013.10.034.

[32] A. M. Díez-Pascual, “Mechanical Properties of Epoxy/Thermoplastic Blends,” in *Handbook of Epoxy Blends*, J. Parameswaranpillai, N. Hameed, J. Pionteck, and E. M. Woo, Cham: Springer International Publishing, 2016, pp. 1–32.

[33] P. van Velthem *et al.,* “Influence of thermoplastic diffusion on morphology gradient and on delamination toughness of RTM-manufactured composites,” *Composites Part A: Applied Science and Manufacturing*, vol. 72, pp. 175–183, 2015, doi: 10.1016/j.compositesa.2015.02.012.

[34] M. V. Lobanov, A. I. Gulyaev, and A. N. Babin, “Improvement of the impact and crack resistance of epoxy thermosets and thermoset-based composites with the use of thermoplastics as modifiers,” *Polym. Sci. Ser. B*, vol. 58, no. 1, pp. 1–12, 2016, doi: 10.1134/S1560090416010048.

[35] B.-Z. Huang, X.-Z. Hu, and J. Liu, “Modelling of inter-laminar toughening from chopped Kevlar fibers,” *Composites Science and Technology*, vol. 64, 13-14, pp. 2165–2175, 2004, doi: 10.1016/j.compscitech.2004.03.014.

[36] Z. Sun, J. Jeyaraman, S. Sun, X. Hu, and H. Chen, “Carbon-fiber aluminum-foam sandwich with short aramid-fiber interfacial toughening,” *Composites Part A: Applied Science and Manufacturing*, vol. 43, no. 11, pp. 2059–2064, 2012, doi: 10.1016/j.compositesa.2012.06.002.

[37] M.-S. Sohn and X.-Z. Hu, “Mode II delamination toughness of carbon-fibre/epoxy composites with chopped Kevlar fibre reinforcement,” *Composites Science and Technology*, vol. 52, no. 3, pp. 439–448, 1994, doi: 10.1016/0266-3538(94)90179-1.

[38] M. Yasaee, I. P. Bond, R. S. Trask, and E. S. Greenhalgh, “Mode II interfacial toughening through discontinuous interleaves for damage suppression and control,” *Composites Part A: Applied Science and Manufacturing*, vol. 43, no. 1, pp. 121–128, 2012, doi: 10.1016/j.compositesa.2011.09.026.

[39] Z. Sun, S. Shi, X. Hu, X. Guo, J. Chen, and H. Chen, “Short-aramid-fiber toughening of epoxy adhesive joint between carbon fiber composites and metal substrates with different surface morphology,” *Composites Part B: Engineering*, vol. 77, pp. 38–45, 2015, doi: 10.1016/j.compositesb.2015.03.010.

[40] Z. Sun, X. Hu, S. Sun, and H. Chen, “Energy-absorption enhancement in carbon-fiber aluminum-foam sandwich structures from short aramid-fiber interfacial reinforcement,” *Composites Science and Technology*, vol. 77, pp. 14–21, 2013, doi: 10.1016/j.compscitech.2013.01.016.

[41] R. M. Groves, “3.12 Inspection and Monitoring of Composite Aircraft Structures,” in *Comprehensive Composite Materials II*: Elsevier, 2018, pp. 300–311.

[42] Jolly *et al.,* “Review of Non-destructive Testing (NDT) Techniques and their Applicability to Thick Walled Composites,” *Procedia CIRP*, vol. 38, pp. 129–136, 2015, doi: 10.1016/j.procir.2015.07.043.

[43] NDT Resource Center, *Modes of Sound Wave Propagation*. Accessed on: Jan. 20 2021. [Online]. Available: https://www.nde-ed.org/EducationResources/CommunityCollege/Ultrasonics/Physics/modepropagation.htm

[44] NDT Resource Center, *Wave Propagation*. Accessed on: Jan. 20 2021. [Online]. Available: https://www.nde-ed.org/EducationResources/CommunityCollege/Ultrasonics/Physics/wavepropagation.htm

[45] D. J. Coleman, “Measurement of Choroidal Pulsation with M-Scan Ultrasound,” *American Journal of Ophthalmology*, vol. 71, no. 1, pp. 363–365, 1971, doi: 10.1016/0002-9394(71)90411-9.

[46] Laura-Kristin Scholz, *Ultrasonic Pulse-Echo Method*. Accessed on: Jan. 20 2021. [Online]. Available: https://wiki.tum.de/display/zfp/Ultrasonic+Pulse-Echo+Method

[47] R. Prakash, *Non-destructive testing techniques*. Tunbridge Wells: New Academic Science, 2012.

[48] *Standard Test Method for Floating Roller Peel Resistance of Adhesives,* D3167-10: ASTM International, West Conshohocken, 2017.

[49] *Standard Test Method for Climbing Drum Peel for Adhesives,* D1781-98: ASTM International, West Conshohocken, 2012.

[50] *Standard Test Method for Peel Resistance of Adhesives (T-Peel Test),* D1876-08: ASTM International, West Conshohocken, 2015.

[51] L. F. Kawashita, D. R. Moore, and J. G. Williams, “Comparison of Peel Tests for Metal–Polymer Laminates for Aerospace Applications,” *The Journal of Adhesion*, vol. 81, no. 6, pp. 561–586, 2005, doi: 10.1080/00218460590954557.

[52] S. T. de Freitas and J. Sinke, “Test method to assess interface adhesion in composite bonding,” *Appl Adhes Sci*, vol. 3, no. 1, 2015, doi: 10.1186/s40563-015-0033-5.

[53] ADMET, Inc., *ASTM D1781* | *Adhesives* | *Peel Testing*. Accessed on: Feb. 22 2021. [Online]. Available: https://www.admet.com/testing-applications/testing-standards/astm-d1781-climbing-drum-peel-testing/

[54] ADMET, Inc., *ASTM D1876* | *Adhesives* | *Peel Testing*. Accessed on: Feb. 22 2021. [Online]. Available: https://www.admet.com/testing-applications/testing-standards/astm-d1876-adhesive-peel-strength-testing/

[55] F. Sacchetti, W. Grouve, L. L. Warnet, and I. F. Villegas, “Woven fabric composites: Can we peel it?,” *Procedia Structural Integrity*, vol. 2, pp. 245–252, 2016, doi: 10.1016/j.prostr.2016.06.032.

[56] F. Sacchetti, W. J. Grouve, L. L. Warnet, and I. Fernandez Villegas, “Interlaminar fracture toughness of 5HS Carbon/PEEK laminates. A comparison between DCB, ELS and mandrel peel tests,” *Polymer Testing*, vol. 66, pp. 13–23, 2018, doi: 10.1016/j.polymertesting.2017.12.005.

[57] L. Daelemans *et al.,* “Bisphenol A based polyester binder as an effective interlaminar toughener,” *Composites Part B: Engineering*, vol. 80, pp. 145–153, 2015, doi: 10.1016/j.compositesb.2015.05.044.

[58] Y. Su, M. de Rooij, W. Grouve, and L. Warnet, “Characterisation of metal–thermoplastic composite hybrid joints by means of a mandrel peel test,” *Composites Part B: Engineering*, vol. 95, pp. 293–300, 2016, doi: 10.1016/j.compositesb.2016.03.055.

[59] R. E. Maples, *Petroleum Refinery Process Economics (2nd Edition)*: PennWell, 2000.

Annex

C-scan images for all impact specimens

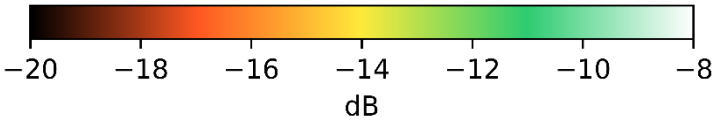

1ABCDF - EPXCSR0SNP0

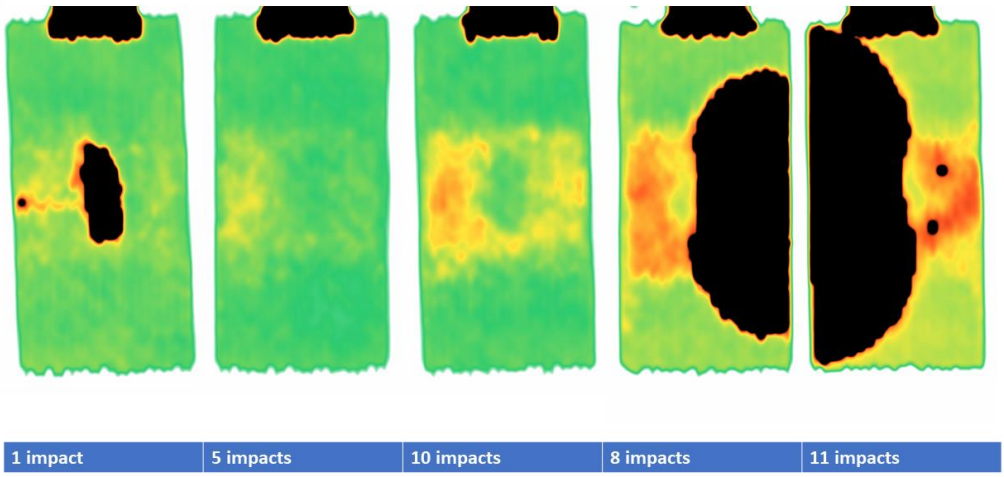

2ABCD - EPXCSR0SNP10

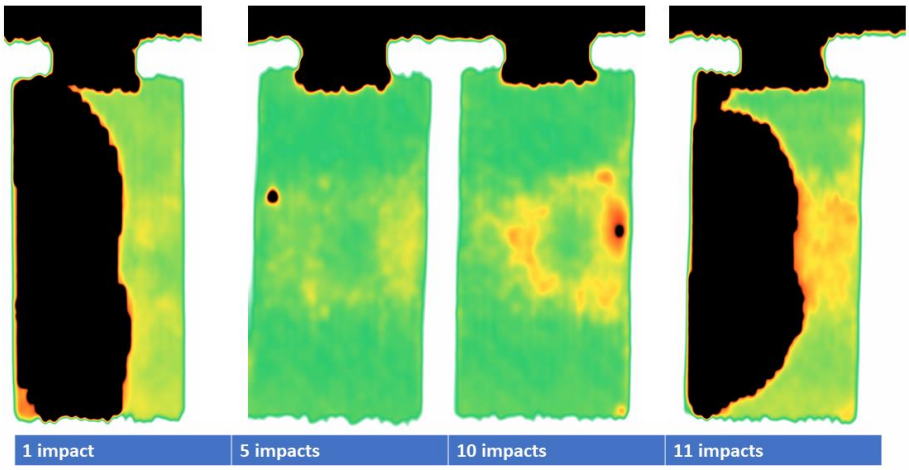

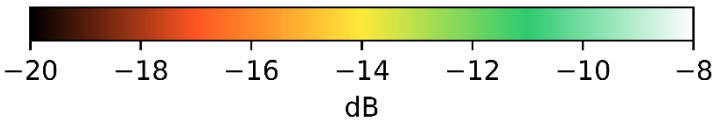

3ABCF - EPXCSR0SNP20

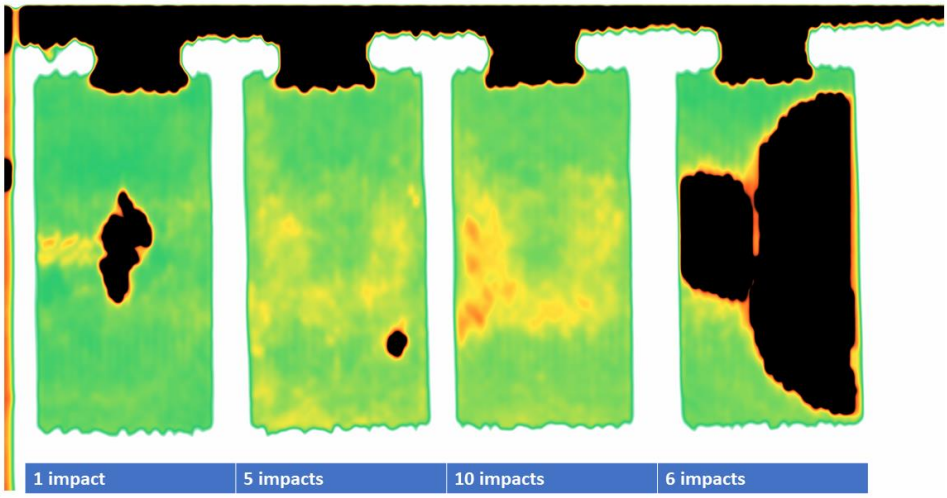

4ABCD - EPXCSR6SNP0

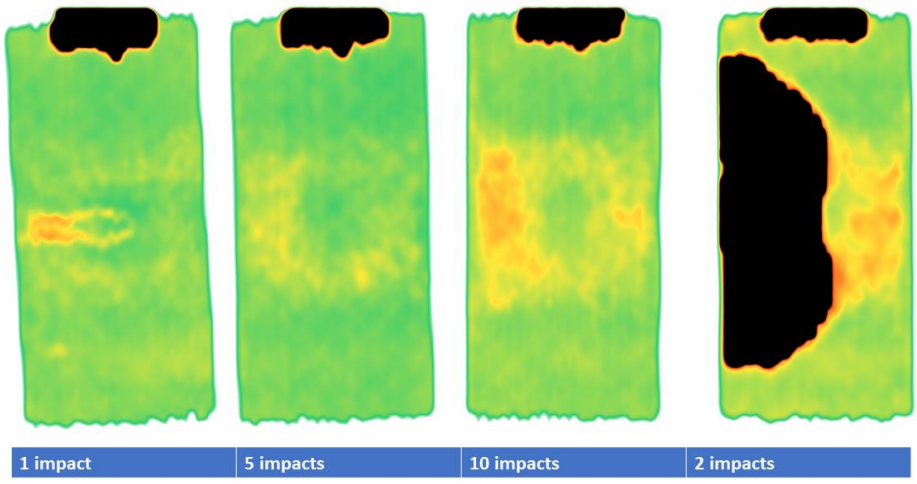

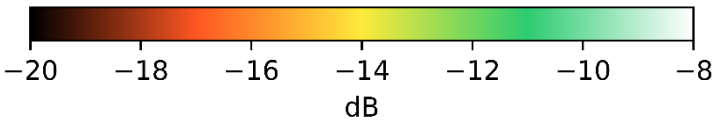

5ABCD - EPXCSR6SNP10

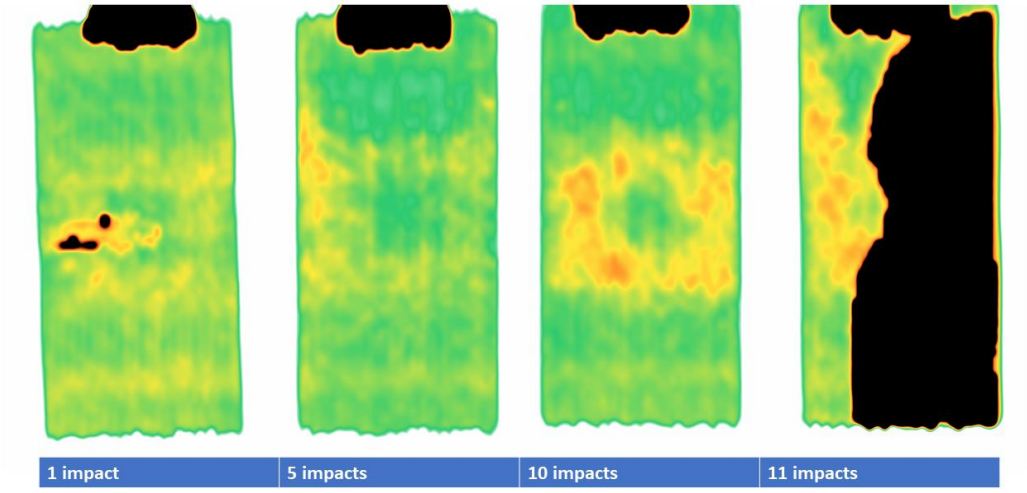

6B62BC - EPXCSR6SNP20

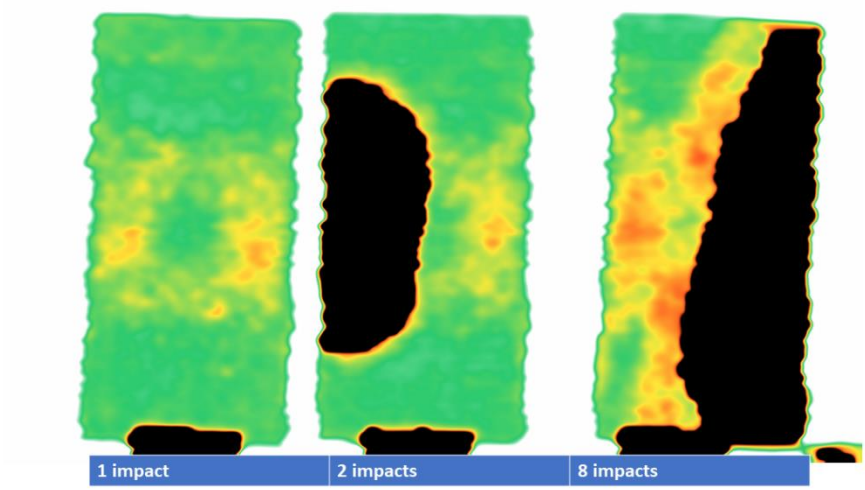

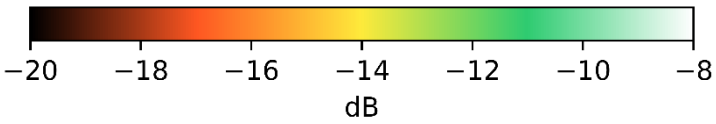

7BCDF – EPXCSR15SNP0

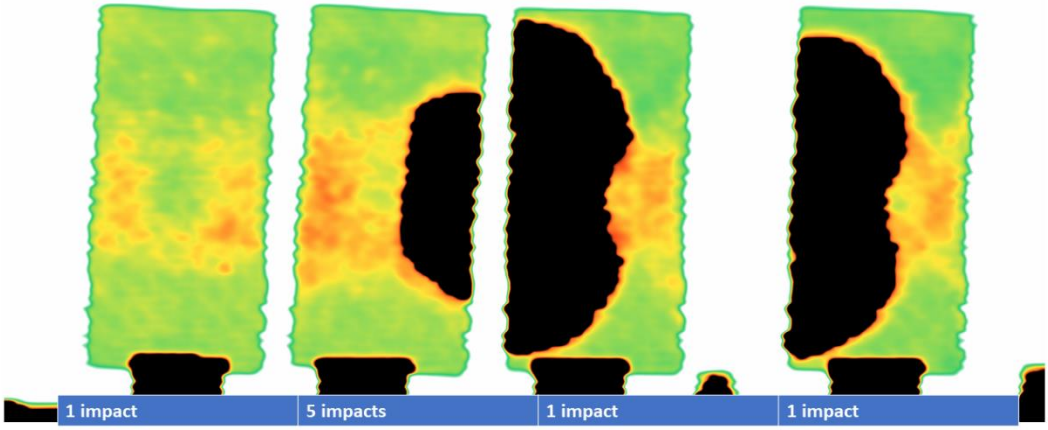

8BC – EPXCSR15SNP10

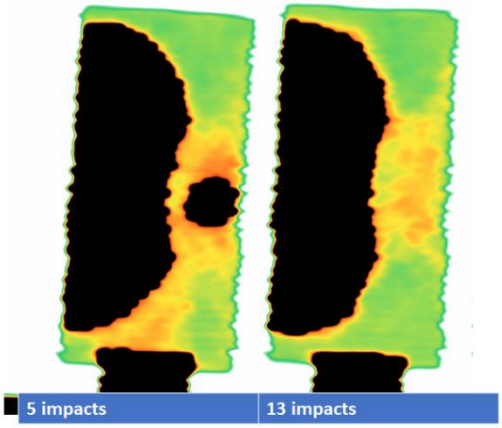

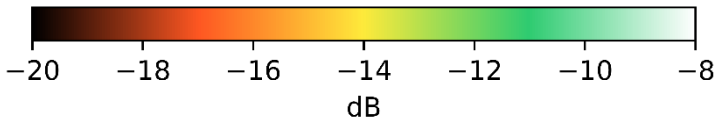

10ABCD – COPCSR0SNP0

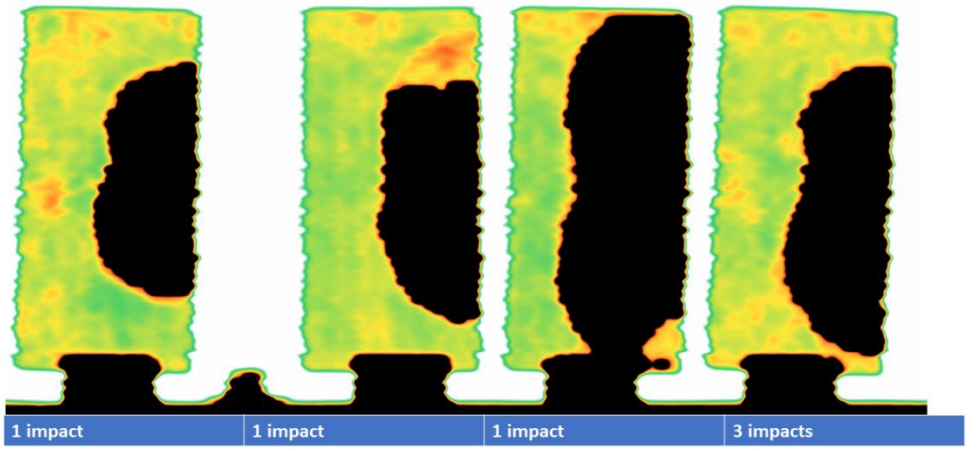

11ABCD – COPCSR0SNP10

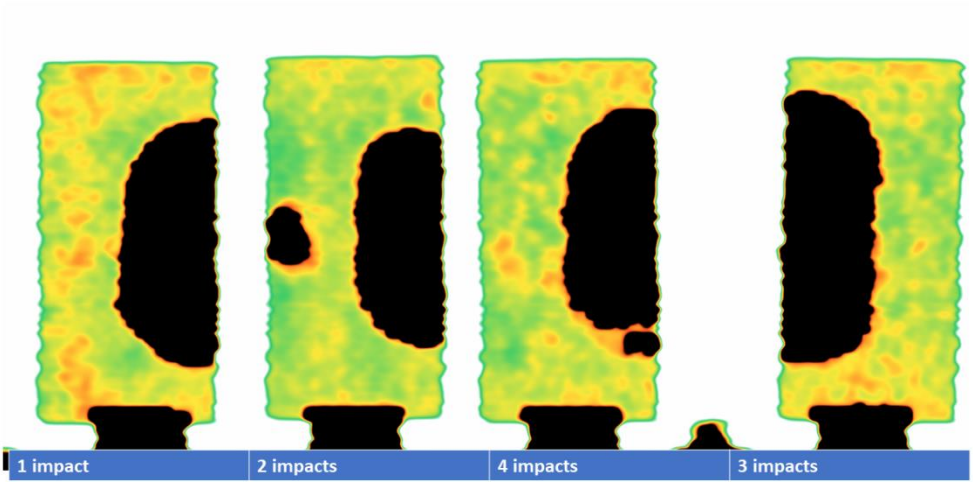

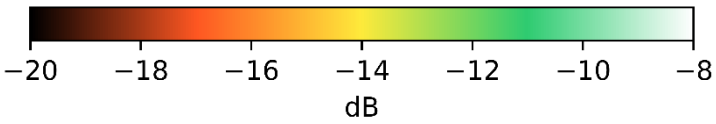

12ABC – COPCSR0SNP20

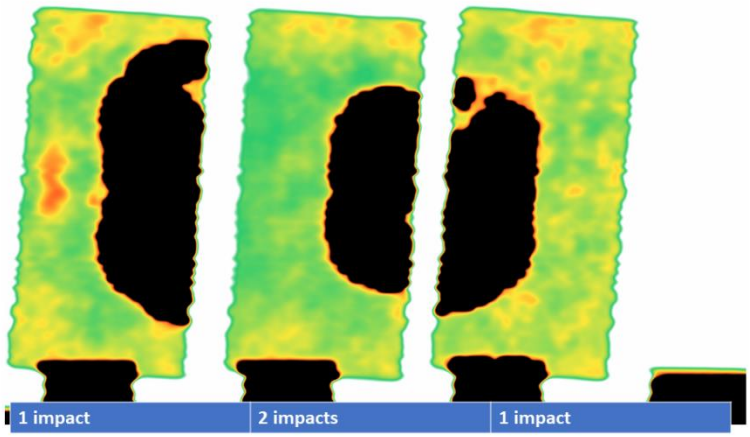

13ABCD – COPCSR6SNP0

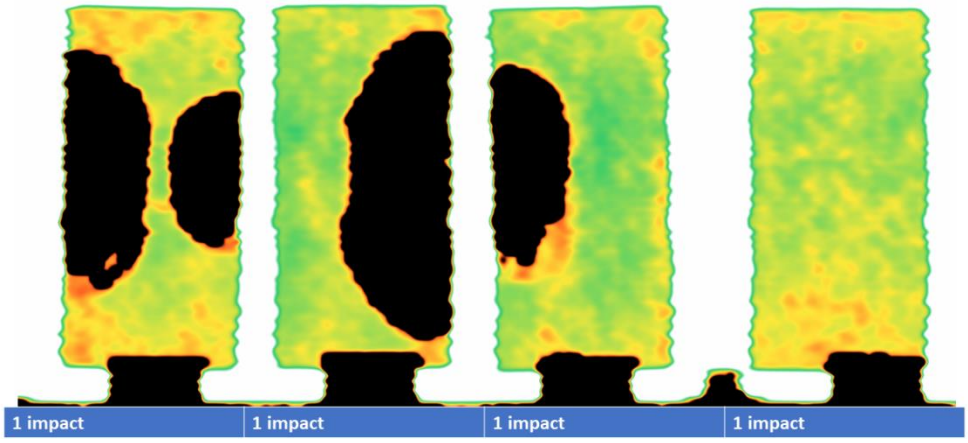

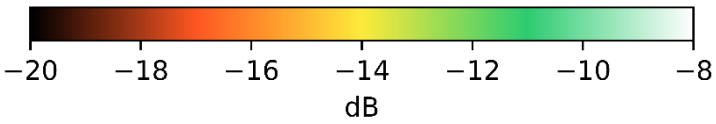

14ABCF – COPCSR6SNP10

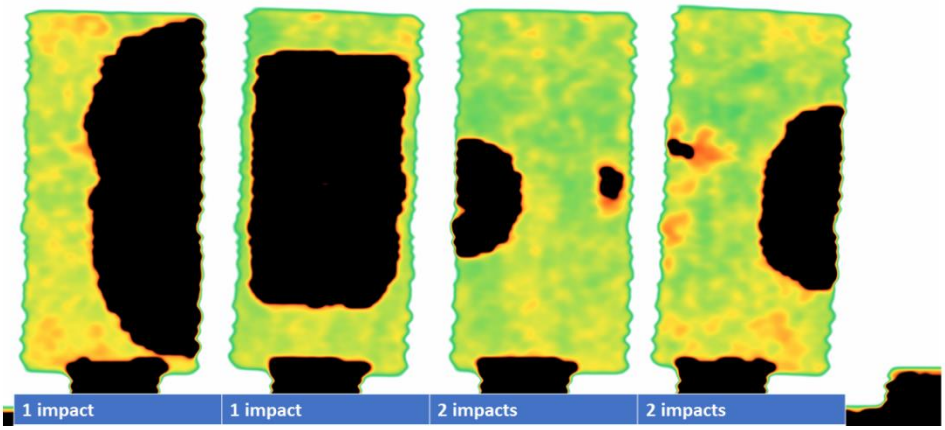

15ABCF – COPCSR6SNP20

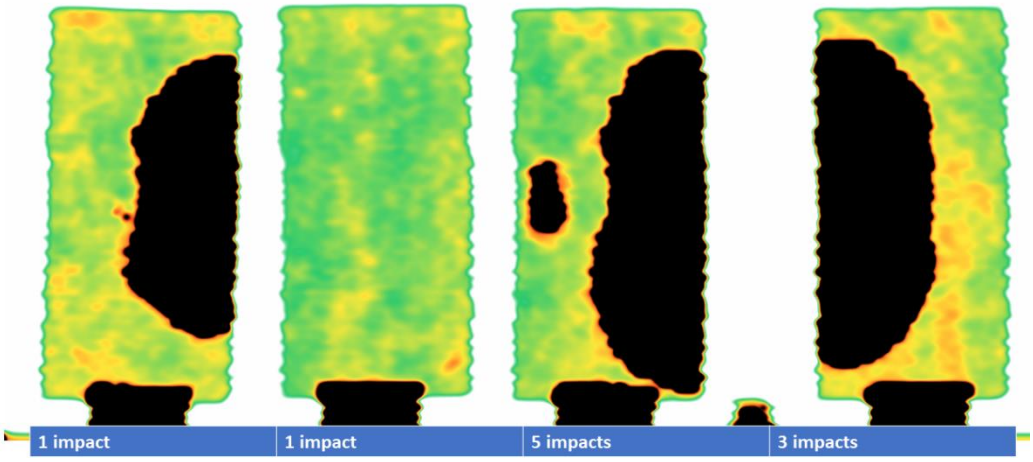

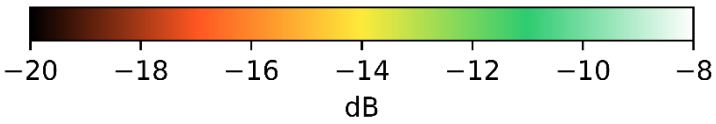

16ABCF – COPCSR15SNP0

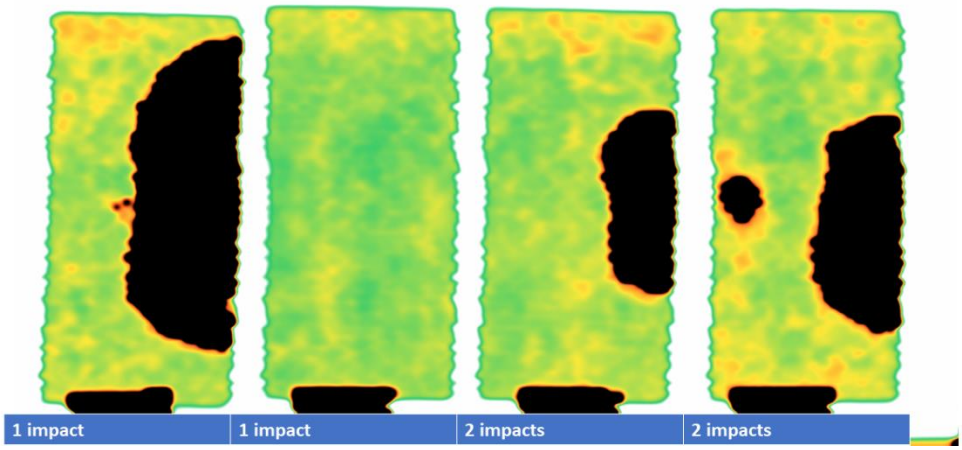

17ABCF – COPCSR15SNP10

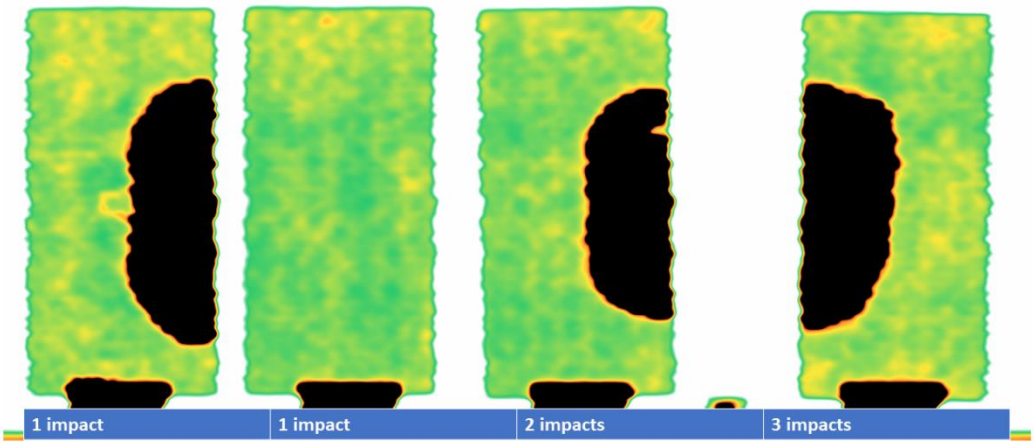

Quantified C-scan measurements for all specimens

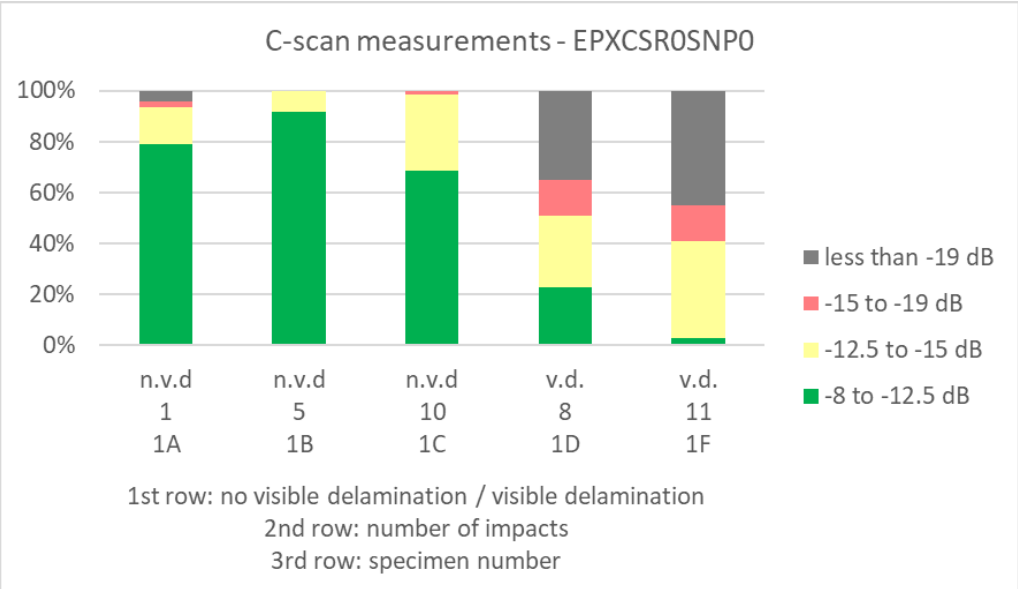

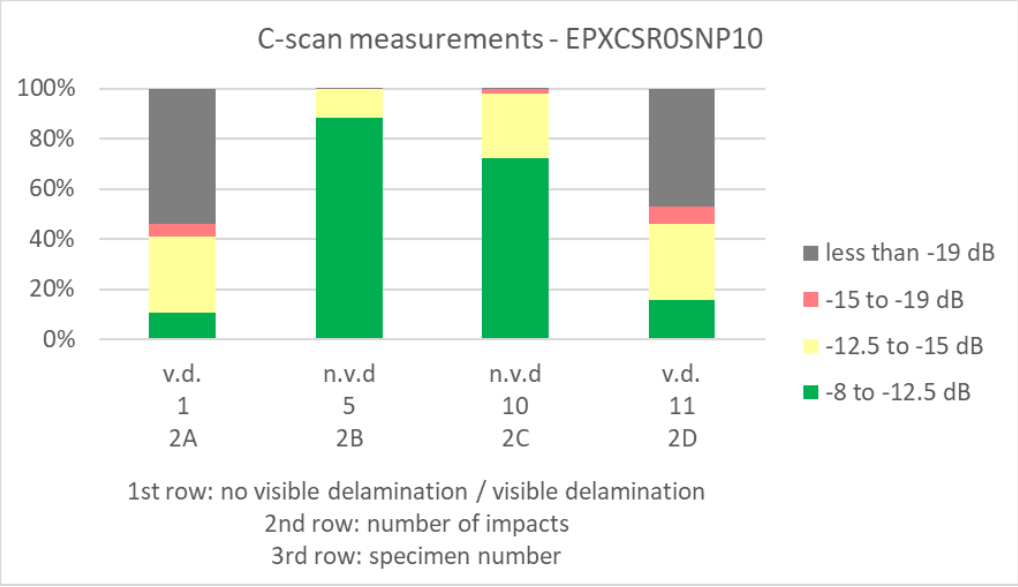

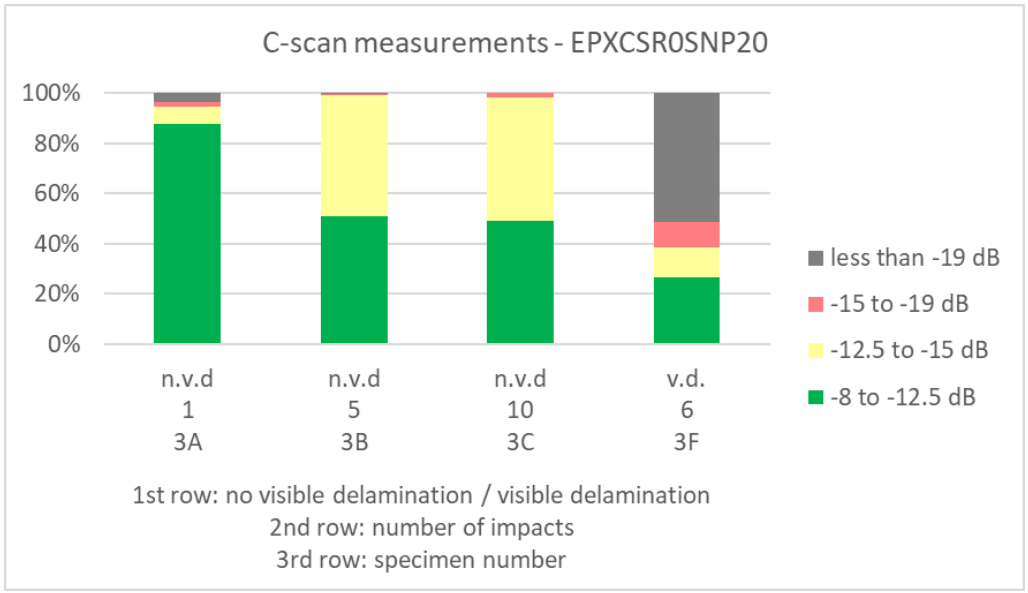
C-scan measurements - EPXCSR0SNP20
100%
80%
60%
40%
20%
0%
n.v.d
1
3A
n.v.d
5
3B
n.v.d
10
3C
v.d.
6
3F
less than -19 dB
-15 to -19 dB
-12.5 to -15 dB
-8 to -12.5 dB
1st row: no visible delamination / visible delamination
2nd row: number of impacts
3rd row: specimen number

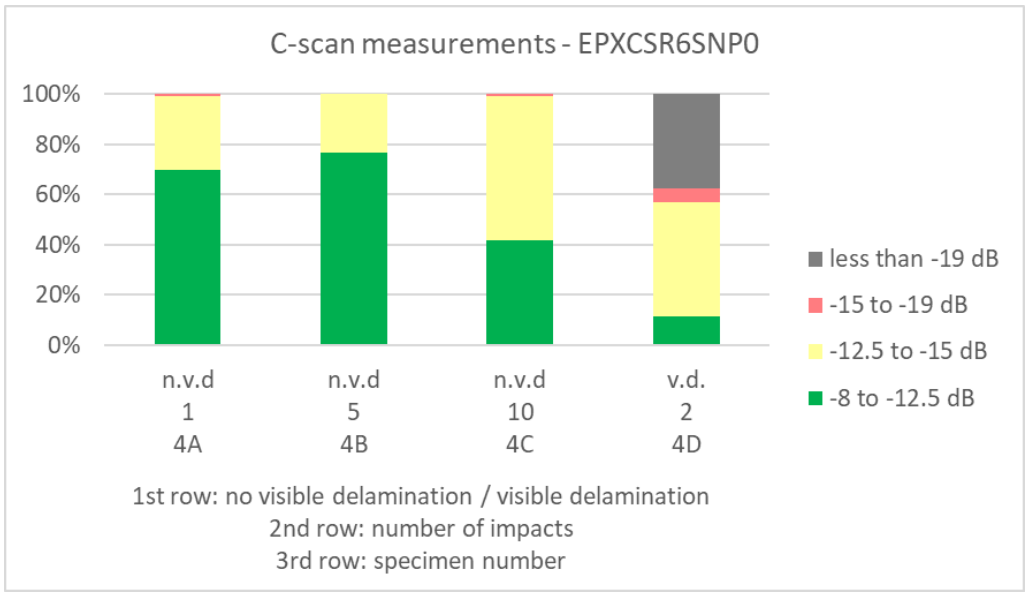
C-scan measurements - EPXCSR6SNP0
100%
80%
60%
40%
20%
0%
n.v.d
1
4A
n.v.d
5
4B
n.v.d
10
4C
v.d.
2
4D
less than -19 dB
-15 to -19 dB
-12.5 to -15 dB
-8 to -12.5 dB
1st row: no visible delamination / visible delamination
2nd row: number of impacts
3rd row: specimen number

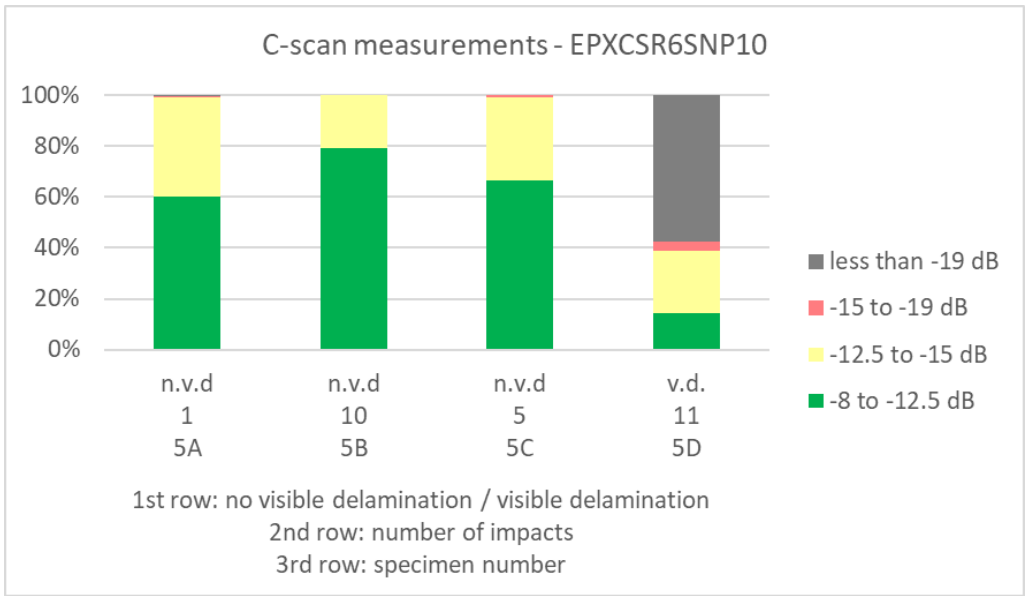
C-scan measurements - EPXCSR6SNP10
100%
80%
60%
40%
20%
0%
n.v.d
1
5A
n.v.d
10
5B
n.v.d
5
5C
v.d.
11
5D
less than -19 dB
-15 to -19 dB
-12.5 to -15 dB
-8 to -12.5 dB
1st row: no visible delamination / visible delamination
2nd row: number of impacts
3rd row: specimen number

X

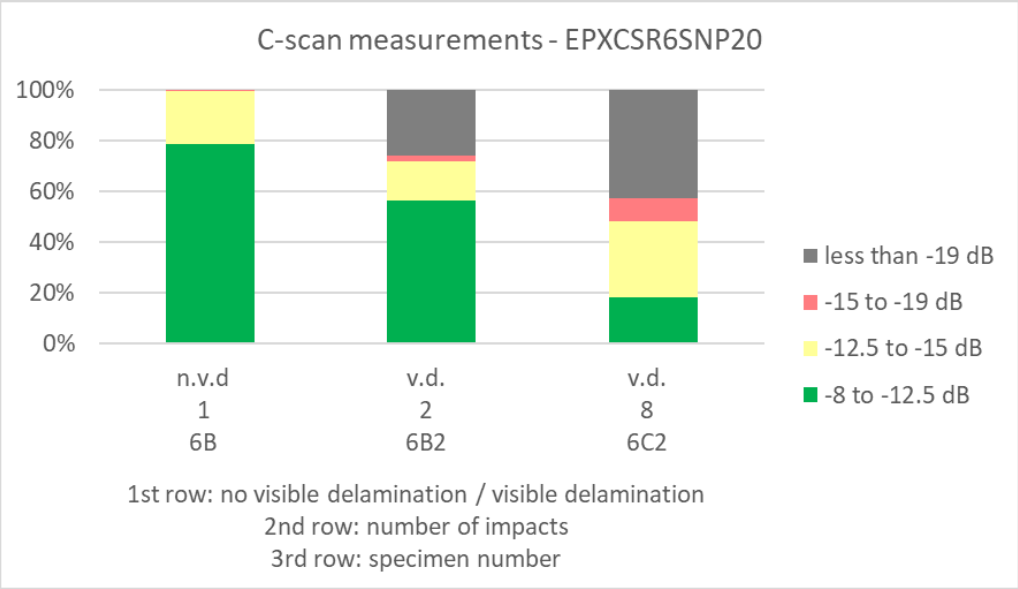
C-scan measurements - EPXCSR6SNP20
100%
80%
60%
40%
20%
0%
n.v.d
1
6B
v.d.
2
6B2
v.d.
8
6C2
less than -19 dB
-15 to -19 dB
-12.5 to -15 dB
-8 to -12.5 dB
1st row: no visible delamination / visible delamination
2nd row: number of impacts
3rd row: specimen number

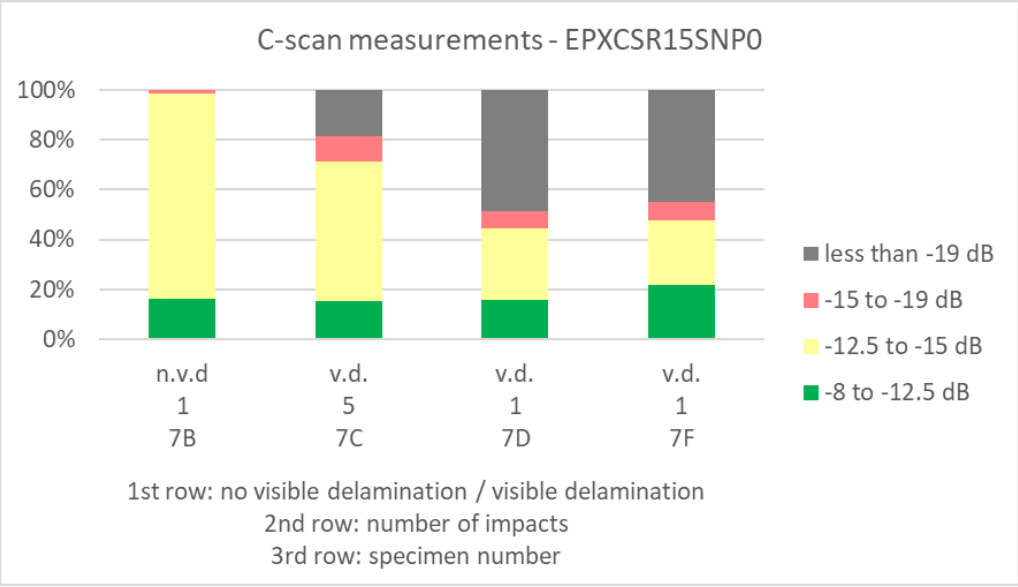
C-scan measurements - EPXCSR15SNP0
100%
80%
60%
40%
20%
0%
n.v.d
1
7B
v.d.
5
7C
v.d.
1
7D
v.d.
1
7F
less than -19 dB
-15 to -19 dB
-12.5 to -15 dB
-8 to -12.5 dB
1st row: no visible delamination / visible delamination
2nd row: number of impacts
3rd row: specimen number

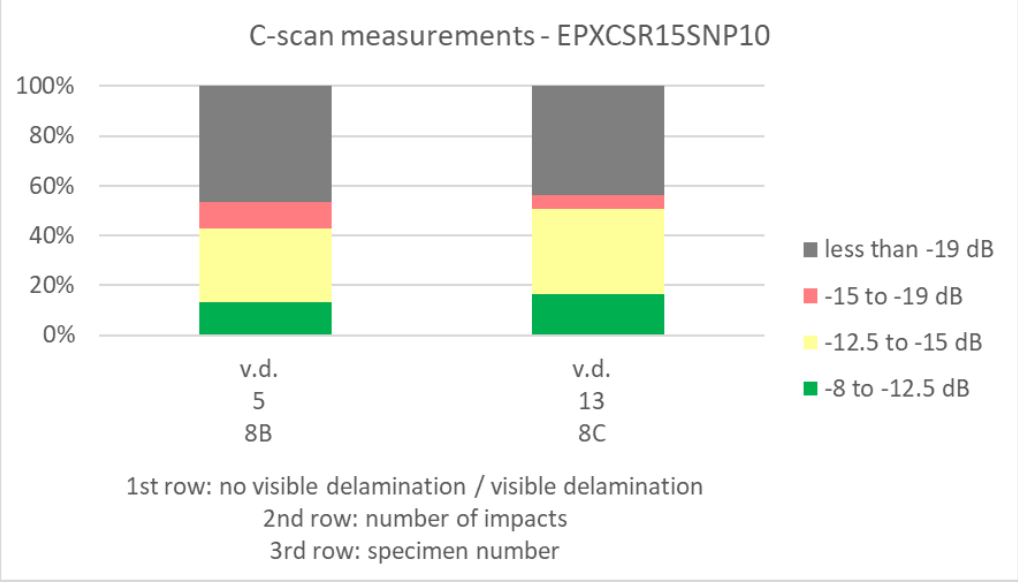
C-scan measurements - EPXCSR15SNP10
100%
80%
60%
40%
20%
0%
v.d.
5
8B
v.d.
13
8C
less than -19 dB
-15 to -19 dB
-12.5 to -15 dB
-8 to -12.5 dB
1st row: no visible delamination / visible delamination
2nd row: number of impacts
3rd row: specimen number

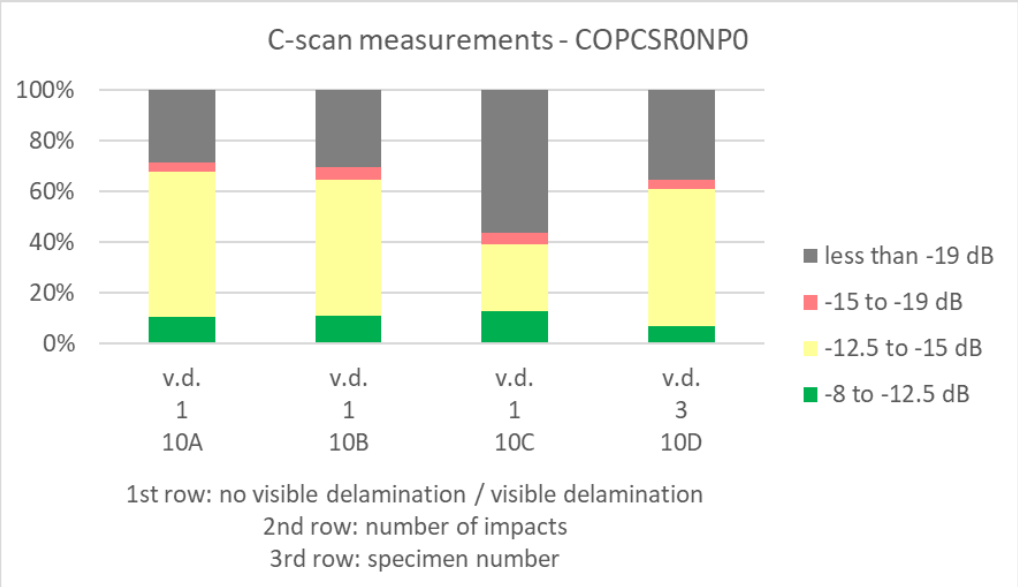
C-scan measurements - COPCSR0NP0
100%
80%
60%
40%
20%
0%
v.d. 1 10A
v.d. 1 10B
v.d. 1 10C
v.d. 3 10D
less than -19 dB
-15 to -19 dB
-12.5 to -15 dB
-8 to -12.5 dB
1st row: no visible delamination / visible delamination
2nd row: number of impacts
3rd row: specimen number

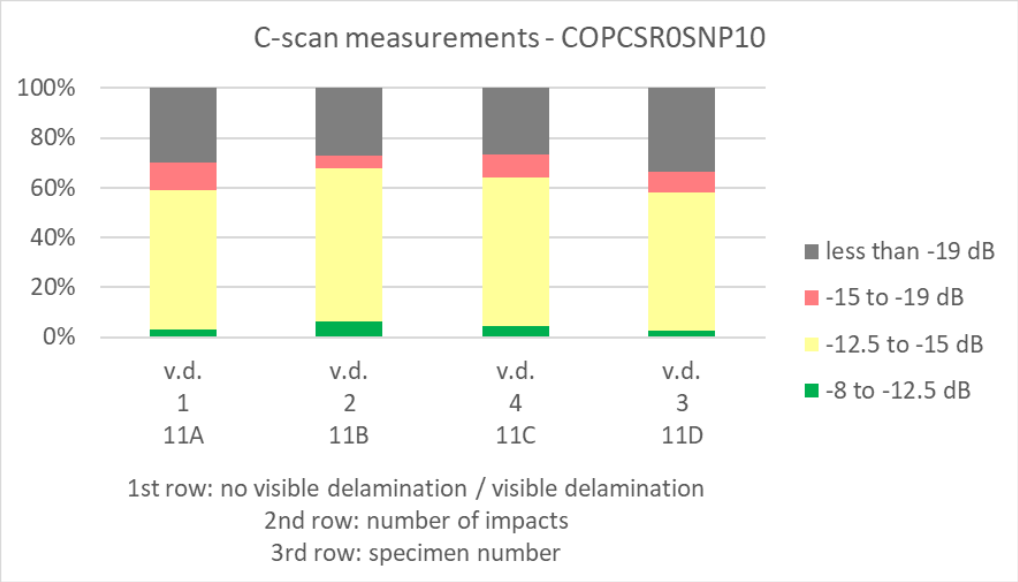
C-scan measurements - COPCSR0SNP10
100%
80%
60%
40%
20%
0%
v.d. 1 11A
v.d. 2 11B
v.d. 4 11C
v.d. 3 11D
less than -19 dB
-15 to -19 dB
-12.5 to -15 dB
-8 to -12.5 dB
1st row: no visible delamination / visible delamination
2nd row: number of impacts
3rd row: specimen number

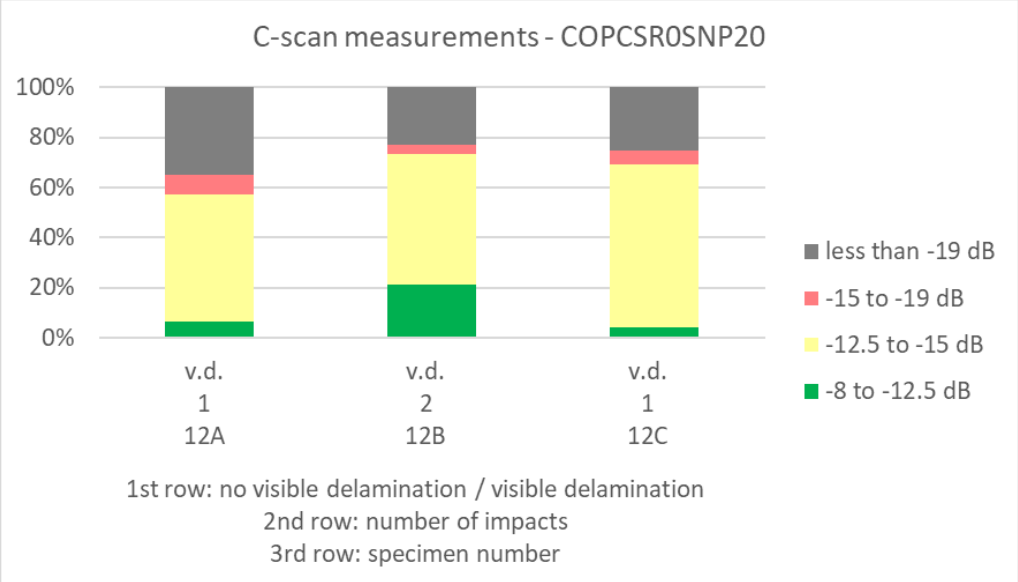
C-scan measurements - COPCSR0SNP20
100%
80%
60%
40%
20%
0%
v.d. 1 12A
v.d. 2 12B
v.d. 1 12C
less than -19 dB
-15 to -19 dB
-12.5 to -15 dB
-8 to -12.5 dB
1st row: no visible delamination / visible delamination
2nd row: number of impacts
3rd row: specimen number

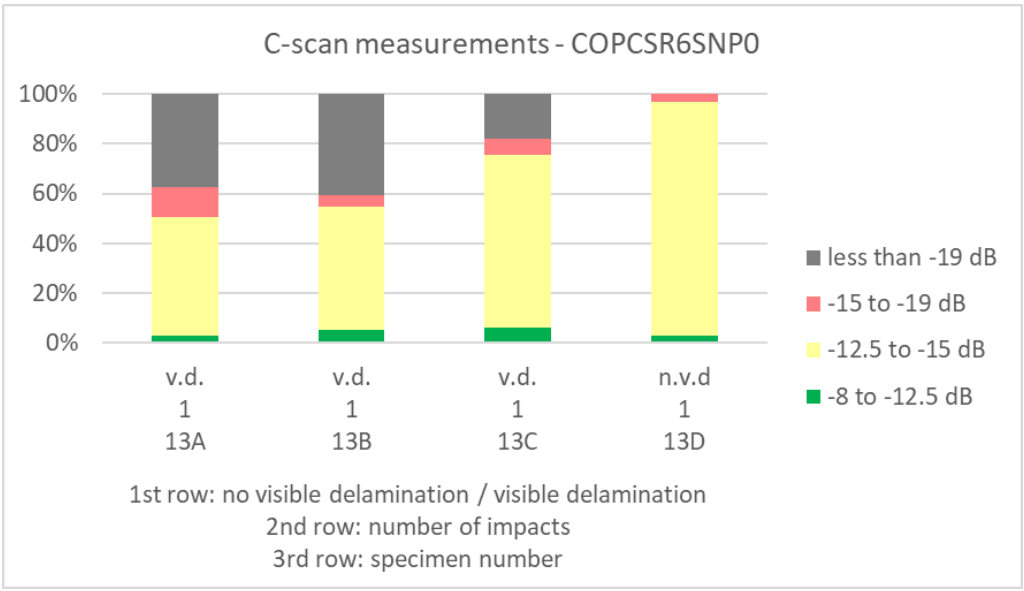
C-scan measurements - COPCSR6SNP0
100%
80%
60%
40%
20%
0%
v.d.
1
13A
v.d.
1
13B
v.d.
1
13C
n.v.d
1
13D
less than -19 dB
-15 to -19 dB
-12.5 to -15 dB
-8 to -12.5 dB
1st row: no visible delamination / visible delamination
2nd row: number of impacts
3rd row: specimen number

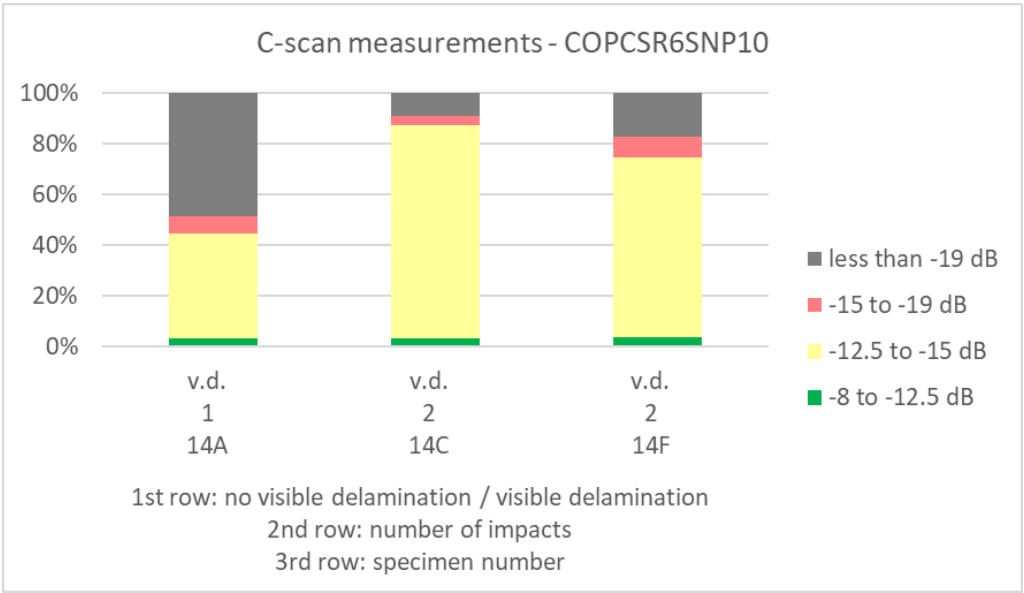
C-scan measurements - COPCSR6SNP10
100%
80%
60%
40%
20%
0%
v.d.
1
14A
v.d.
2
14C
v.d.
2
14F
less than -19 dB
-15 to -19 dB
-12.5 to -15 dB
-8 to -12.5 dB
1st row: no visible delamination / visible delamination
2nd row: number of impacts
3rd row: specimen number

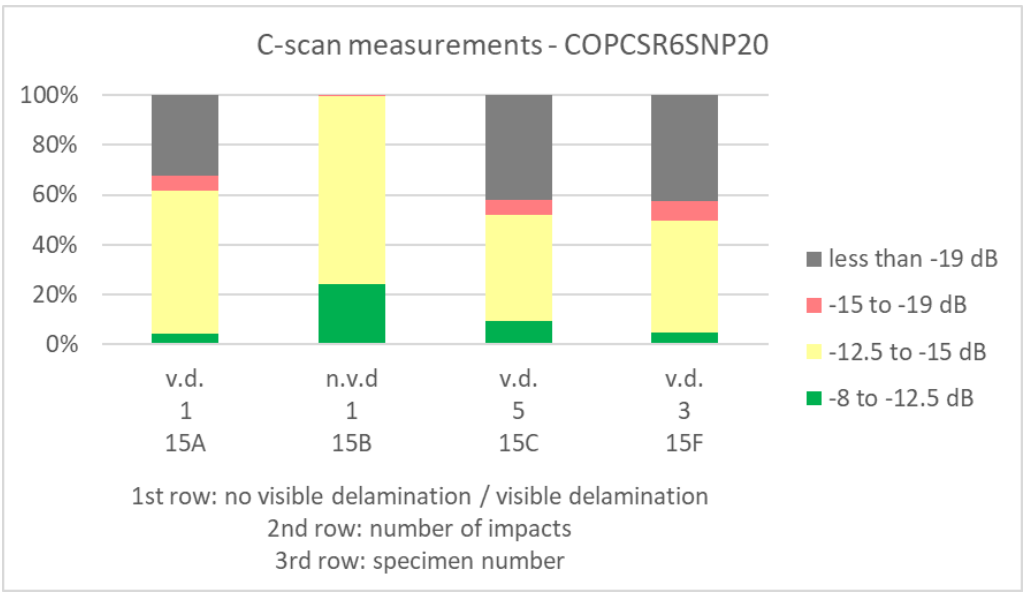
C-scan measurements - COPCSR6SNP20
100%
80%
60%
40%
20%
0%
v.d.
1
15A
n.v.d
1
15B
v.d.
5
15C
v.d.
3
15F
less than -19 dB
-15 to -19 dB
-12.5 to -15 dB
-8 to -12.5 dB
1st row: no visible delamination / visible delamination
2nd row: number of impacts
3rd row: specimen number

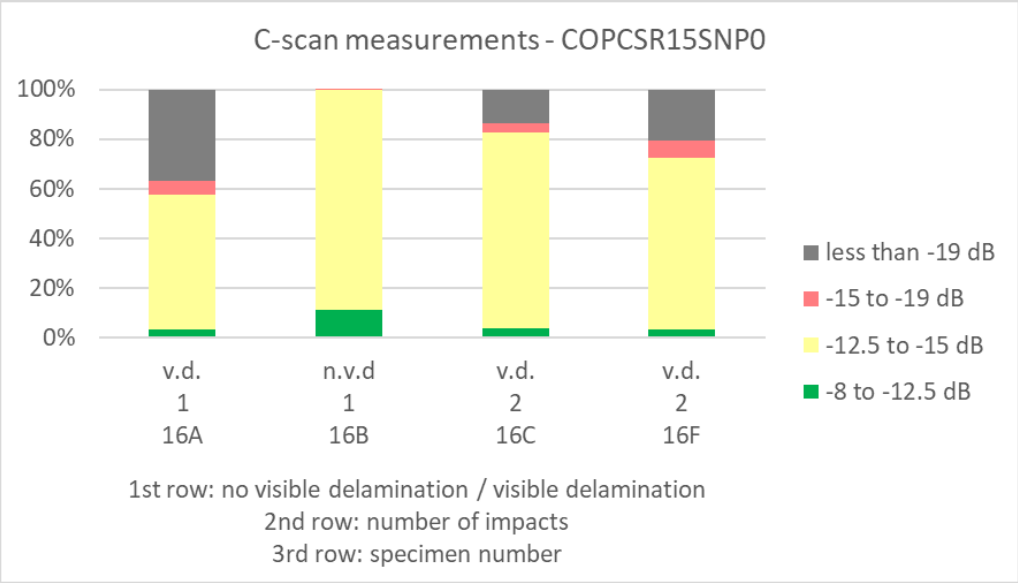
C-scan measurements - COPCSR15SNP0
100%
80%
60%
40%
20%
0%
v.d.
1
16A
n.v.d
1
16B
v.d.
2
16C
v.d.
2
16F
less than -19 dB
-15 to -19 dB
-12.5 to -15 dB
-8 to -12.5 dB
1st row: no visible delamination / visible delamination
2nd row: number of impacts
3rd row: specimen number

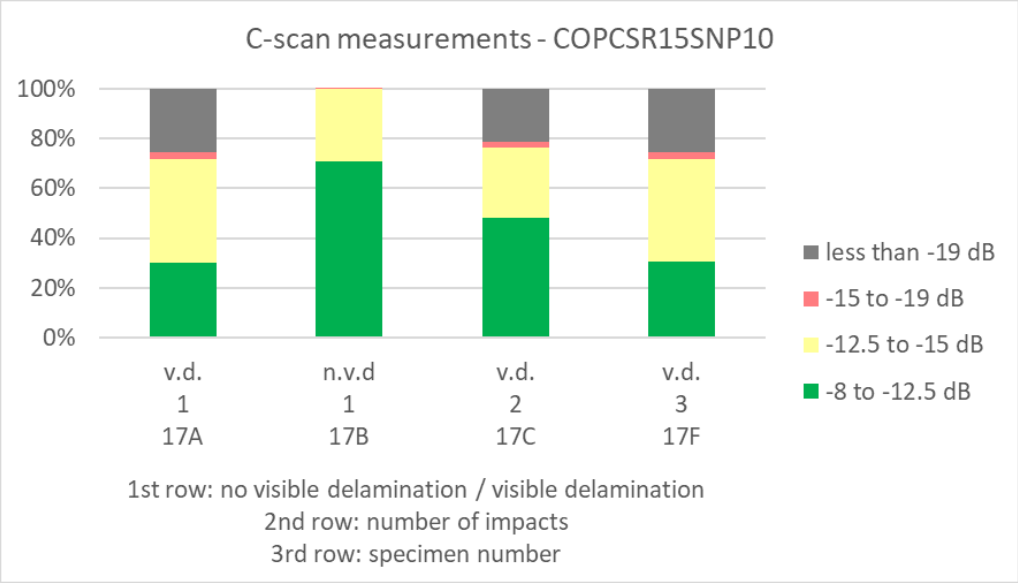
C-scan measurements - COPCSR15SNP10
100%
80%
60%
40%
20%
0%
v.d.
1
17A
n.v.d
1
17B
v.d.
2
17C
v.d.
3
17F
less than -19 dB
-15 to -19 dB
-12.5 to -15 dB
-8 to -12.5 dB
1st row: no visible delamination / visible delamination
2nd row: number of impacts
3rd row: specimen number